Doctoral Dissertation
Doctoral Program in Metrology (32nd cycle)

High-Accuracy Optical Frequency Metrology: traceability at the 10^{-17} level

Piero Barbieri

* * * * * *

Supervisor
Dr. Davide Calonico, INRiM

Doctoral Examination Committee:
Dr. Pablo Cancio Pastor, Referee, CNR - INO
Dr. Stéphane Schilt, Referee, Université de Neuchâtel

Politecnico di Torino
March 30, 2020

I hereby declare that, the contents and organisation of this dissertation constitute my own original work and does not compromise in any way the rights of third parties, including those relating to the security of personal data.

. . . .
Piero Barbieri
Turin, March 30, 2020

Summary

The advancements achieved in measuring and disseminating optical frequency signals have benefited the realisation of metrological standards. In particular, atomic clocks based on optical transitions show performances that outperform those of the current primary standards that realise the definition of the second in the International Systems of Units (SI), based on the hyperfine microwave transition of the fundamental level of the Cs atom. A future redefinition of the second will be possible if accurate frequency measurements of optical clocks with respect to the current Cs primary standard are performed, as well as direct comparisons of optical clocks to characterise their ultimate uncertainty level.

High-accuracy optical frequency measurements have been made possible thanks to the development of optical frequency combs, which are based on femtosecond pulsed lasers whose frequency spectrum consists of a series of equispaced optical frequency modes. Being the separation between the comb modes a radio-frequency, frequency combs provide a direct link between the optical and microwave domain, allowing comparison of optical frequencies with respect to the Cs primary standard. Moreover, optical combs make feasible measurements of optical frequency ratios, so that comparisons between different species of optical clocks can be performed. In this case optical combs are used as transfer oscillators throughout the optical domain. In addition, the same technique can be used to perform spectral purity transfer of ultrastable optical sources.

When atomic clocks have to be compared between distant facilities, proper methods to disseminate time and frequency signals have to be found. In the case of optical frequencies, the technique that makes possible accurate dissemination is based on the frequency transfer over networks of phase-stabilised optical fibre links. Dissemination at the accuracy level achieved by optical clocks have been demonstrated over distances of thousands of km.

This thesis reports on the work carried out at the Istituto Nazionale di Ricerca Metrologica (INRiM), the Italian National Metrology Institute (NMI), and the activity performed as guest researcher at the National Physical Laboratory (NPL), the UK's NMI.

The work performed at INRiM focused on using an erbium-fibre frequency comb

to enable spectral purity transfer of ultrastable lasers and optical frequency measurements of the ^{171}Yb optical lattice clock operating in our laboratories. Spectral purity transfer between the 1156 nm and 1542 nm spectral regions has been demonstrated with a residual instability of $5 \times 10^{-17}(\tau/\mathrm{s})^{-1/2}$ and accuracy of 3×10^{-19}. Two absolute frequency measurements of the ^{171}Yb clock have been performed by using the erbium-fibre comb, one with respect to the INRiM Cs primary standard, achieving uncertainty of 5.9×10^{-16}, the other with respect to the International Atomic Time timescale (TAI), with uncertainty of 2.6×10^{-16}. Furthermore, the optical comb was used to measure the optical frequency ratio between the ^{171}Yb clock and a transportable ^{87}Sr optical clock developed at the German NMI (PTB), with uncertainty of 2.8×10^{-16}.

At NPL preliminary investigations on a novel technique that could be used for the phase-stabilisation of fibre links have been carried out, studying backreflection signals generated in optical fibres. The effect of spurious signals and chromatic dispersion in fibre spools has been characterised and a coherent detection scheme that could make possible to retrieve information about phase fluctuations experienced over optical fibres has been developed.

Acknowledgements

I would like to thank my supervisor Davide Calonico for giving me the possibility to work on very interesting and innovating research subjects within an international collaboration frame, and also for continuously motivating and encouraging me during my PhD.

Many thanks to Cecilia Clivati, whose help, support, and guidance have been essential to my work.

I want to thank the INRiM folks of the Time and Frequency group, especially Salvatore Micalizio, Claudio Calosso, Marco Pizzocaro, Marco Tarallo, Elio Bertacco, Pierre Thoumany, Carolina Cardenas, Alberto Mura, Filippo Levi, Giovanni Costanzo, Benjamin Rauf, Matteo Frittelli, Giacomo Cappellini. A special thank to my INRiM colleagues and friends Filippo Bregolin, Michele Gozzelino, Anna Tampellini, Martina Gertosio, Gianmaria Milani, Matteo Barbiero, Haixiao Lin.

A sincere thank to Giuseppe Marra for advising, guiding and inspiring me during my period as guest researcher at NPL. Thank to the NPL's Time and Frequency group, especially to Jochen Kronjaeger, Riley Ilieva, Marco Schioppo, Rich Hendricks. Thank also to Radan Slavik for hosting me at the Optoelectronics Research Centre of the University of Southampton and Meng Ding for his kind help.

Funding This work has been funded by the "European Metrology Program for Innovation and Research" (EMPIR) projects 15SIB03 OC18 and 15SIB05 OFTEN. This project has received funding from the EMPIR programme co-financed by the participating states and from the European Union's Horizon 2020 research and innovation programme.

EMPIR EURAMET

The EMPIR initiative is co-funded by the European Union's Horizon 2020 research and innovation programme and the EMPIR Participating States

This work has been supported by the Q-SENSE project of the European Union. Q-SENSE project has received funding from the European Union's Horizon 2020 Research and Innovation Staff Exchange (RISE) Horizon 2020 program under Grant Agreement Number 691156.

"Dost thou love picking meat? Or wouldst thou see
A man in the clouds, and have him speak to thee?"

John Bunyan

"The world is always full of the sound of waves. The little fishes, abandoning themselves to the waves, dance and sing, and play, but who knows the heart of the sea, a hundred feet down? Who knows its depth?"

Eiji Yoshikawa

Contents

List of Tables

List of Figures

Chapter 1

Introduction

During the last century the advancements achieved in precise spectroscopy of atoms and molecules and optical frequency measurements have benefited, besides fundamental physics, the realisation of the metrological standards of length, time and frequency. In 1983 the speed of light in vacuum has been fixed to the precise value $c_0 = 299\,792\,458\ \mathrm{m\,s^{-1}}$ [1]. Since then, the metre is defined through the relation $c_0 = \lambda \cdot \nu$, being λ and ν the wavelength and frequency in vacuum of an electromagnetic plane wave. Therefore, each transition whose frequency can be traceable to the unit of time of the International System of Units (SI) gives access to either the standard of length, time or frequency. With the redefinition of the unit of length, practical guidelines to its realisation were recommended. Among the methods listed for the so-called *mise en pratique* of the new metre were either the measurement of the wavelength of an electromagnetic wave in vacuum referred to its correspondent SI frequency or the use of one of the wavelength reported in the list of the recommended radiations, including optical frequency-based standards [1]. Soon, the uncertainty achieved by using the first method encompassed by orders of magnitude the accuracy required for practical use in length metrology. Thanks to the improvements in precise measurements of laser radiations, frequency standards based on optical radiations had started to be traced to the primary standard of time, which among the SI base units is the one measured with the highest level of accuracy.

In the past, humanity has kept track of the flowing of time in a number of ways, based on periodical physical phenomena such as the apparent motion of the Sun in the sky or the oscillations of a pendulum. As the precision with which time is measured increased, the need of oscillators that do not show irregularities emerged. For this reason, the definition of the second that has been held until the 1960s based on the period of rotation of the Earth was no more adequate, as it shows variations over the years. Therefore, a redefinition based on an atomic standard took place at the General Conference on Weights and Measures (CGPM) in 1967. By exploiting the reproducibility and eternal immutability of atomic properties, the SI second was

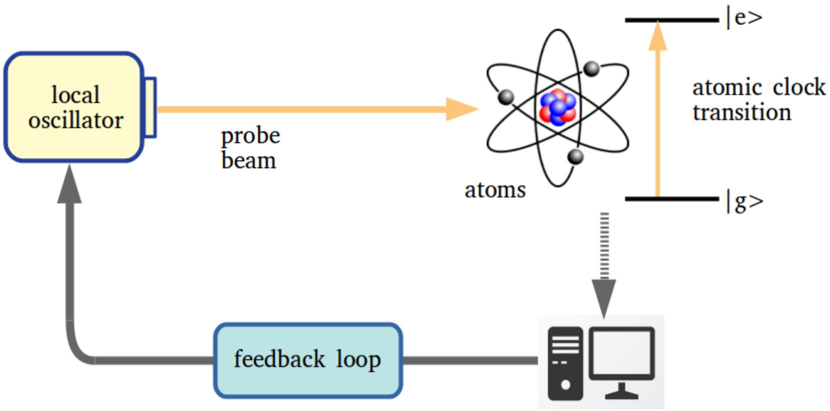

Figure 1.1: Atomic clock operation scheme.

defined as *"the duration of 9 192 631 770 periods of the radiation corresponding to the transition between the two hyperfine levels of the ground state of the caesium-133 atom"*. After the first demonstration of a caesium thermal beam-based clock in 1955 [2], atomic clocks that realise the definition of the SI second have made use of laser-cooling of atoms and new interrogation techniques to improve their performances. The current primary frequency standard is based on the Cs atomic fountain scheme [3] and achieves an ultimate uncertainty in the low 10^{-16}. Very recently, a new revision of the SI has been approved by the CGPM [4], leading to a redefinition of the base units in May 2019 based on seven physical constants. For what concerns the SI second, this translated in just a rewording of the previous definition with particular emphasis on the role of the transition of the ^{133}Cs ground state as a physical constant: the SI second is defined *"by taking the fixed numerical value of the caesium frequency $\Delta\nu_{Cs}$, the unperturbed ground-state hyperfine transition frequency of the caesium 133 atom, to be 9 192 631 770 when expressed in the unit Hz, which is equal to* s^{-1}*"*.

Atomic clocks basically rely on a narrow atomic transition as a reference to trace the frequency of a local oscillator. A sketch of an atomic clock operation is shown in fig. 1.1. During the clock operation atomic samples are probed by means of a local oscillator frequency-tuned close to the atomic resonance of interest. Depending on the spectroscopy signal obtained from the probing process, a correction is applied to the local oscillator in order to keep its frequency at the corresponding atomic transition value.

The current definition of the second is based on an atomic transition in the microwave domain. However, nowadays the best performing atomic clocks are based on optical transitions, which surpass the Cs fountain standard in terms of both accuracy and stability. Optical atomic clocks exploit atomic transition frequencies

10^5 times higher than the microwave clocks, allowing improved levels of stability of the clocks thanks to the higher quality factor $Q \propto 1/\Delta\nu$ [5]. Therefore, much interest in developing and characterising such frequency standards has arisen, and to date optical clock based on single ions [6] or neutral atoms trapped in an optical lattice [7] show uncertainty up to the 10^{-18} level [8–10]. With uncertainties that largely surpass the current primary standard performances, optical clocks became the favourite candidates for a future redefinition of the SI second. Meanwhile, eight optical frequency standards have already been selected as secondary representations of the second [11].

In order to prove the reliability of optical frequency standards is necessary to measure them against the current primary standard and at the same time to perform a direct comparison between optical clocks at their intrinsic level of accuracy, i.e. without being limited by the Cs atomic fountain. In addition, proper techniques to remotely disseminate optical frequency standards without deteriorating the clock performances had to be found. These needs have been met by the advent of the optical frequency comb [12] and the development of frequency transfer techniques, in particular based on optical fibre link networks [13].

Optical frequency measurements

Before the 2000s, high-accuracy measurements of frequency were limited to the radio-frequency (RF) domain and microwave domain up to $\sim$ 100 GHz, where the measurement is made directly thanks to the availability of counters and synthesisers or by using heterodyne techniques. When the frequency increases up to the hundreds of THz region in the optical domain, electronic counters cannot be used. On the other hand, for instance interferometric techniques can provide measurement of lasers' wavelength with precision of about tens or hundreds of MHz, which is far from being satisfactory.

Finding a "clockwork"to connect the optical and microwave domains and to allow traceable measurements of optical frequencies against the primary standard in the microwave domain had represented a challenging issue.

The common approach consisted in building harmonic frequency chains, where the gap between the microwave and optical domains was covered through a stepwise series of frequency multiplications, starting from a known lower frequency up to the target optical one. The frequency bridge realised with these measurement chains required a large-scale apparatus and the knowledge and control of a huge assortment of devices dedicated to the microwave, far and near infrared, and visible domains. Moreover, each frequency chain was built specifically to measure a single optical frequency, limited by the tunable range of the involved oscillators. For this reason, a few optical frequency standards have been measured through harmonic frequency chains, for instance the 3.39 µm CH_4 [14, 15] and the 657 nm Ca [16, 17] standards.

In an alternative way, some efforts have been dedicated to measurement schemes based on the division of a large frequency gap into smaller intervals. By iterating the division process, such frequency difference signals became small enough to be measured with a frequency counter, allowing to recover the original frequency gap. The most common method is the frequency interval bisection [18]. It can be explained by considering for instance three laser sources of frequency ν_1, ν_2 and ν_3 that fulfil the relation $2\nu_3 = \nu_1 + \nu_2$. Such signals can be produced by exploiting second-harmonic and sum-frequency generation in nonlinear crystals. In this way, a signal at frequency ν_3 is phase-locked to the midpoint between ν_1 and ν_2 by stabilising the RF beatnote signal $2\nu_3 - (\nu_1 + \nu_2)$. Another technique employed to generate frequency differences was based on using an electro-optic modulator (EOM) inside a Fabry-Pérot cavity to produce modulation sidebands around the carrier frequency of a laser. By choosing a cavity resonant to both the carrier and the sidebands frequencies, frequency intervals up to 30 THz have been covered [19].

The limitations and complex realisation of the methods above described were overcome by the development of optical frequency combs and their first demonstration for measuring optical frequencies [20, 21]. The invention of the optical frequency comb was awarded in 2005 with the Nobel Prize in Physics to John L. Hall and Theodor W. Hänsch for "*their contributions to the development of laser-based precision spectroscopy, including the optical frequency comb technique*"[22, 23]. Optical frequency combs are based on mode-locked lasers, which emit a periodic train of pulses of duration as small as few fs in the time domain. The frequency domain counterpart of a mode-locked laser output is a sequence of sharp frequency modes equally spaced, a "frequency comb". Each frequency mode ν_m is described by the equation

$$\nu_\mathrm{m} = f_0 + m f_\mathrm{rep}, \tag{1.1}$$

where f_rep quantifies the spacing between two optical modes, called the comb repetition rate, f_0 is an offset, and m is the integer number that identifies a single comb mode. Therefore, the comb structure provides a "frequency ruler"that can be used to count an optical frequency in terms of the RF-signals f_rep and f_0. As can be seen from fig. 1.2, once f_rep, f_0 and m are known, by measuring the beatnote between an optical source and the nearest comb mode a direct link between the optical and microwave domain is established. Optical frequency measurements can then be realised through a single device suitable for table-top applications. Absolute frequency measurements by using an optical frequency combs have been validated at the 1×10^{-19} level [24].

Although mode-locked lasers have been firstly demonstrated in 1964 [25], it took more than thirty years before such kind of lasers can be classified as optical frequency combs suitable for optical frequency metrology. Absolute optical frequency measurements are possible only if f_rep and f_0 can be measured. While f_rep is easily detectable, the same could not be said for the offset frequency f_0. As will be

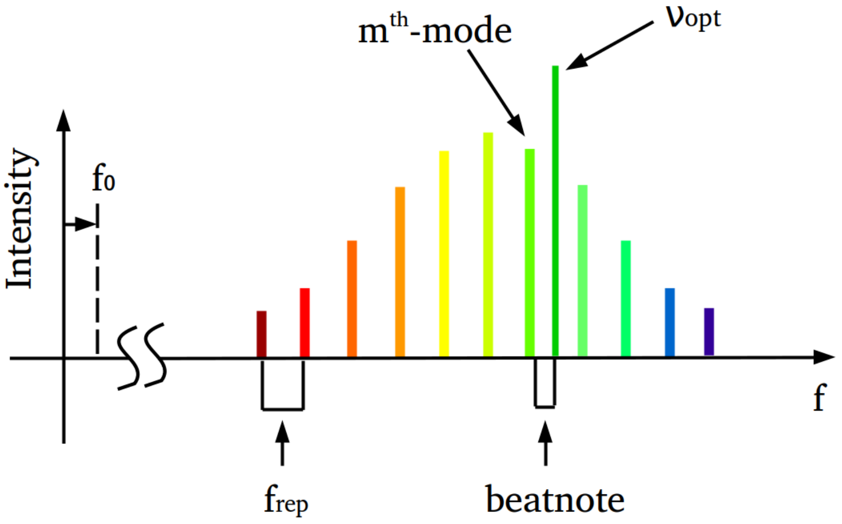

Figure 1.2: Measuring an unknown optical frequency ν_{opt} by using an optical frequency comb.

detailed in chapter 2, the f_0 detection requires that the comb output covers a frequency octave, which has been made possible only in the late 1990s by exploiting spectral broadening in microstructured optical fibres [26, 27].

The other key aspect that makes optical combs essential tools for time and frequency metrology is the capability of directly comparing optical sources, particularly optical clocks. As will be explained in chapter 3 and chapter 4, optical combs can be used as transfer oscillators for measuring optical frequency ratios. Such measurements are performed through the transfer oscillator technique [28] (see chapter 3), where the comb contribution is cancelled out from the optical frequency comparison. Optical frequency ratio measurements with an ultimate uncertainty in the 10^{-21} regime by using optical combs have been demonstrated [29]. Moreover, by means of the same transfer scheme optical combs allow to copy the properties of high-stability optical sources throughout the optical domain, as described in chapter 3, allowing the development of several ultrastable sources referenced to a common master oscillator.

Optical frequency dissemination

The other requirement of a time and frequency metrological measurement chain is finding a proper transfer channel to compare frequency standards located in different National Metrology Institutes (NMIs).

The most established method used for time and frequency dissemination is based on satellite microwave transfer [30]. However, as the accuracy of optical clocks improves up to the 10^{-18} level, satellite-based techniques are no more satisfactory for the accurate dissemination of optical frequency standards. The satellite instability would limit the optical clock transfer, since it is a factor 10^4 lower than the optical clocks' accuracy. To cope with this problem, novel methods have been proposed, which rely on using optical fibre links for the dissemination of both optical, microwave and timing signals [31, 32]. As will be described in chapter 5, these techniques make use of already existing telecom fibre infrastructures. By implementing a phase-stabilisation of the optical fibres, optical clock comparisons over thousands of km have been demonstrated with an uncertainty contribution due to the optical frequency transfer lower than 10^{-18} after 10 000 s of averaging time [33].

Thesis overview

This thesis reports on the work I performed during my Ph.D. activity at the Istituto Nazionale di Ricerca Metrologica (INRiM), the Italian NMI, between 2016 and 2019. I worked in the Quantum Metrology and Nanotechnology division's laboratories, which are part of the INRiM campus in Turin. The work focused on using an erbium-fibre optical frequency comb to realise spectral purity transfer of ultrastable laser sources and to perform measurements of the INRiM ^{171}Yb optical lattice clock [34, 35].

This dissertation includes also the activity carried out at the National Physical Laboratory (NPL), the NMI of UK, where I worked as a visiting Ph.D. student between 2018 and 2019. There, I studied technical limitations and possible improvements of time and frequency transfer techniques using optical fibres.

The thesis is organised as follows:

- Chapter 2 provides the theoretical background of optical frequency combs, including the mode-locked laser operation and the detection of the comb parameter f_0 and f_{rep}. Then erbium-fibre optical combs are presented in more details, referring in particular to the comb system used at INRiM.

- Chapter 3 describes the use an characterisation of the optical comb to transfer the spectral purity of a 1156 nm ultrastable laser to a 1542 nm telecom laser. We characterised the different noise contributions to the spectral transfer, giving an upper limit evaluation of the comb performances that can be generalised to similar systems. The last section of the chapter is dedicated to the optical-to-microwave transfer by using the optical comb as a frequency divider.

- Chapter 4 reports on the optical frequency measurements of the ^{171}Yb optical clock using the optical comb. Two absolute frequency measurements of the

Yb standard are presented, one with respect to the Cs primary standard operating at INRiM, the second by exploiting a link to the International Atomic Time (TAI). An optical frequency ratio measurement between the Yb clock and a transportable Sr optical clock developed at the Physikalisch-Technische Bundesanstalt (PTB) is presented, which has been realised within the ‟International timescales with optical clocks″(ITOC) project.

- Chapter 5 illustrates the activity performed at NPL, concerning the characterisation of the effect of spurious signals and chromatic dispersion in optical fibres. The preliminary investigation on a novel technique that could be used for the phase-stabilisation of fibre links is presented, based on exploiting back-reflection signals along fibre spools.

Chapter 2

Optical frequency combs

In this thesis metrological-related applications of optical frequency combs will be explained through the experiments carried out at INRiM's laboratories. Absolute optical frequency measurements and optical clock comparison are among the fundamental measurements that are performed in a time and frequency laboratory. Moreover, optical combs allow the transfer of the properties of high-spectral purity sources throughout the optical domain, which is extremely useful for the improvement of optical atomic clocks.

However, thanks to their features such as broadband covering of the optical domain and narrow-linewidth high-coherent modes, optical combs have found application in several research fields and also outside the laboratories. Multiple examples can be found in spectroscopy experiments [36], where the comb allows absolute spectroscopy of atoms and molecules across a large portion of the optical domain, from the mid-IR to the visible [37, 38]. In addition, optical combs have been also used for direct spectroscopy, where the samples are probed by multiple wavelengths at the same time [39], and for dual-comb spectroscopy, by overlapping two optical combs with slightly different repetition rate [40]. Other applications include the calibration of high-resolution spectrographs for measuring the velocities of astronomical sources [41], as well as the generation of low-noise microwave signals using the comb as a frequency divider [42], which affects also many sectors of our society such as military and communication areas. Furthermore, frequency combs benefited measurements of distances by improving the resolution with respect to traditional laser-based interferometry [43].

This chapter describes the theory of mode-locked laser (MLL) sources and how optical frequency comb are generated from this kind of oscillators. A summary of different types of optical combs is provided, with particular attention dedicated to erbium-fibre-based systems. Finally, the multi-branch erbium-fibre comb used at INRiM is presented, discussing the optical setup and the comb stabilisation.

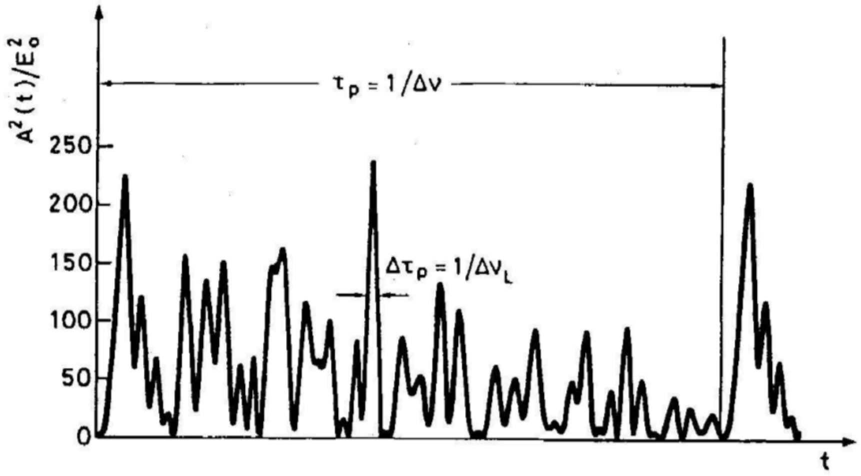

Figure 2.1: Time behaviour of $|A(t)|^2/E_0^2$ in the case of oscillating modes of same amplitude (taken from [44]).

2.1 Mode-locked lasers

Optical cavities can sustain a large number of longitudinal modes with frequencies ν_n equally spaced by a quantity $\Delta\nu_n$ known as free spectral range (FSR). The mode frequency value ν_n can be inferred imposing that the cavity resonator length L must contain an integer number n of half wavelength $\lambda/2$, i.e. $L = n\lambda/2$. Hence ν_n and $\Delta\nu_n$ are expressed by

$$\nu_n = \frac{n}{\sqrt{\epsilon_r \mu_r}} \frac{c}{2L} \quad , \quad \Delta\nu_n = \frac{c}{2L\sqrt{\epsilon_r \mu_r}}, \tag{2.1}$$

where ϵ_r and μ_r are respectively the relative electric permittivity and the relative magnetic permeability of the cavity medium, and c is the light speed. A laser impinging the cavity oscillates on a subset of such modes, the actual number depending on its gain bandwidth. This can be very large in the case of dye laser and solid-state laser (up to 400 nm of gain bandwidth in the Ti:sapphire-based lasers [44]). In the case of a single-frequency laser, oscillation happens on a single cavity mode. Usually, such laser modes have a random initial phase, and in continuous-wave (CW) operation the intensity of the laser output has a random profile due to interference between them. Figure 2.1 shows the time behaviour of the total output power, expressed in terms of the total power of the electric field $|A(t)|^2$ normalised by the power of the single mode E_0^2 (assumed to be the same for each mode). Nevertheless, since this amplitude shape arises from the sum of N equispaced frequency modes it shows typical features of a Fourier series, which are periodicity in the emission, of period $\tau_p = 1/\Delta\nu$, and pulsed behaviour, with pulse duration $\Delta\tau_p = 1/\Delta\nu_L$, where $\Delta\nu_L = N\Delta\nu$ is the total oscillation bandwidth. Therefore,

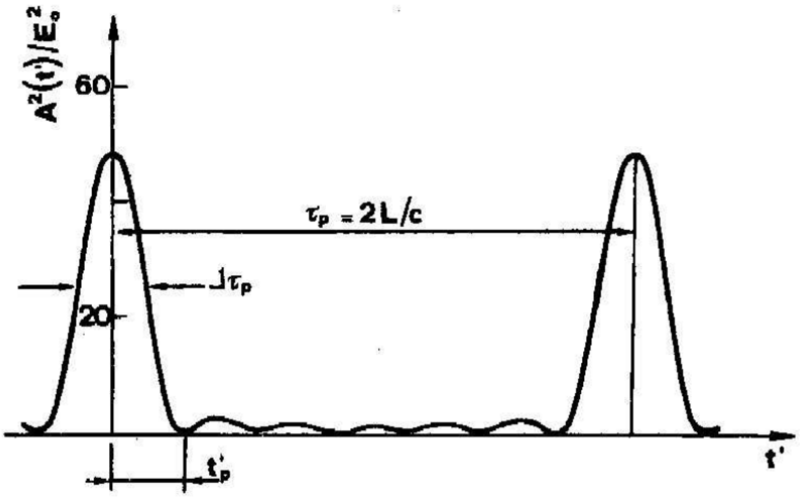

Figure 2.2: Time behaviour of $|A(t)|^2/E_0^2$ in the case of oscillating modes with locked phase and equal amplitudes (taken from [44]).

lasers with large gain bandwidth ($\sim \Delta\nu_L$) can yield pulses with duration less than ps. However, the average pulse power cannot reach high contrast with respect to the continuous operation because of the random interference of the pulses.

Lasers are called mode-locked when the oscillating modes can be forced to propagate with a well defined phase relation. To understand how mode-locking arises, we can consider the case of $(2N+1)$ oscillating modes with equal amplitudes, where N is an integer number. If their phases ϕ can be forced to follow the relation

$$\phi_l - \phi_{l-1} = \alpha \tag{2.2}$$

with α constant, then the total electric field of the output beam will be expressed as the sum over the $(2N+1)$ modes:

$$E(t) = \sum_{l=-N}^{N} E_0 e^{i[(2\pi\nu_0 + 2\pi l\Delta\nu)t + l\alpha]} = A(t)e^{i2\pi\nu_0 t}, \tag{2.3}$$

where ν_0 is the central mode frequency, and

$$A(t) = \sum_{l=-N}^{N} e^{il(2\pi\Delta\nu t + \alpha)}. \tag{2.4}$$

Thus, the total electric field is composed by a carrier wave of frequency ν_0 with an amplitude modulation $A(t)$. Replacing t with a new variable t', such that $2\pi\Delta\nu t' = 2\pi\Delta\nu t + \alpha$, $A(t)$ can be written as [44]:

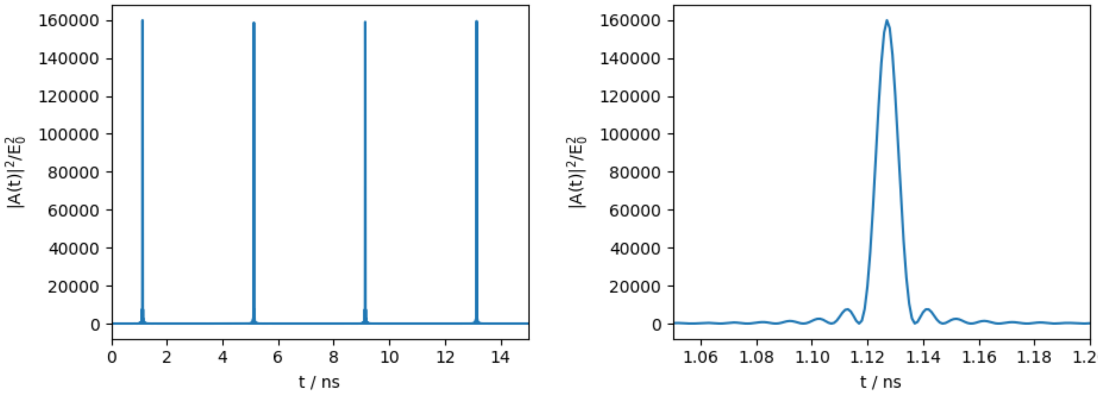

(a) **(b)**

Figure 2.3: Simulation of a mode-locked laser output with round-trip time $\tau_p = 4$ ns and $N = 400$ optical modes within the laser gain bandwidth $\Delta\nu_L = 100$ GHz. (a) First four pulses emitted by the mode-locked laser. (b) Zoom in on the first pulse emitted by the mode-locked laser.

$$A(t') = E_0 \frac{\sin[(2N+1)\pi\Delta\nu t']}{\sin(\pi\Delta\nu t')}. \tag{2.5}$$

Figure 2.2 shows the amplitude envelope as a function of t' in such configuration. It can be seen that the laser emission has a pulsed behaviour, and each pulse concentrates the total field power E_0^2. Pulses are periodical, with period τ_p expressed as the time difference between two peaks

$$\tau_p = \frac{1}{\Delta\nu}. \tag{2.6}$$

From fig. 2.2 it can be seen that the full width at half maximum (FWHM) $\Delta\tau_p$ of $A^2(t')$ is approximately equal to t'_p. Thus, using eq. (2.5) the pulse width can be written as

$$\Delta\tau_p \simeq \frac{1}{(2N+1)\Delta\nu} = \frac{1}{\Delta\nu_L}. \tag{2.7}$$

Hence the output beam of a mode-locked laser consists of a series of short pulses, with duration $\Delta\tau_p$ equal to the inverse of the total oscillation bandwidth of the laser $\Delta\nu_L$, and separated by the round-trip time of the light in the cavity $\tau_p = 2L/v_g$, where v_g is the group velocity of the pulse. Moreover, from eq. (2.5), taking $\sin\alpha \sim \alpha$ for $\alpha \ll 1$, it can be seen that the power of the pulse is proportional to $(2N+1)^2E_0^2$, instead of $(2N+1)E_0^2$ as when the modes have random phase distribution. In the case of a femtosecond mode-locked laser the number of modes can be as high as $2N+1 \approx 10^5 - 10^6$, leading to pulse power up to tens of MW and pulse width of few fs [44].

2.1.1 Mode-locking techniques

In time domain description, once the mode-locking condition is achieved, the pulse train can be viewed as a single ultra-short pulse propagating back and forth in the laser cavity, and partially transmitted outside of it. The exiting pulses are separated by the round-trip time τ_p. Therefore, the basic idea that lies behind the mode-locking techniques is to act as a shutter. That shutter has to be fast enough to be opened at time intervals equal to τ_p and it has to start operating possibly when the more intense pulse reaches it. Furthermore, the shutter opening time has to be comparable to the pulse duration in order to allow only the propagation of this pulse inside the cavity [44].

Mode-locking methods can be divided into two main categories, namely active mode-locking techniques, where the shutter is activated by external sources, and passive mode-locking techniques, which are achieved, for instance, through saturable absorption.

An example of active mode-locking is the amplitude modulation mode-locking, where the resonator losses are modulated in order to have a minimum in correspondence of the time at which the pulse propagation is desired, or the phase modulation mode-locking, which operates through periodic phase modulation [44]. However, active mode-locking typically is not used as is too slow to allow the generation of femtosecond pulses.

The mode-locked lasers used to develop frequency combs mainly exploit passive mode-locking techniques. Passive methods produce the shortest pulses [45], up to few fs, because of the faster modulation of the resonator losses that can be achieved. Among passive mode-locking techniques is saturable absorbtion using materials with a finite number of absorbers, e.g. dyes and semiconductors. If an absorber material is placed, e.g., in contact with one cavity mirror, the initial non-phase-locked pulses of fig. 2.1 with low intensity suffer the absorber loss more than the intense ones. Hence after several round-trips only the most intense pulse survives and achieves a net gain greater than the total loss [44].

In the case of the Ti:sapphire mode-locked laser, which achieves the shortest pulses thanks to its broad gain spectrum (pulse duration of ~ 5 fs [46]), the passive mechanism is realised with the Kerr lens mode-locking (KLM). The Kerr effect occurs when high intensity pulses travel in a suitable optical material and consists in a variation of the refractive index n of the medium proportional to the electric field intensity I [47]

$$n = n_0 + n_2 I, \tag{2.8}$$

where n_0 is the refractive index of the unperturbed medium and n_2 refers to the contribution of the Kerr effect. Considering a beam propagating inside the cavity with a Gaussian transverse intensity distribution, a spatial variation of the refractive index similar to that of a spherical lens is induced. Thus, low-intensity pulses which are loosely focused are blocked by a diaphragm or aperture placed inside the cavity, so that only the most intense pulse survives [44, 48].

Other passive mode-locking techniques use for example semiconductor saturable absorber mirror (SESAM), such as in the case of Yb:KYW fibre-laser comb [49] and Er:Yb:glass laser comb [50], while for Er fibre-laser comb mode-locking is achieved through a nonlinear polarisation rotation effect, as will be described in section 2.5.

2.2 Mode-locked lasers' spectrum

The pulses' phase evolves from pulse to pulse, as can be explained by taking into account the difference between the group velocity v_g and the phase velocity v_p. These two velocities differ due to the dispersion inside the cavity. $v_g = \partial\omega/\partial k$ is the velocity at which the light-pulse envelope travels, where ω is the angular frequency and k is the wawenumber, while the phase velocity is expressed as $v_p = \omega/k$ and it is the velocity of the laser carrier. This situation is depicted in fig. 2.4 a). The carrier-envelope phase $\Delta\phi_{ce}$ quantifies the phase shift between the pulse carrier of angular frequency $\omega_c = 2\pi\nu_0$ and the envelope peak. $\Delta\phi_{ce}$ is given by

$$\Delta\phi_{ce} = (\frac{1}{v_g} - \frac{1}{v_p})L\omega_c, \tag{2.9}$$

where ω_c is the carrier frequency of the envelope and L is the cavity length.

In the frequency domain, this results in a series of equally spaced frequency modes, whose spacing is the so-called repetition rate $f_{\text{rep}} = 1/\tau_p$, the inverse of the round-trip time (see fig. 2.4 b)). As a consequence, the comb feature of the frequency modes arises from the constructive interference of the pulses. That interference occurs at frequencies that are integer multiples of the repetition rate [51]. Therefore, in the frequency domain the laser modes' equation is expressed by:

$$\nu_m = m\frac{1}{\tau_p} + \frac{\Delta\phi_{ce}}{2\pi}\frac{1}{\tau_p} = mf_{\text{rep}} + f_0, \tag{2.10}$$

where m refers to the mode number and f_0 is the offset frequency, which is generated from the evolution of the carrier-envelope phase from pulse to pulse and it is related to $\Delta\phi_{ce}$.

Equation (2.10) illustrates once again the basic concept that has led to the employment of mode-locked lasers in optical frequency metrology. Indeed, if one can count the number of modes m and measure the two parameters f_{rep} and f_0, then an optical frequency measurement can be easily down-converted to a measurement in the microwave domain through the detection of a heterodyne beatnote between the optical source of interest and the nearest comb mode.

In the following section we describe how mode-locked lasers became optical frequency combs, which is not just a matter of semantic.

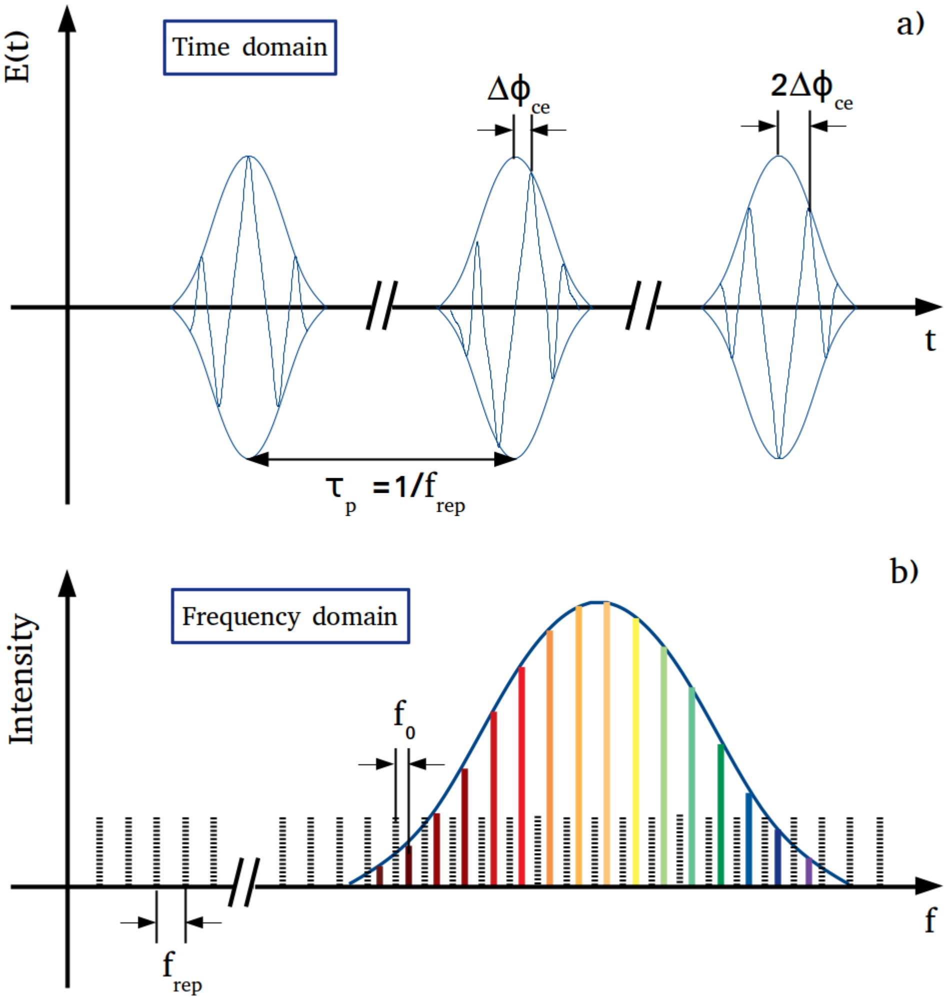

Figure 2.4: Mode-locked laser spectrum in the time domain, a), which is represented by a pulse train with evolving carrier-to-envelope phase, and in the frequency domain, b), which shows the equispaced comb modes' structure.

2.3 Detection of the parameters f_{rep} and f_0

Using mode-locked lasers for performing high-precision measurements of optical frequencies clearly requires that the frequency modes of eq. (2.10) do not experience frequency drift and stability deterioration over time (at least at the accuracy level needed for the measurement). Therefore, it is important to find a way for detecting and thereby stabilising the two fundamental parameters f_{rep} and f_0.

The repetition rate f_{rep}, which usually ranges from few tens of MHz to several GHz, can be directly measured through the detection of the pulse train of the laser

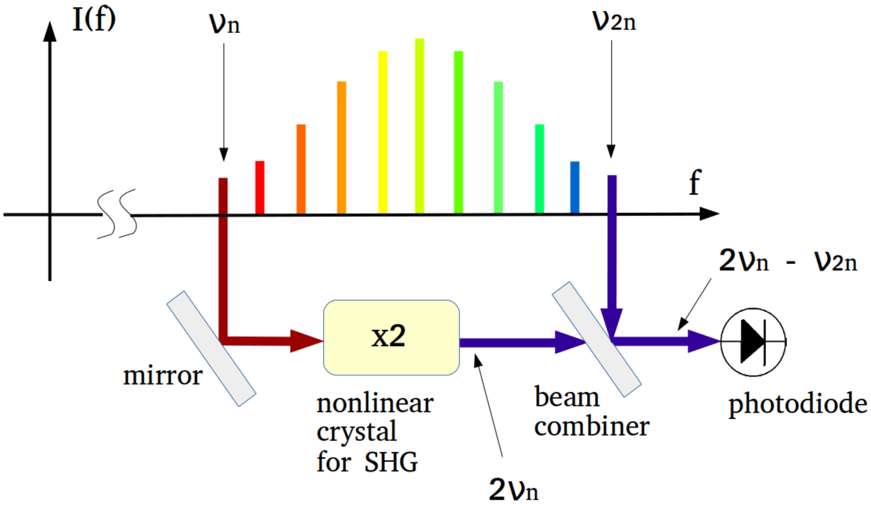

Figure 2.5: $f - 2f$ interferometer scheme for the offset frequency detection. SHG = second harmonic generation.

with a fast photodiode. However, the detected signal does not carry any information about the offset frequency f_0. The demanding requirement of measuring f_0 has represented a critical issue towards the use of mode-locked lasers as frequency combs.

The technique that allows the detection of f_0 is based on the so-called $f - 2f$ interferometer scheme [52]. This is a self-referencing method that relies on an octave-spanning spectrum, i.e. the spectrum highest frequency ν_{max} is at least twice than the lowest frequency ν_{min}, $\nu_{\text{max}} \geq 2\nu_{\text{min}}$. Historically, the main issue was related to the fact that mode-locked lasers did not directly achieved an octave-spanning bandwidth. Spectral broadening of the laser output to achieve such condition (supercontinuum generation) has been achieved by using micro-structured optical fibres. Different physical phenomenons contribute to that process, among which the self-phase modulation plays a dominant role when dealing with high-intensity femtosecond pulses. This is due to the Kerr effect and yields to having pulses with nonlinear phase shift with temporal variability [53].

With the octave-spanning supercontinuum the $f - 2f$ interferometer can be realised as shown in fig. 2.5. One arm of the interferometer consists of the low-frequency region of the spectrum that is frequency-doubled by means of second-harmonic generation (SHG) in a nonlinear crystal, converting the frequency mode ν_m into $2\nu_m$. The other arm is the high-frequency region of the original comb spectrum that includes the mode with index $2m$, ν_{2m}. Using the comb modes' expression given by equation eq. (2.10) we can write

$$\begin{aligned} 2\nu_m &= 2(mf_{\text{rep}} + f_0), \\ \nu_{2m} &= 2mf_{\text{rep}} + f_0. \end{aligned} \tag{2.11}$$

Hence, by mixing $2\nu_m$ and ν_{2m} and detecting their difference frequency with a photodiode we obtain

$$2\nu_m - \nu_{2m} = (2mf_{\text{rep}} + 2f_0) - (2mf_{\text{rep}} + f_0) = f_0, \tag{2.12}$$

which yields exactly the offset frequency.

2.4 Different types of optical combs

The early demonstration of an optical frequency comb was based on Ti:sapphire mode-locked lasers [20, 21]. From then on, frequency combs have found several improvements in terms of reliability, size, output wavelengths and mode spacing [54]. Mode-locked-based frequency combs were demonstrated by using solid-state, semiconductor and fibre-based lasers. In addition, different systems as semiconductor quantum cascade lasers (QCL), modulated CW-lasers and micro-resonators have been also investigated, where the comb is not generated from mode-locked operation. Hereinafter a brief summary of such types of combs is provided.

Solid-state combs Among this type of combs the Ti:sapphire combs have been the most largely used, and they evolved over time. Ti:sapphire combs have central wavelength at 800 nm. Initially, they needed external spectral broadening to build up the $f - 2f$ interferometer [55]. Afterwards, they have become self-referenced systems whit direct octave-spanning output [56]. Improvements have been made also for the repetition rate, which was about a few tens of MHz in the first prototypes and then has been increased up to 10 GHz. Such kind of frequency combs offers the best low-noise performances and the shortest pulses. However, the main drawback is related to the difficulty in achieving stable long-term operation because of the all-bulk-optic setup. Besides the Ti:sapphire-based, other frequency combs have been developed by using Yb:KYW, Yb:KGW, Yb:CALGO, Er:Yb:glass and Cr:LiSAF solid-state lasers, which emit in the 1 µm region [57].

Fibre-laser combs This kind of frequency combs has replaced the Ti:sapphire-based comb for most applications, especially inside metrological research facilities [58]. Indeed, fibre-laser combs take advantage from an all-fibre design that guarantees higher robustness and compactness as compared to solid-state combs. Moreover, fibre-laser combs have emission output that spans roughly between 0.7 µm and 2 µm. That region of the spectrum includes the optimum transmission window of optical fibres, the gain bandwidth of erbium fibre amplifiers and also the advantage of having available several components used in telecommunication. The erbium-doped fibre comb, emitting at 1.56 µm, is nowadays widely employed in several fields and it has gained improvements such as more robustness thanks to an all-polarisation-maintaining design [59]. An high-power fibre-laser comb is the Yb-based one, with central wavelength at 1.04 µm [60].

Semiconductor-based combs Semiconductor systems used to generate optical frequency combs include mode-locked sources or QCL-based devices without pulse generation. In the first case, semiconductor lasers with vertical emission can achieve mode-locking operation when used with semiconductor saturable absorber mirrors, yielding to fs-pulses on a chip-scale platform [61]. On the other hand, semiconductor QCLs are made of multiple quantum well heterostructures stacked together, where the comb structure arises thanks to four-wave mixing processes [62]. Since no optical pulses are produced, the spectral broadening and the modes' stability represent challenging issues for such kind of combs. To date QCLs with access to the offset frequency have not yet been demonstrated, but they still remain interesting systems due to their tunable emission between the mid-IR and the THz regions and the capability of being directly electrically pumped.

Micro-resonator combs The so-called micro-combs are another example of frequency combs that are not generated by mode-locked optical pulses. Micro-combs are based on optical resonators where a CW resonating pump laser is converted to equally-spaced upshifted and downshifted signals by exploiting a parametric four-wave mixing process [63]. Much efforts have been dedicated to the study of the temporal dynamics of the solitons generated inside the resonators, as the pulse generation is crucial for build-up a coherent comb. Nowadays, self-referenced micro-combs without using external broadening modules have been demonstrated [64]. However, low-power output and photonic-integration issues have to be overcome prior to allow the development of reliable chip-based frequency combs.

Electro-optic combs The output of a CW-laser can be modified by using modulators driven by microwave signals. With this technique, optical pulses with tunable repetition rate have been generated. Moreover, the wide-span repetition rate achievable, up to 10 GHz, is the most attractive feature of these devices. Recently, an electro-optic comb with access to the offset frequency has been proved [65], allowing their employment for applications without high-demanding frequency stability [66].

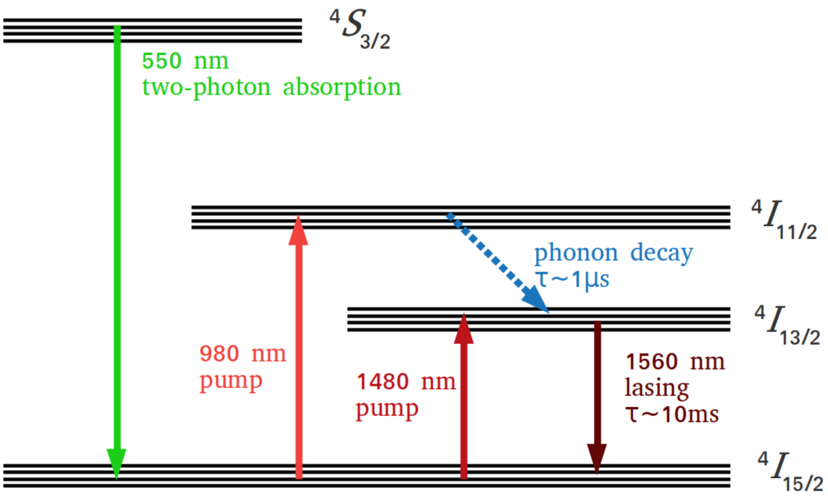

Figure 2.6: Energy level diagram of the erbium-fibre lasing process.

2.5 Erbium-doped fibre combs

Among fibre-based frequency combs, the Er^{3+} ion-based has found large employment over the last years. As a fibre-based system it guarantees robustness and continuous operation for several days without loosing the mode-locked state. Er:fibre combs have central emission wavelength at 1.56 μm, which is particularly interesting since this wavelength is part of the telecommunication C-band. Here minimum losses are experienced in optical fibre transmission (less than 0.2 dB/km at 1.56 μm [67]). However, initially fibre-laser combs were not expected to be competitive with respect to the Ti:sapphire-based ones, due to the fact that they show worse performances regarding both the pulse duration and the relative intensity noise. Despite of this, progresses in the design of erbium-fibre combs have led to produce devices comparable to the Ti:Sapphire-based comb in terms of frequency stability and phase-noise [29, 68, 69], and they have become commercial systems developed worldwide [70–72].

Lasing process

The Er:fibre laser operation relies on a quasi-three-level lasing diagram [73], as can be seen from fig. 2.6. Optical pumping can be performed both at 1480 nm and 980 nm, typically by using diode lasers. When pumping with 1480 nm light the ions are directly excited from the ground level $^4I_{15/2}$ to the $^4I_{13/2}$ level, where they decay by emitting light at 1.56 μm with a lifetime of about 10 ms. In the other case, 980 nm pumping leads to a first excitation to the $^4I_{11/2}$ level, then rapidly decay through a phonon-transition to the $^4I_{13/2}$ level with a lifetime of about 1 μs. Usually the 980 nm pumping is preferred, since it is less noisy and the wavelength is far from the lasing emission value. Finally, note that the ${}^4S_{3/2}$ level can be populated by the pump laser via two-photons absorption and it decays to the ground state emitting green light at 550 nm, which is the typical sparkling colour visible when the fibre medium is pumped.

Mode-locking

Erbium-fibre combs achieve the pulsed operation through passive mode-locking techniques. The most used method is based on the nonlinear polarisation evolution (NPE) effect [74], which has been proposed by Tamura *et al.* [75]. This method relies on the fact that due to the fibre birefringence and the self-phase modulation originating from the Kerr effect, intense pulses travelling into optical fibres show a nonlinear rotation in the polarisation state [76, 77]. Thus, by placing a polarisation selector inside the laser cavity it is possible to allow the transmission of only the most intense pulses. This mechanism works like a saturable absorber and leads to femtosecond pulses thanks to the fast timescale at which the Kerr effect manifests. Alternative mode-locking techniques are based on nonlinear amplifying loop mirror [78, 79] or SESAM placed in a linear fibre cavity [80].

2.6 INRiM Er:fibre comb

2.6.1 Laser cavity

At INRiM we use a commercial MenloSystems Er:fibre comb with repetition rate $f_{\mathrm{rep}} = 250$ MHz. The NPE-based mode-locking is achieved by using a scheme that presents peculiar features as compared to the original Tamura scheme. Indeed, in this case free-space elements replace fibre components leading to a better control of the polarisation, whilst an all-fibre setup remains cheaper an easier to be aligned. Figure 2.7 shows the laser cavity setup. The ${}^{3+}$Er fibre is pumped with a 980 nm diode laser through a wavelength division multiplexer (WDM) and launched in free-space using a collimator. Then two pairs of quarter-wave ($\lambda/4$) and half-wave ($\lambda/2$) plates are used for the polarisation state selection before the light is coupled again into the fibre. After the first two waveplates a polarising beam splitter (PBS1) is used to extract a portion of the beam that provides the comb output and then an isolator guarantees that the pulses travel only counter-clockwise. The piezo actuator mounted on the cavity mirror and the electro-optic modulator (EOM) are used to control the cavity length, and thus f_{rep}. An optical wedge is used to control the cavity dispersion and stabilise f_0. A detailed discussion of the comb parameters' stabilisation is provided in section 2.6.3. Finally, a $\lambda/4$ waveplate is placed before the piezo-mounted mirror so that by passing twice through it the

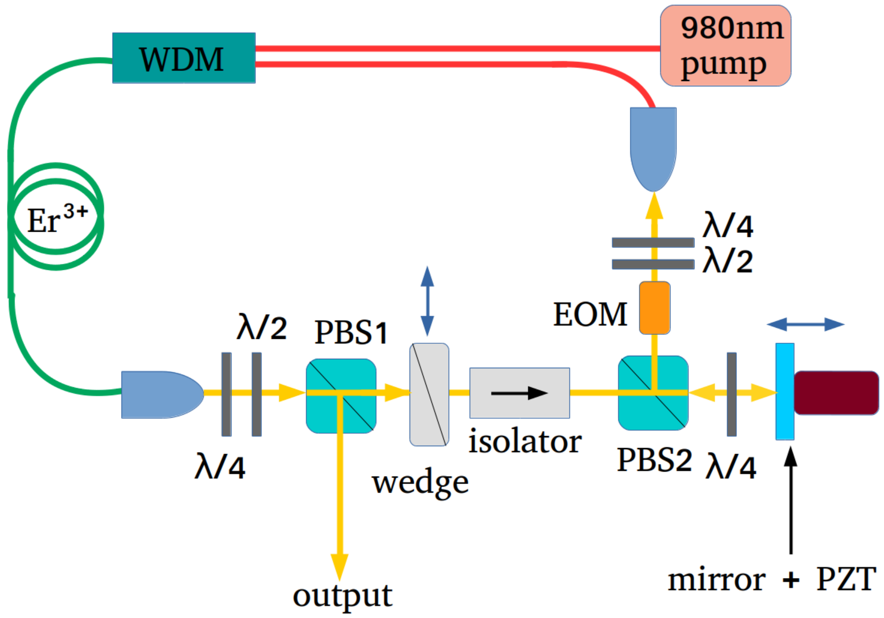

Figure 2.7: Mode-locking scheme of the erbium-fibre femtosecond laser. PBS = Polarizing Beam Splitter; WDM = wavelength division multiplexer; PZT = piezo actuator; blue arrows = direction of movement; EOM = Electro-Optic Modulator; $\lambda/2$ = half-wave plate; $\lambda/4$ = quarter-wave plate.

light polarisation changes of 90°. In this way the beam has the proper polarisation state to be reflected by PBS2 and re-injected into the fibre.

2.6.2 Supercontinuum generation

The femtosecond oscillator output at 1.56 µm is split into five branches that cover different regions of the optical domain (see fig. 2.8), needed for building the $f-2f$ interferometer as well as perform measurements in the visible domain.

1.56 µm-branch The first branch is the main output itself, which is centred at 1.56 µm and 100 nm-wide (see fig. 2.10).

$f-2f$ branch The second branch is designed in order to cover an octave-spanning spectrum between 1 µm and 2.1 µm, allowing the f_0 detection through the $f-2f$ interferometer described in section 2.3. To do that, the comb main output is amplified using an erbium-doped fibre amplifier (EDFA) [73], whose amplification process relies on the same lasing scheme described in section 2.5. Then the spectrum broadening is achieved in a highly-nonlinear fibre (HNLF) by exploiting nonlinear effects among which are self-phase modulation, four-wave mixing and Raman scattering

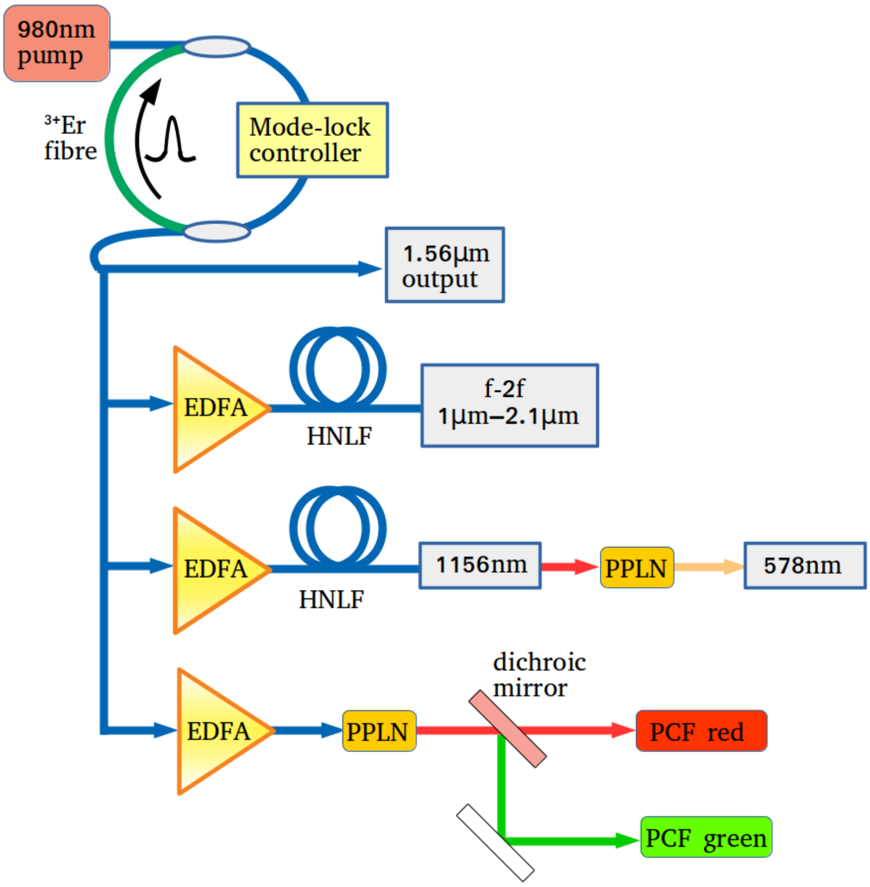

Figure 2.8: Multi-branch configuration of the erbium-fibre comb. EDFA: erbium-doped fibre amplifier; HNLF: highly-nonlinear fibre; PPLN: periodically-poled lithium niobate crystal; PCF: photonic crystal fibre.

[53, 81, 82]. The $f-2f$ interferometer provides an output port with 2.5 mW power that can be used for other measurements. Its spectrum recorded on a optical spectrum analyser (OSA) is shown in Figure 2.11, where the limitation on the maximum wavelength is given by the instrument. With the available $f-2f$ power, beatnote signals with signal-to-noise ratio (SNR) sufficient to be counted can be detected in particular between 1000 nm and 1100 nm. However, a compromise between having enough power to detect f_0 and measuring at the same time a desired laser has to be found when the broadband power spectrum of the $f-2f$ branch is optimised in specific regions. In our laboratories the $f-2f$ branch allows the measurement of the 1156 nm diode laser used to generate the 578 nm local oscillator of our operating ^{171}Yb optical lattice clock [35]. The 1156 nm laser's measurement with the $f-2f$ branch will be detailed in section 3.3.1. In addition, we are developing an UV laser source to be used for frequency metrology and spectroscopy, which is

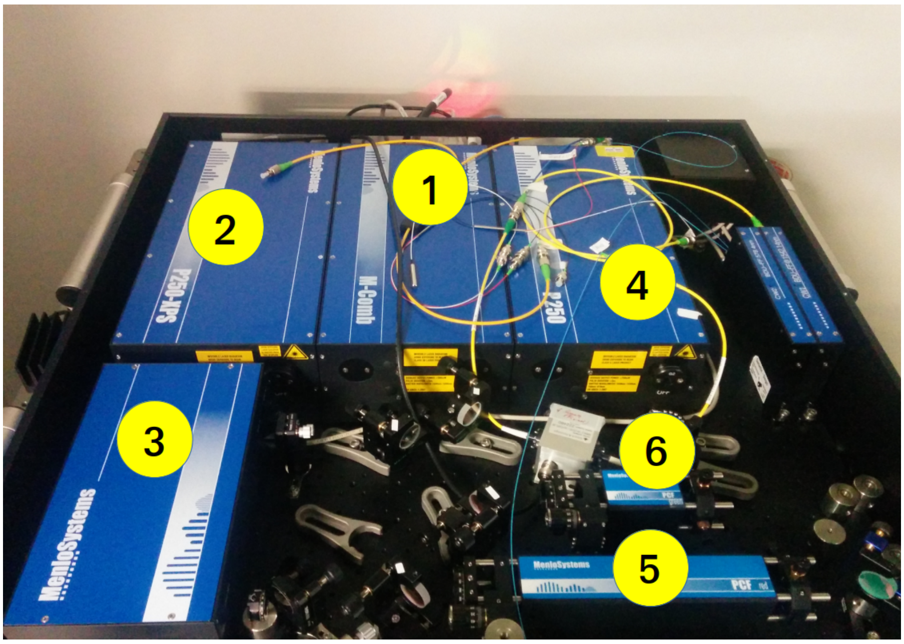

Figure 2.9: Picture of the Er:fibre comb package. 1: Er:fibre femtosecond oscillator module; 2: $f - 2f$ interferometer and EDFA and HNLF for wavelength-shifting to 1156 nm; 3: second-harmonic generation at 578 nm by using the 1156 nm output of module 2; 4: second-harmonic generation at 780 nm by using the 1.56 µm output amplified with an EDFA; 5-6: spectrum broadening using red (5) and green (6) PCFs.

obtained from frequency-quadrupling a 1016 nm diode laser. The detection of the 1016 nm seed laser with the $f - 2f$ branch allows the measurement and possible future stabilisation of the laser to the comb.

578 nm-branch The third branch generates light at 578 nm with ~ 5 mW output power, which is of interest since we need to measure the 578 nm clock transition of the ^{171}Yb optical lattice clock [35]. Details about the 578 nm laser's measurement will be provided in section 3.3.1. The 578 nm branch consists of a second EDFA that amplifies the main comb output at 1.56 µm, followed by a HNLF. This is a Raman fibre operated as a wavelength-shifting module used to obtain light at 1156 nm. Frequency-doubling to 578 nm is obtained via a bulk periodically-poled lithium niobate (PPLN) crystal [83] mounted in a temperature-controlled oven for optimising the crystal phase-matching and minimising the temperature effects on the second-harmonic generation.

Visible-domain branhces The fourth and fifth branches broaden the spectrum in the visible domain, spanning roughly from 500 nm to 950 nm. A third EDFA is used to provide high-power light at 1.56 µm. This is sent to a PPLN crystal that

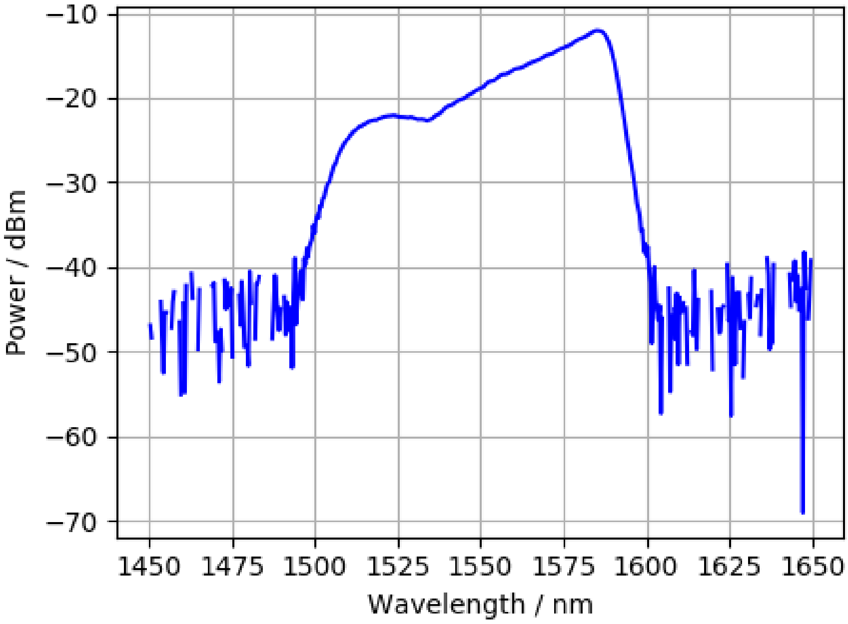

Figure 2.10: 1.56 µm comb output power spectrum recorded using an OSA with resolution bandwidth RBW = 1 nm.

generates 780 nm second-harmonic and 530 nm third-harmonic signals used as seeds to feed red and green photonic crystal fibres (PCFs). PCFs achieve supercontinuum generation through their internal structure made of tiny air holes that enhance the refractive index variation between regions with holes and the surrounding material [84]. The comb branch generated thorugh the red PCF is particularly useful in our laboratories for measuring the 759 nm lattice laser of the Yb clock [85]. By optimising the PCF in the lattice laser region, beatnote signals with SNR > 30 dB in a 100 kHz resolution bandwidth (RBW) can be obtained.

Each EDFA is optically pumped using four 980 nm diode lasers. By changing the currents of the pump lasers the spectrum of each branch can be tailored for maximising the power in the regions of interest.

2.6.3 Comb stabilisation

The entire comb spectrum can be phase-stabilised by controlling the two parameters f_0 and f_{rep}. Two main approaches can be implemented to stabilise the frequency comb. The first one is realised by phase-locking both of them to an RF-oscillator. In a second approach, f_0 and the beatnote between a comb mode and an optical oscillator are stabilised to an RF reference. This indirectly stabilises all

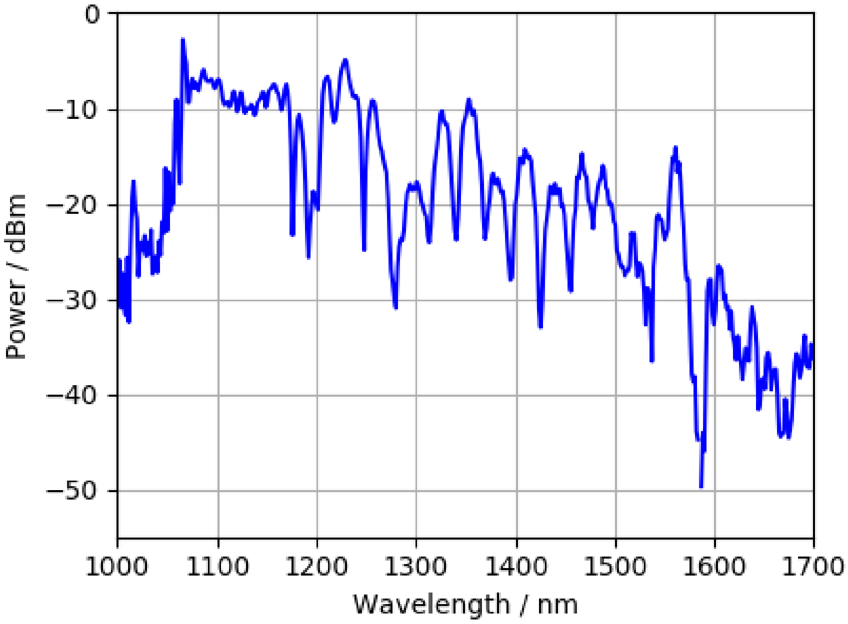

Figure 2.11: $f - 2f$-branch power spectrum recorded using an OSA with resolution bandwidth RBW = 1 nm. The upper limit on the wavelength is set by the instrument.

comb teeth and the repetition rate as a consequence. The latter method is preferable when a narrow-linewidth comb is required, since the phase-noise properties of the optical reference can be coherently transferred over the comb spectrum [86–88]. Furthermore, referencing the comb to an ultrastable optical source can allow the generation of low-noise microwave signal by using the comb as a frequency divider from the optical to the microwave domain [42, 89, 90]. Indeed, by detecting an harmonic of the repetition rate a microwave signal with the same stability as the optical oscillator can be obtained. Being m the index of the comb tooth used for the stabilisation and n the index of the f_{rep} harmonic, in principle microwave sources with phase-noise a factor 20 $\log(m/n)$ lower with respect to the optical domain can be generated.

Repetition rate f_{rep}: detection and stabilisation

A sketch of the f_{rep} stabilisation to an RF oscillator is shown in fig. 2.12. In this case the fourth harmonic of the repetition rate at 1 GHz is directly detected at the femtosecond oscillator output and then mixed with a digital resonator oscillator (DRO) tuned to 980 MHz. The choice of stabilising the n^{th} harmonic of f_{rep} $(n = 4)$ instead of the fundamental tone is due to the fact that the m^{th} optical comb tooth has phase noise a factor 20 $\log(m/n)$ greater than the reference. Afterwards, the

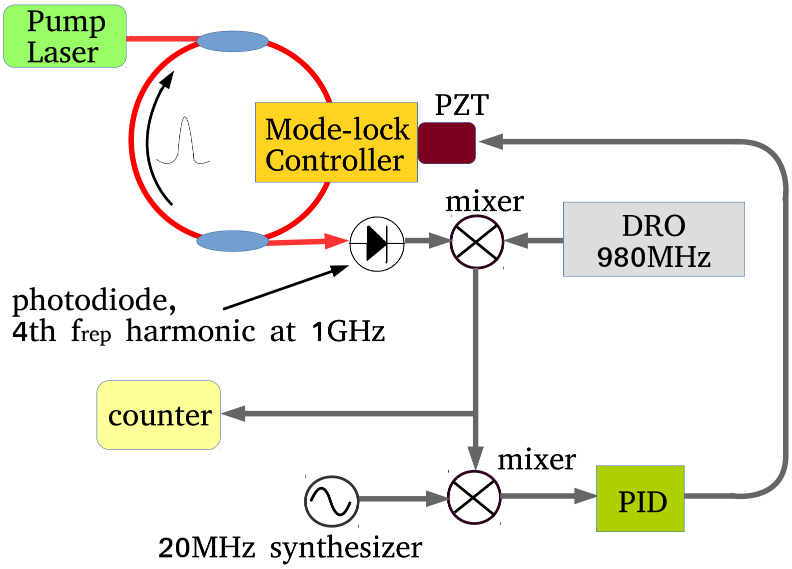

Figure 2.12: Scheme of the detection and the optical stabilisation of the repetition rate f_{rep}. PZT: piezo actuator; DRO: digital resonator oscillator; PID: proportional-integral-derivative controller.

frequency difference between the f_{rep} harmonic and the DRO is counted and down-converted to DC with a synthesiser tuned to 20 MHz. The error signal generated in this way is sent to a proportional-integrative-derivative (PID) controller that acts on the piezo of the laser cavity mirror. In this way, the cavity length and thus f_{rep} can be stabilised on a bandwidth of 3.5 kHz. The synthesisers and the counters are referenced to one of the INRiM hydrogen masers, which in turns is measured by the INRiM caesium fountain ITCsF2 [91]. Through this scheme the repetition rate is phase-locked to the H-maser, with a fractional instability of about $1-2\times 10^{-13}$ at 1 s of averaging time.

On the other hand, the optical stabilisation of f_{rep} is achieved by phase-stabilising the beatnote between one comb mode and the CW-laser used as the optical reference (see fig. 2.13). Our comb electronics requires the beatnote to be at 60 MHz. If this value cannot be directly achieved, frequency conversion can be exploited by mixing the beatnote with a local oscillator. Hence in this case the error signal used to feed the PID is generated from the down-conversion to DC of the optical beatnote. Considering the fact that the signal to be stabilised is a beatnote between optical oscillators, the phase-noise is multiplied by a factor m/n of about 10^4-10^6. The low bandwidth of the piezo cannot sustain the PLL operation with such kind of high phase-noise. Therefore, a faster actuator is used together with the piezo, which is an intra-cavity EOM crystal with a 200 kHz bandwidth.

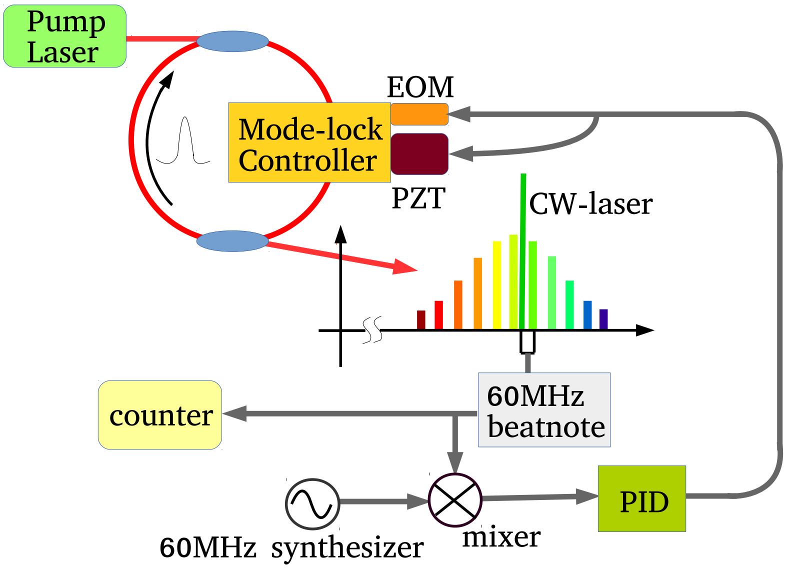

Figure 2.13: Scheme of the detection and the optical stabilisation of the repetition rate f_{rep}. EOM: electro-optical modulator crystal; PZT: piezo actuator; PID; proportional-integral-derivative controller.

Offset frequency f_0: detection and stabilisation

The offset frequency is detected using an $f - 2f$ interferometer scheme (see section 2.3). The stabilisation of f_0 is performed by acting on the dispersion of the laser cavity, since this parameter is sensitive to the phase velocity variations of the mode-locked pulses. A fine tuning of f_0 is obtained by changing the refractive index, hence the dispersion, of the active medium by varying the pump laser's power, while a coarse tuning is achieved by using an intra-cavity optical double-wedge (see fig. 2.7). The wedge is composed by two plane-inclined surface prisms with slightly different refractive indexes n_1 and n_2 such that

$$\begin{aligned} n_1 &= n_0 + \frac{\partial n_1}{\partial \lambda}(\lambda - \lambda_0), \\ n_2 &= n_0 + \frac{\partial n_2}{\partial \lambda}(\lambda - \lambda_0). \end{aligned} \tag{2.13}$$

By perpendicularly moving the wedge with respect to the propagation direction of the laser pulses the total thickness of the glass does not change, thus the group delay is not affected. On the contrary, the quantity $\partial n/\partial \lambda$ changes yielding to a variation of the group delay dispersion and consequently of f_0. As shown in fig. 2.14, f_0 is tuned to 20 MHz and both counted and fed into a phase detector, where is down-converted to DC using the frequency-doubled signal extracted from

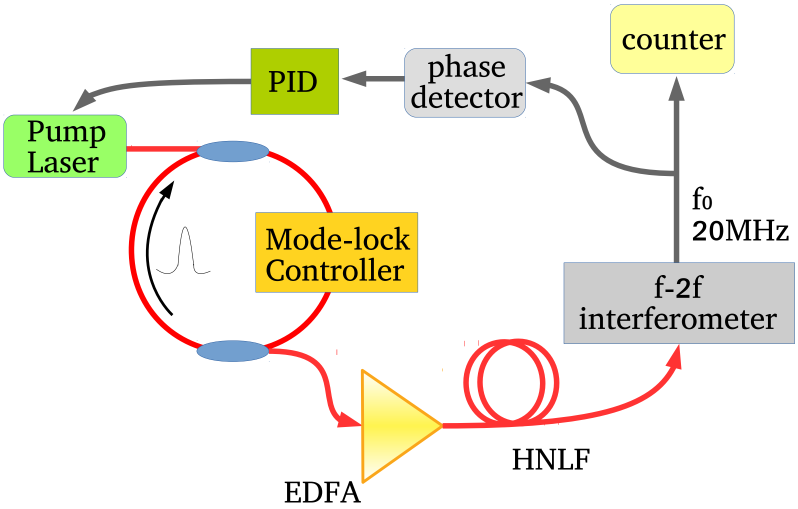

Figure 2.14: Scheme of the detection and the RF-stabilisation of the offset frequency f_0. EDFA: erbium-doped fibre amplifier; HNLF: highly-nonlinear fibre; PID: proportional-integral-derivative controller.

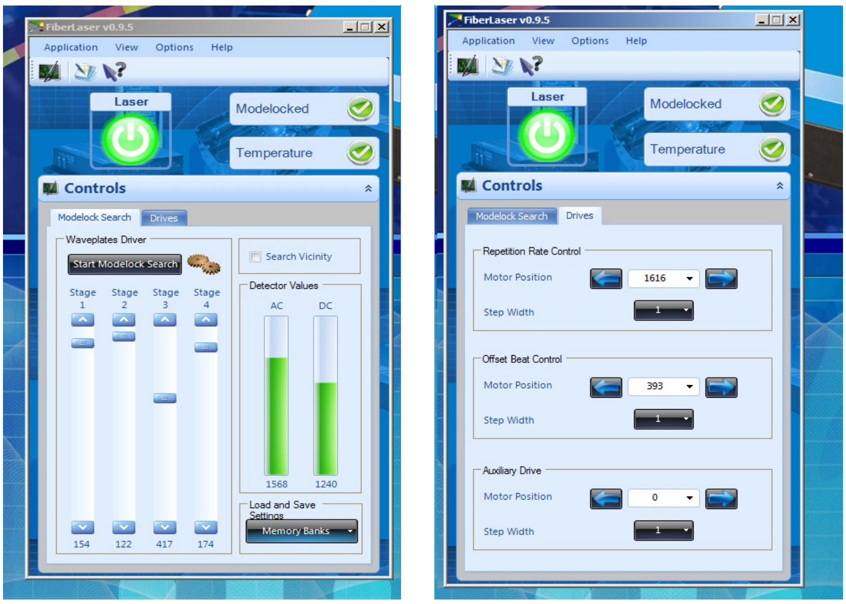

Stage 1: 154
Stage 2: 122
Stage 3: 417
Stage 4: 174
AC: 1568
DC: 1240

Repetition Rate Control
Motor Position: 1616
Step Width: 1

Offset Beat Control
Motor Position: 393
Step Width: 1

Auxiliary Drive
Motor Position: 0
Step Width: 1

Figure 2.15: Software interface used to control the comb mode-locking and to adjust f_0 and f_{rep}.

the 10 MHz output of the H-maser. The phase detector output is then sent to a PID controller that acts on the laser pump power.

Software control The erbium-fibre mode-locking is controlled via the FiberLaser software provided by MenloSystem. The software interface, shown in fig. 2.15, consists of a control window on the left-hand that allows the mode-locking search by rotating the four waveplates placed inside the laser cavity. Instead, on the right-hand of the interface is possible to change f_0 and f_{rep} with adjustable step width.

Chapter 3

Universal frequency synthesiser using an Er:fibre comb

Besides the fundamental role of frequency combs as rulers for measuring optical frequencies, in recent years they emerged also as a tool for transferring the spectral purity of ultrastable oscillators [87, 88, 92–94]. Thanks to their structure, optical combs allow the transfer of the performances of high-finesse optical cavities across the optical domain or from the optical to the microwave domain. This capability is beneficial to high-resolution spectroscopy in different regions of the optical domain [95] and generation of low-noise microwave signals [42].

Particularly, within a metrology laboratory where different optical atomic clocks are operated, there is the need of having ultrastable lasers available at different wavelengths. Such lasers are employed as local oscillators for interrogating the narrow-linewidth clock transitions and thus they determine the stability of the clocks [96]. The best ultrastable sources available today are based on developing cryogenic systems to reduce the thermal-noise floor [97, 98], as well as using special mirrors (such as crystalline coatings [99, 100]) and increasing the cavity length [101]. As a result, ultrastable lasers can reach fractional frequency stability in the low 10^{-17} regime [102, 103]. Moreover, the best stability results have been demonstrated only for specific wavelengths in the infrared domain [104].

Optical combs provide a powerful solution for simplifying the laboratory setup when more than one ultrastable cavity has to be developed. Thanks to the transfer oscillator technique, it is possible to use a single ultrastable cavity as a reference for multiple laser sources. This provides advantages also for the comparison of atomic clocks based on different atoms. Indeed, when the optical clocks use independent probe lasers, the stability is limited by the Dick effect [96]. This limit can be reduced if a single cavity is used as a reference for different probe lasers, as in this case the probe frequency noise is in common-mode [105–107]. Carrying on such kind of comparisons will provide more evidences to sustain a future redefinition of the SI second, and improve the International Atomic Time (TAI) evaluation by using optical clocks [108–110].

This chapter reports on the spectral purity transfer between the 1156 nm and 1542 nm spectral regions we performed at INRiM by using our Er:fibre frequency comb. The results presented are published in [111]. The reference laser used is a cavity-stabilised diode laser that is frequency-doubled and employed for interrogating the ^{171}Yb optical lattice clock transition [34, 35]. Its frequency instability is about 2×10^{-15} at 1 s of averaging time and it is currently the laser source with the highest stability in our laboratories. We transfer its properties to a 1542 nm diode laser that is used for frequency dissemination over fibre to several research institutes using the phase-stabilised fibre link network that we have developed in Italy [112]. This setup will allow the dissemination of our Yb clock. Furthermore, we plan to use the same technique to generate the 698 nm clock laser needed for our ^{87}Sr optical lattice clock that is under development [113].

3.1 Spectral purity transfer using optical combs

The purpose of the spectral transfer is to copy the superior stability of an ultrastable laser, called the master laser, to optical and microwave sources. Specifically, in the case of optical-to-optical transfer we want to phase-lock two lasers whose frequency difference is too large to be measured on a photodiode. The frequency comb can be used to cancel the gap between distant regions of the optical domain, which can be attained using two main approaches.

Locking the comb to an ultrastable laser

The first method consists in locking the repetition rate of the comb f_{rep} to the master laser [95, 114], following the procedure described in section 2.6.3. Both the master and the slave lasers are beaten with the nearest comb tooth. The absolute frequencies ν_{M} and ν_{S} of the two lasers in terms of the comb parameters are

$$\begin{aligned} \nu_{\mathrm{M}} &= m_{\mathrm{M}} f_{\mathrm{rep}} + f_0 + f_{\mathrm{b,M}}, \\ \nu_{\mathrm{S}} &= m_{\mathrm{S}} f_{\mathrm{rep}} + f_0 + f_{\mathrm{b,S}}. \end{aligned} \tag{3.1}$$

where $f_{\mathrm{b,M}}$ and $f_{\mathrm{b,S}}$ are the master and slave laser beatnote signals and m_{S} and m_{M} the numbers of the comb modes with which the two lasers are beaten. As can be seen from fig. 3.1, the beatnotes are mixed with the offset frequency f_0 in order to get rid of its contribution, generating the f_0-free beatnotes ν_{A} and ν_{B}:

$$\begin{aligned} \nu_{\mathrm{A}} &= f_0 + f_{\mathrm{b,S}}, \\ \nu_{\mathrm{B}} &= f_0 + f_{\mathrm{b,M}}. \end{aligned} \tag{3.2}$$

Afterwards, they are down-converted to DC to phase-lock the comb to the master laser and the slave laser to the comb mode with which it is beaten. One of the

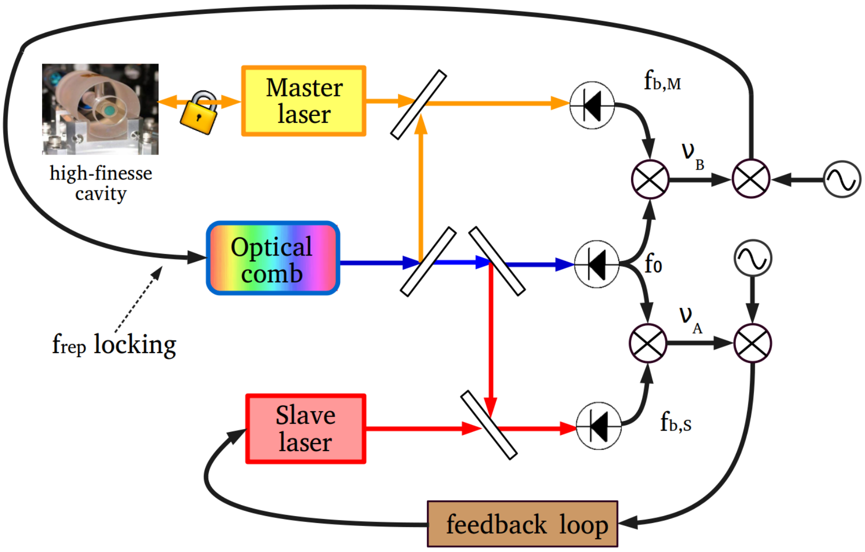

Figure 3.1: Spectral purity transfer scheme by locking the comb f_{rep} to an ultrastable laser.

advantages of this method is the generation of comb modes with higher power compared to the RF-stabilisation, since the power is concentrated in a narrower bandwidth. On the other hand, the main drawback is that the comb repetition rate contribution is not cancelled out, leading to deal with an additional noise source in the transfer scheme besides the contributions given by the electronics and the optical interferometers.

Transfer oscillator technique

In order to completely avoid any contribution of the frequency comb in the spectral purity transfer the so-called transfer oscillator technique proposed by Telle *et al.* can be implemented [28]. As can be seen in fig. 3.2, firstly the two lasers are again beaten with a comb mode. Then the two f_0-free signals ν_{A} and ν_{B}^* are generated, being

$$\nu_{\text{B}}^* = (f_0 + f_{\text{b,M}})\frac{m_{\text{S}}}{m_{\text{M}}}. \tag{3.3}$$

Thus in this case one of the two f_0-free beatnotes is scaled by the comb mode numbers' ratio, which is made by using a direct digital synthesiser (DDS). Finally, the so-called transfer beatnote signal ν_{T} is obtained from the difference signal between ν_{A} and ν_{B}^*:

$$\nu_{\text{T}} = \nu_{\text{A}} - \nu_{\text{B}}^* = \nu_{\text{S}} - \nu_{\text{M}}\frac{m_{\text{S}}}{m_{\text{M}}}. \tag{3.4}$$

From eq. (3.4) we can note that the transfer beatnote expression does not include any comb parameter, as the dependence on f_0 has been removed a priori, and

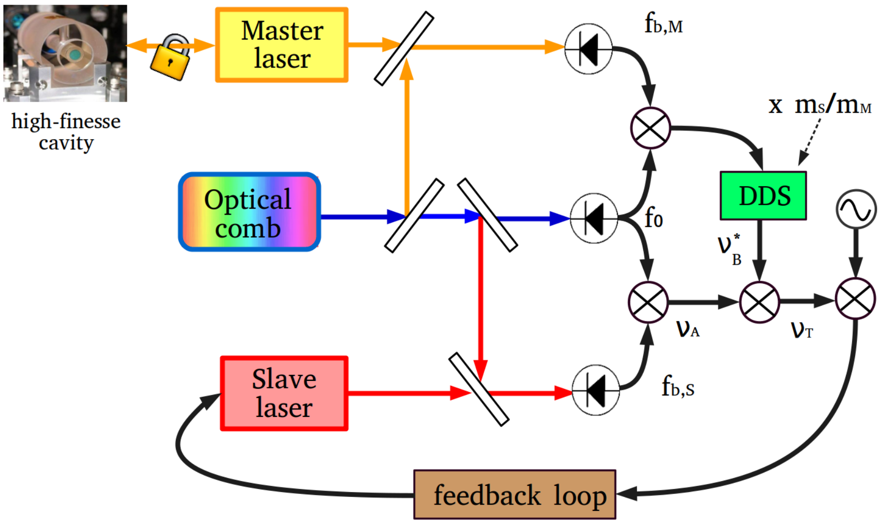

Figure 3.2: Spectral purity transfer scheme by using the transfer oscillator technique. DDS: direct digital synthesiser.

the multiplication factor equal to the ratio of the comb mode numbers allows the scaling between the two optical frequency domains. Then ν_{T} can be used to produce an error signal to be sent to the phase-locked loop that acts on the slave laser. Since through this scheme f_{rep} is cancelled out, the residual noise contributions to the spectral transfer are related to the electronic and optical setups, which have to be characterised and minimised as well as possible to improve the transfer performances. In principle both f_0 and f_{rep} do not require stabilisation. However, usually the comb is locked to an RF source to keep the beatnote signals inside the filters' bandwidth. For our experiment we phase-lock both f_0 and f_{rep} to the H-maser as described in section 2.6.3.

Moreover, it is straightforward to note that by simply dividing eq. (3.4) by the optical frequency ν_{S} we obtain the frequency ratio

$$r = \frac{\nu_{\mathrm{M}}}{\nu_{\mathrm{S}}} = \frac{m_{\mathrm{M}}}{m_{\mathrm{S}}}\left(1 - \frac{\nu_{\mathrm{T}}}{\nu_{\mathrm{S}}}\right). \tag{3.5}$$

In case the master and slave lasers are used to probe different clocks, the measurement of ν_{T} gives direct access to the clocks' frequency ratio [107, 115], as will be described in section 4.2. The uncertainty of the ratio r can be expressed as

$$\delta r = \frac{m_{\mathrm{M}}}{m_{\mathrm{S}}}\sqrt{\left(\frac{\delta\nu_{\mathrm{T}}}{\nu_{\mathrm{S}}}\right)^2 + \left(\frac{\nu_{\mathrm{T}}}{\nu_{\mathrm{S}}}\frac{\delta\nu_{\mathrm{S}}}{\nu_{\mathrm{S}}}\right)^2}. \tag{3.6}$$

Since ν_{T} is in the range of tens of MHz, δr is dominated by the uncertainty of the first term. Therefore, in order to measure frequency ratios below the 10^{-18}

level one has to measure the transfer beatnote ν_T with a relative uncertainty of 10^{-11} or better. This would require, for instance, a frequency counter with 12-digit resolution for measuring a transfer beatnote $\nu_\mathrm{T} = 100$ MHz. Optical frequency ratio measurements performed through the transfer oscillator scheme have been demonstrated with a relative uncertainty in the low 10^{-19} already in the early 2000s [116] and more recently up to the 10^{-21} level [29].

Finally, we note that frequency ratio measurements can be realised by either developing the full hardware setup of fig. 3.2 or alternatively by processing the detected comb parameters f_0 and f_rep and the lasers' beatnote $f_\mathrm{b,M}$ and $f_\mathrm{b,S}$. In the first case the most important element of the electronics is the DDS, whose number of bits determines how faithfully the comb mode ratio $m_\mathrm{M}/m_\mathrm{S}$ can be reproduced. Instead, for the software implementation a proper digital format has to be chosen to avoid degradation of the accuracy during the data processing. In addition, a good synchronisation between the beatnote measurements is required. This is typically achieved by using a single, multi-channel phasemeter.

3.2 Multi-branch and single-branch combs

Multi-branch frequency combs are developed to select specific regions of interest throughout the optical spectrum by means of dedicated amplifiers and optics modules. In this way it is possible to increase the available comb power and to reach wavelengths outside the native spectrum of the comb. However, the several elements employed to build-up the comb branches leads to uncommon noise that has to be carefully evaluated, since it could limit the spectral transfer between two or more branches [87].

Er:fibre combs have a natively output that ranges between 1 µm and 2 µm. Therefore, when multiple wavelengths in the visible domain have to be measured or power enhancement in the 1-2 µm region is needed, a multi-branch configuration is implemented [87, 92, 117–119]. Each branch is amplified using a dedicated EDFA and different wavelength regions are achieved by using SHG crystals, HNLFs and PCFs (see section 2.6.2). As a result, a multi-branch configuration provides comb outputs with enough power to generate high-SNR beatnote signals. Although the transfer oscillator technique allows cancellation of the femtosecond oscillator contribution, all the additional noise sources related to the independent optics paths of the comb branches are not suppressed.

Alternatively, one can think of of using the same comb branch (single-branch approach [93, 94, 120]) for measuring all the wavelengths of interest. In this way the wavelength-conversion modules' noise is cancelled out as it is in common-mode. However, with single-branch combs, it is difficult to obtain sufficient power to detect high-SNR beatnotes at multiple wavelengths simultaneously. For this reason usually tracking oscillators are employed. In addition, locking the comb repetition rate to a narrow-linewidth laser could improve the beatnotes' SNR [93]. In this case, as mentioned in the previous section, the comb modes' power would be concentrated in a narrower bandwidth, allowing a better filtering of the beatnote signals.

Frequency combs used for optical clock comparison and spectral purity transfer have to cope with the requirements set by the contemporary optical atomic clocks, which achieve accuracy of few parts in 10^{-18} and have stability that averages down as $1 \times 10^{-16}(\tau/\mathrm{s})^{-1/2}$ [121–124], as well as state-of-the art ultrastable lasers that reach the low 10^{-17} of fractional stability in few seconds of averaging time (while for longer timescales the stability is deteriorated by frequency drift) [97, 103]. Multi-branch combs demonstrated so far achieve instability of few parts in 10^{-17} at $\tau = 1$ s [125], typically averaging down as $(\tau/\mathrm{s})^{-1/2}$, while single-branch comb performances are one order of magnitude better, with stability of few parts in 10^{-18} at $\tau = 1$ s [93]. In a recent work a multi-branch comb that overcomes the typical limitations of such kind of system has been demonstrated [126]. In this experiment the inter-branch noise is actively suppressed, leading to the same performances of a single-branch system. This kind of setup will be useful in view of growing requirements in terms of accuracy and instability.

The following sections report on the spectral purity transfer performed by using our multi-branch Er:fibre comb by separately addressing the characterisation of the different noise contributions. The residual noise due to the multi-branch comb configuration is discussed in section 3.4. We evaluated the inter-branch noise between the $f - 2f$ and 578 nm comb branches by measuring the 1156 nm laser and its second-harmonic on the two branches. By measuring the same 1542 nm laser on the the $f - 2f$ and 1.56 µm branches the corresponding inter-branch noise is also quantified. Section 3.5 reports on the characterisation of the electronics noise related to the transfer oscillator scheme. Finally, the spectral purity transfer between the 1156 nm and 1542 nm lasers is described in section 3.6.

Firstly, in the next section the laser sources involved in the spectral transfer are presented, as well as their detection on the comb branches.

3.3 Laser sources and beatnote detection

1156 nm master laser

The master laser is the ultrastable laser used to probe the 578 nm ${}^1\mathrm{S}_0 - {}^3\mathrm{P}_0$ clock transition of the INRiM ^{171}Yb optical lattice clock [34, 35]. It is a 1156 diode laser that is frequency-doubled to 578 nm by using a waveguide periodically-poled lithium niobate (PPLN) crystal, which generates about 9 mW of yellow light. After the doubling process 4 mW of the 1156 nm seed radiation are still available. A fraction of the output light at 578 nm, 10 µW, is used to stabilise the laser to an ultrastable 10 cm-long Fabry-Pérot cavity through the Pound-Drever-Hall technique [127, 128].

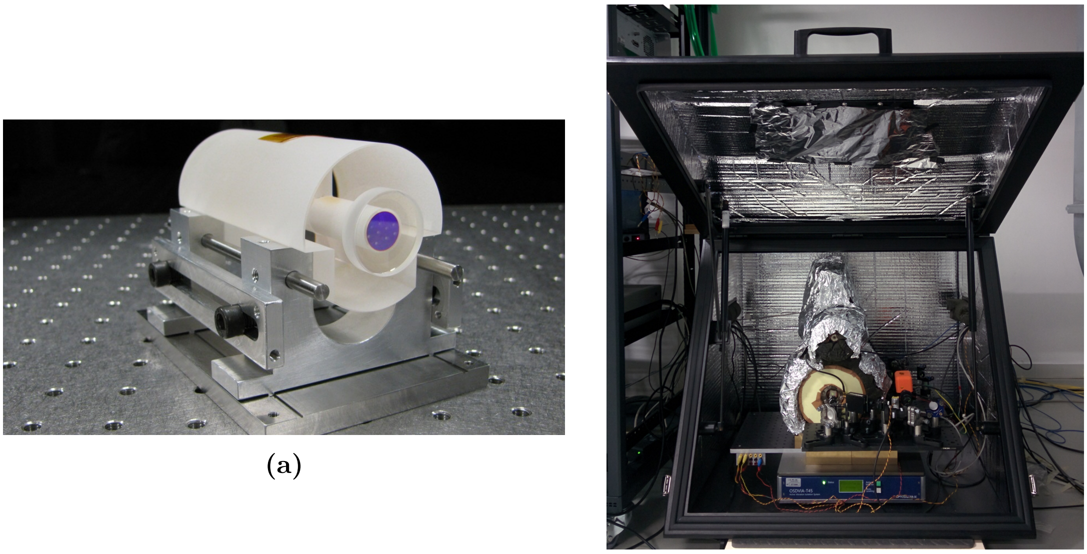

(a) **(b)**

Figure 3.3: The master laser's ultrastable cavity. (a) Picture of the ULE ultrastable cavity. (b) Picture of the ULE cavity surrounded by the vacuum chamber and placed inside the acoustic enclosure.

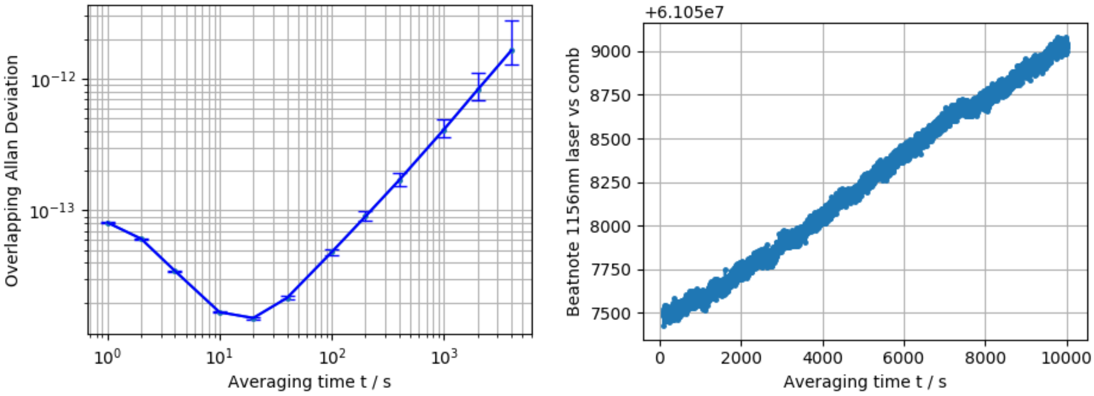

(a) **(b)**

Figure 3.4: Measurements of the beatnote between the master laser and the comb. (a) Overlapping Allan deviation of the beatnote signal between the comb locked to the H-maser and the 1156 nm laser locked to the ultrastable cavity. (b) Raw data of the beatnote signal between the comb locked to the H-maser and the 1156 nm laser locked to the ultrastable cavity.

The cavity has a ultra-low expansion (ULE) spacer and fused silica mirrors with

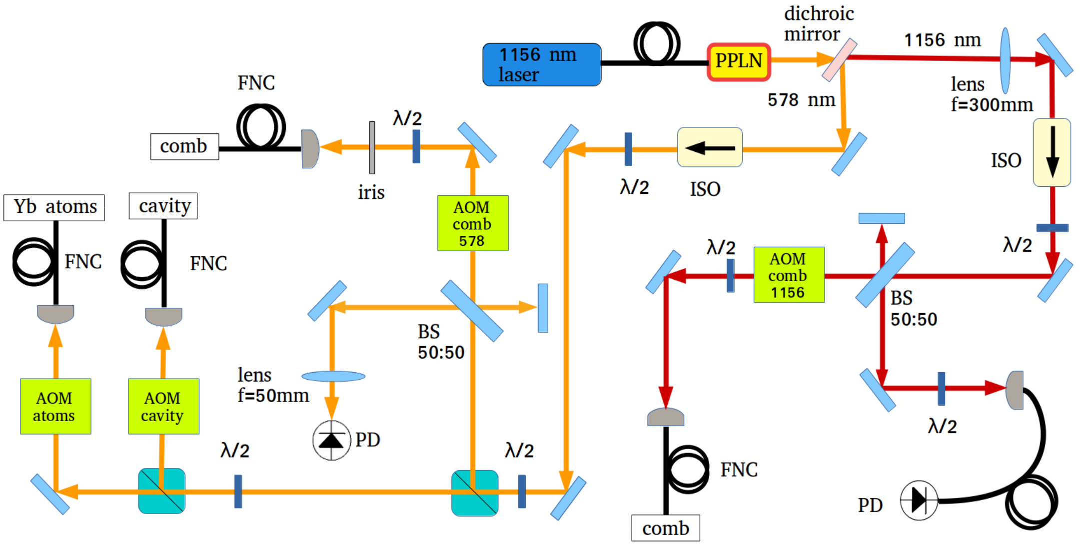

Figure 3.5: Optical setup for the 1156 nm laser dissemination. PPLN: periodically-poled lithium niobate crystal; ISO: isolator; AOM: acousto-optic modulator; BS: beam splitter; FNC: fibre-noise cancellation; PD: photodiode.

coatings optimised for 578 nm, and finesse of 224 000. It is housed in a temperature-controlled vacuum chamber and the whole package is placed on an active-vibration-isolation platform to suppress seismic noise (see pictures in fig. 3.3). An acoustic box encloses the whole system. Such a laser achieves fractional stability of 2×10^{-15} at 1 s, inferred from interleaved measurements of the ^{171}Yb optical clock that are Dick-effect limited [129]. The cavity drift is assessed to be 0.15 Hz/s by measuring the beatnote between the 1156 nm radiation and the comb referenced to the H-maser (see section 3.3.1 for the 1156 nm measurement details). The fractional instability of the measurement is shown in terms of overlapping Allan deviation [130, 131] in fig. 3.4. For timescales between 1 s and 10 s the stability is limited by the RF-stabilisation of the comb, which following the H-maser reference decreases as $(\tau/\mathrm{s})^{-1/2}$ for $\tau > 10$ s. For averaging time greater than 10 s the cavity drift emerges and can be quantified.

The master laser is delivered to the Yb clock experiment and the comb laboratory through the setup shown in fig. 3.5. The free-space output of the PPLN is sent to a long-pass dichroic mirror used to separate the residual radiation at 1156 nm from the frequency-doubled light. The 1156 nm light is entirely sent to the comb, while the 578 nm light is split into three branches needed for locking the master laser to the ultrastable cavity, performing spectroscopy of the Yb atoms and measuring the beatnote with the comb on the visible branch. All paths are established through polarisation-maintaining (PM) fibres, which are phase-stabilised by using a Doppler-stabilisation technique [132, 133]. Four AOMs are used to compensate for the fibre-noise, one for each branch (see fig. 3.5).

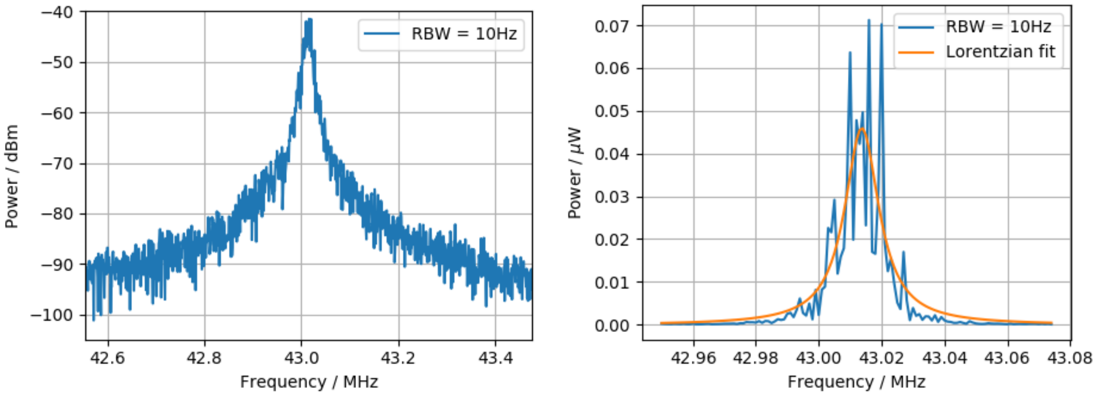

(a) **(b)**

Figure 3.6: Beatnote signal between the free-running slave laser and the 1542 nm ultrastable laser. (a) Beatnote signal recorded with a spectrum analyser, RBW = 10 Hz. (b) Lorentzian fit of the beatnote.

1542 nm slave laser

The slave laser is a 1542 nm external-cavity diode laser that is frequency-tuned by changing either the driving current or the temperature [134]. The output wavelength can be tuned in the range 1541.9-1542.5 nm by changing the temperature, with a power that varies from -7 dBm to 9 dBm. The laser's linewidth has been inferred through a beatnote measurement between the free-running laser and a cavity-stabilised laser (shown in fig. 3.6). Using a Lorentzian fit a linewidth Γ of $\sim$ 13 kHz is estimated. The long-term frequency variations are about few MHz over few hours. With such kind of laser there is no need of implementing a frequency pre-stabilisation for using it in our transfer oscillator setup.

3.3.1 Beatnote signals' detection

The beatnotes of the 1156 nm master laser and its frequency-doubled 578 nm component with the comb are detected through free-space interferometers. The 1156 nm light is beaten with the $f-2f$ branch, while the 578 nm light is detected on the 578 nm dedicated comb branch. The 1542 nm laser is detected by beating to the 1.56 µm comb output. Figure 3.7 outlines the measurement configuration with all the laser sources involved.

The master laser light and its second harmonic are sent from the Yb clock laboratory to the comb laboratory using two 20 m-long phase-stabilised PM-fibres. The slave laser is sent to the comb optical bench by using a standard telecom non-PM fibre, which is not phase-stabilised. No active stabilization of the comb path is adopted and the system relies on passive thermal insulation. The optical comb and

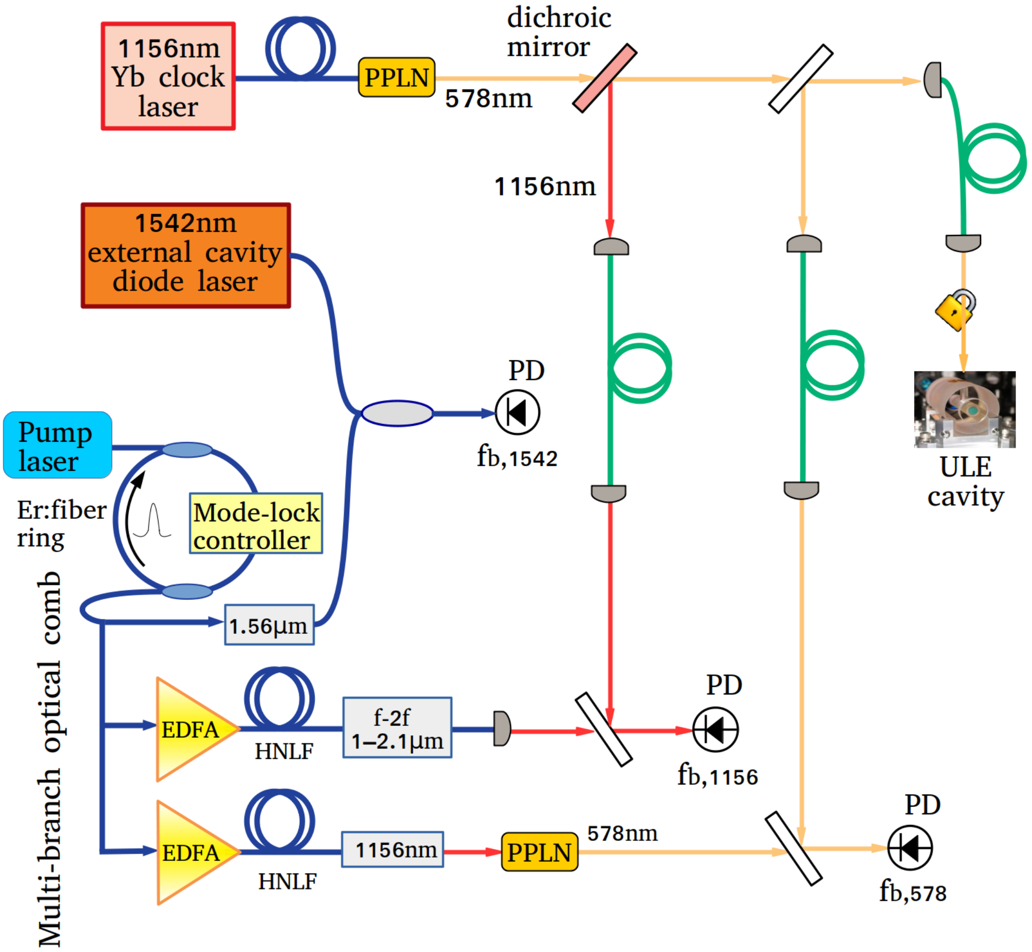

Figure 3.7: Measurement scheme of the beatnotes' detection between the master and slave lasers and the comb branches. Green lines: phase-stabilised optical fibres; blue lines: uncompensated optical fibres; red and yellow lines: free-space paths, referring to the 1156 nm and 578 nm respectively; PPLN: periodically-poled lithium niobate crystal; EDFA: erbium-doped fibre amplifier; HNLF: highly-nonlinear fibre; ULE: ultra-low expansion glass; PD: photodiode.

the interferometers are enclosed inside a foam box in order to mitigate the effect of temperature variations and air currents on the fibres. The laboratory hosting the comb is temperature-stabilised at 296 K.

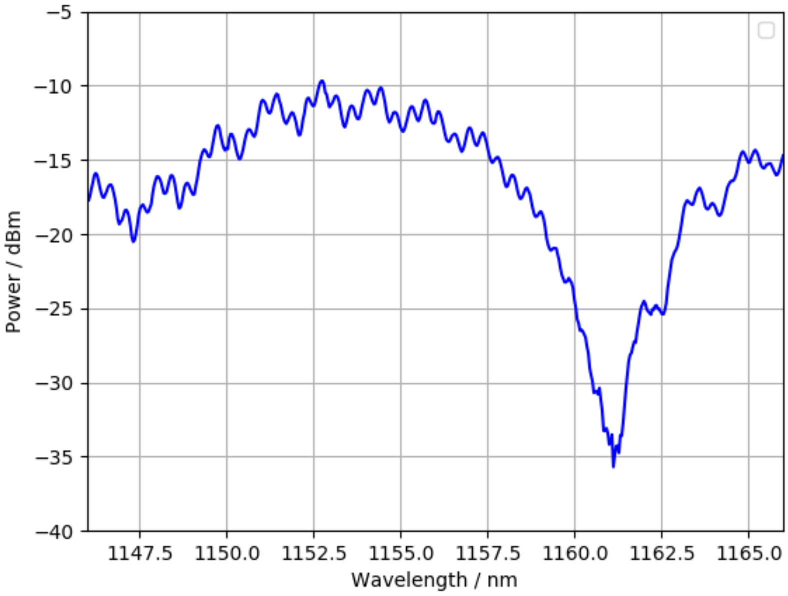

Figure 3.8: Comb power spectrum between 1146 nm and 1166 nm recorded using an OSA with resolution bandwidth RBW = 0.03 nm.

Beatnote signals' math

The beatnote signal of two laser sources can be described by considering the electric field associated to the two laser beams, E_1 and E_2

$$\begin{aligned} E_1(t) &= E_1 \cos(\omega_1 t - \phi_1), \\ E_2(t) &= E_2 \cos(\omega_2 t - \phi_2). \end{aligned} \tag{3.7}$$

The total optical power impinging the photodiode is:

$$\begin{aligned} P(t) \propto & \frac{E_1^2}{2}[1 + \cos(2\omega_1 t - 2\phi_1)] + \frac{E_2^2}{2}[1 + \cos(2\omega_2 t - 2\phi_2)] + \\ & + E_1 E_2[\cos((\omega_1 - \omega_2)t - (\phi_1 - \phi_2)) + \cos((\omega_1 + \omega_2)t - (\phi_1 + \phi_2))]. \end{aligned} \tag{3.8}$$

ω_1, ω_2 and $\omega_1 + \omega_2$ are too fast to be detected because of the limited bandwidth of the photodiode. Therefore one will have only access to the frequency difference between the two lasers, $\omega_1 - \omega_2$. As a consequence, the average optical power $P(t)$ on the detector is

$$P(t) \propto E_1^2 + E_2^2 + 2E_1 E_2 \cos((\omega_1 - \omega_2)t - (\phi_1 - \phi_2)), \tag{3.9}$$

which emphasises the fact that for optimising the SNR of the beatnote signal the best condition is achieved when the two laser have quite the same power levels.

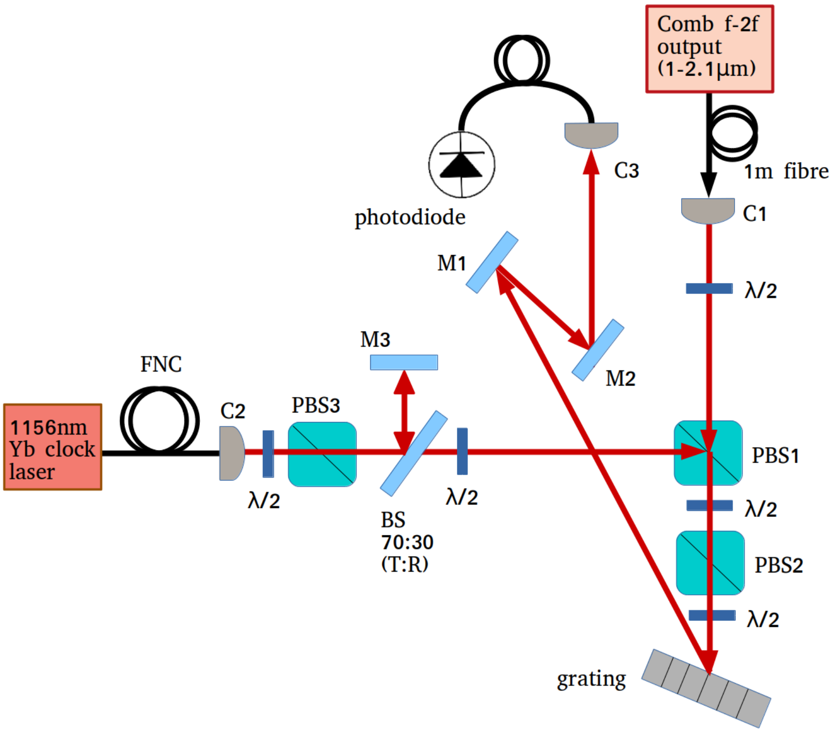

Figure 3.9: Optical setup for the 1156 nm laser beatnote detection. 1 m-long PM fibre brings the comb $f-2f$ output to the optical bench. This setup has been improved by eliminating the 1 m-fibre and coupling the $f-2f$ output directly to free-space. PBS: polarising beam splitter; BS: beam splitter; $\lambda/2$: half-waveplate; C: collimator; M: mirror; FNC: fibre-noise cancellation.

1156 nm detection

1 mW power from the 1156 nm laser is available for the beatnote measurement. On the other hand, the amount of comb power in the 1156 nm region can be evaluated by measuring the $f-2f$ spectrum using an optical spectrum analyser (OSA). Figure 3.8 shows the power spectrum in a 20 nm region around this wavelength with a 0.03 nm resolution bandwidth (RBW) when the pump laser currents of the $f-2f$ amplifier are optimised to have at the same time SNR > 30 dB on the f_0 beatnote and the maximum power in the region of interest. A comb power $P_{f-2f,1156}$ of about 56 µW can be achieved around 1156 nm in a 0.03 nm bandwidth. The number $n_{\Delta\nu}$ of comb teeth within the bandwidth $\Delta\nu$ is $n_{\Delta\nu} = \Delta\nu/f_{\text{rep}} \simeq 27$. The power-per-tooth can be estimated as $P_{f-2f,1156}/n_{\Delta\nu} \simeq 2$ µW.

The free-space interferometer used to detect the 1156 nm laser beatnote is shown in fig. 3.9. The 1156 nm light polarisation is set horizontal after collimator C2 by using a $\lambda/2$ waveplate and PBS3. Before combining the two radiations, the 1156 nm light is split by a 70:30 beam splitter. 30% is reflected for the fibre-link

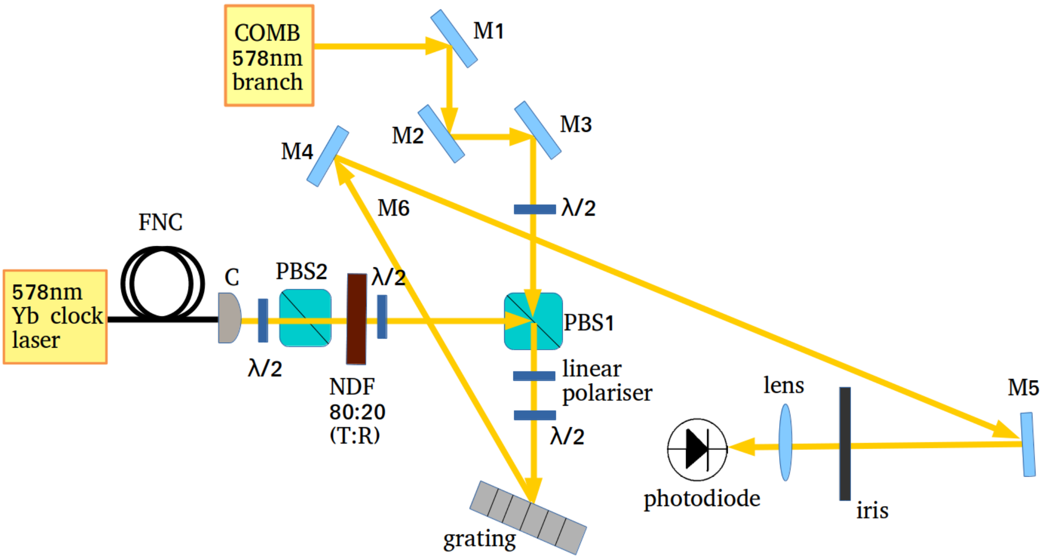

Figure 3.10: Optical setup for the 578 nm laser beatnote detection. PBS: polarising beam splitter; NDF: neutral density filter; $\lambda/2$: half-waveplate; C: collimator; M: mirror; FNC: fibre-noise cancellation.

phase-stabilisation, while 70% is used to perform the beatnote with the comb. The CW-laser and comb radiations are superposed by using a polarising beam splitter (PBS1). Then a reflective holographic grating disperses the comb light along a free-space distance of 110 cm before reaching a fibre-coupled fast InGaAs-photodiode. In this way only a small fraction of the $f-2f$ output is collected on the photodiode, preventing the detector from power saturation. The grating has 1200 grooves/nm and dispersion of 0.74 nm/mrad. After PBS1, a $\lambda/2$ waveplate is used together with PBS2 for combining the horizontal and vertical polarisations that exit from PBS1. The two waveplates placed before PBS1 allow optimisation of the power of each component used for the beatnote. Then the polarisation is optimised for achieving the maximum grating efficiency through a $\lambda/2$ waveplate. The resulting beatnote between the 1156 nm CW-laser and the comb reaches up to 38 dB SNR in a 100 kHz RBW.

578 nm detection

600 µW of the 578 nm second-harmonic radiation generated from the 1156 nm laser is beaten with the 578 nm comb output, which is 1.1 nm-wide and has an output power of about 5 mW. The power-per-tooth is about 1 µW.

The 578 nm beatnote with the comb is detected by using a free-space setup similar to the one implemented for the 1156 nm radiation. The optical setup is shown in figure 3.10. In this case an holographic grating, with 2400 grooves/nm

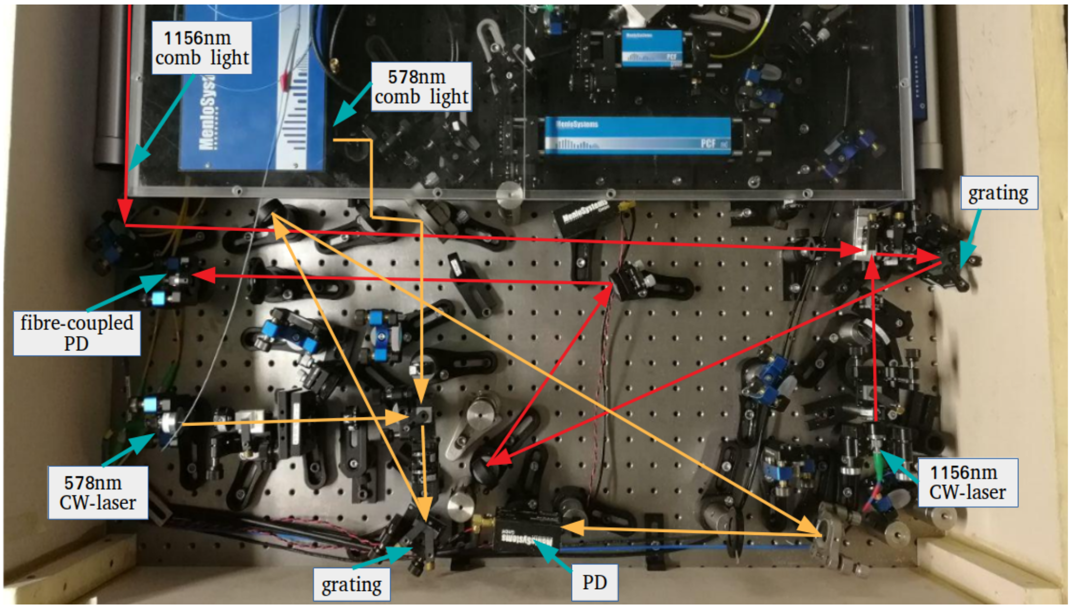

Figure 3.11: Picture of the free-space interferometers developed for measuring the 1156 nm and 578 nm betanotes. The optical paths are highlighted by the red and yellow arrows, respectively for the 1156 nm and 578 nm beatnotes' interferometers. PD: photodiode.

and dispersion of 0.33 nm/mrad, disperses the comb light along a 117 cm-long free-space path. The comb and 578 nm radiations are superposed using PBS1 and a linear polariser. The beatnote signal is detected through a free-space fast Si-photodiode. Before impinging the photodetector the two laser beams pass through an iris, used for cutting out the comb teeth whose wavelength is far from the CW-laser, and then they are focused by a 20 mm-focus lens. A neutral density filter with 79% of transmission is used for having a fraction of the 578 nm CW-laser back-reflected toward the Yb clock laboratory for the fibre-link phase-stabilisation. The resulting beatnote at 578 nm has SNR up to 35 dB in a 100 kHz RBW.

1542 nm detection

The beatnote between the 1542 nm slave laser and the 1.56 µm comb branch is realised through a fully fibre-coupled interferometer. The 100 nm-wide comb output is filtered on a 0.8 nm BW (100 GHz) using a standard telecom filter centred on channel 44th (centre λ = 1542.14 nm) of the International Telecommunication Union (ITU grid). After the filter, about 30 µW of comb light are combined with the CW-laser using a fibre coupler with a 90:10 split ratio. The comb light goes through the 90% arm of the coupler, while the 10%-arm is connected to the 1542 nm laser. This is due to the fact that we need to counter-balance the high-power output of the CW-laser with respect to the comb teeth power, in the same way as is achieved by using $\lambda/2$ waveplates for the free-space interferometers above described. All the fibres used are uncompensated and non-polarisation-maintaining. The beatnote signal easily achieves SNR of more than 40 dB in a 100 kHz RBW.

3.4 Multi-branch comb residual noise

Typically, optical combs' characterisation is performed by comparing optical frequency absolute measurements and optical frequency ratio measurements between two similar systems (i.e. by using two optical combs) [116, 135, 136]. However, in our setup we exploit the possibility of having the same CW-laser source available both at the fundamental frequency and its second-harmonic. These radiations can be measured on two different comb branches allowing the suppression of the CW-laser noise in the measurement, so that we can perform the characterisation using a single optical comb. The residual noise of our multi-branch comb structure is evaluated by measuring the frequency ratio between the 1156 nm laser and its 578 nm second-harmonic. They are detected on the $f - 2f$ and the 578 nm comb branches respectively, hence we can evaluate the residual noise between these two modules. In addition, we characterise also the residual noise between the $f - 2f$ and the 1.56 µm branches by beating the same 1542 nm laser to these two comb branches.

$f - 2f$ vs 578 nm branches

Being $\nu_{1156,\mathrm{comb}}$ and $\nu_{578,\mathrm{comb}}$ the absolute frequency values of the 1156 nm laser and its frequency-doubled component measured on the comb, we evaluated the frequency ratio $\nu_{578,\mathrm{comb}}/\nu_{1156,\mathrm{comb}}$ by measuring the two beatnote signals with the comb, $f_{\mathrm{b},1156}$ and $f_{\mathrm{b},578}$, together with the comb offset frequency f_0 (see section 3.1). We used a zero-dead time eight-channel K+K FXE frequency counter [137] referenced to the H-maser. The counter is used with a 1 s gate time and in the phase-averaging configuration (Λ-counting), which allows better performance evaluation for short averaging time [138–140]. The instability of the frequency counter has been characterised by sending the same 10 MHz maser signal as input frequency and reference for the counter. The ultimate counter fractional instability at 10 MHz is about 3×10^{-13} at 1 s of averaging time, decreasing as $1/\tau$. Hence it is negligible when converted from the RF to the optical domain, and optical frequency measurements are not limited up to the 2×10^{-20} level.

The general electronics scheme used for processing the beatonte signals is realised as showed in fig. 3.12. The beatnote signal is filtered with a 120 MHz low-pass filter (LPF). Considering that $f_{\mathrm{rep}} = 250$ MHz, then the maximum value of the beatnote between a laser and the nearest comb tooth is < 125 MHz, and it can be detected within the 3 dB-bandwidth of the LPF. The signal is down-converted and filtered, then measured on the K+K. The counter has an input frequency range

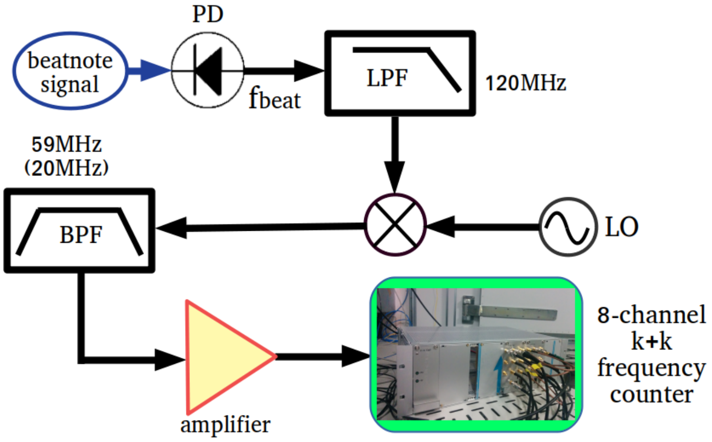

Figure 3.12: General electronic chain for the beatnote signals' processing. LO: local oscillator; LPF: low-pass filter; BPF: band-pass filter; PD: photodiode.

between 4 kHz and 65 MHz. Usually we use BPFs at 20 MHz or 59 MHz after the mixing stage, with a 3 dB-bandwidth of 3 MHz. Finally, the converted beatnote signal is amplified to reach a peak power between 4 dBm and 18 dBm (i.e. the power level needed to be properly counted) and it is sent to the counter. The LO used is referenced to the H-maser in order to improve its frequency stability and to not degrade the measurement.

Each beatnote signal is counted by two similar but independent electronics chains in order to detect cycle-slips occurrence [141]. Data are rejected from the measurements if the difference between the two is greater than 500 mHz.

Looking at fig. 3.5, it can be seen that the absolute frequencies $\nu_{1156,\mathrm{comb}}$ and $\nu_{578,\mathrm{comb}}$ are linked to the ^{171}Yb optical clock transition ν_{Yb} by the relations:

$$\begin{aligned} \nu_{1156,\mathrm{comb}} &= (\nu_{\mathrm{Yb}} - f_{\mathrm{AOM,atoms}})/2 + f_{\mathrm{AOM,comb\text{-}1156}} \\ \nu_{578,\mathrm{comb}} &= \nu_{\mathrm{Yb}} - f_{\mathrm{AOM,atoms}} + f_{\mathrm{AOM,comb\text{-}578}}. \end{aligned} \tag{3.10}$$

Therefore, by considering that $f_{\mathrm{AOM,comb\text{-}1156}} = f_{\mathrm{AOM,comb\text{-}578}} = 80$ MHz, $\nu_{1156,\mathrm{comb}}$ and $\nu_{578,\mathrm{comb}}$ are linked by:

$$\nu_{1156,\mathrm{comb}} = \nu_{578,\mathrm{comb}}/2 - f_{\mathrm{AOM,comb\text{-}578}}/2 + f_{\mathrm{AOM,comb\text{-}1156}} = \nu_{578,\mathrm{comb}}/2 + 40\ \mathrm{MHz}. \tag{3.11}$$

The absolute frequencies $\nu_{1156,\mathrm{comb}}$ and $\nu_{578,\mathrm{comb}}$ are expressed in terms of the comb parameters by:

$$\begin{aligned} \nu_{1156,\mathrm{comb}} &= m_{1156} f_{\mathrm{rep}} + f_0 + f_{\mathrm{b},1156} \\ \nu_{578,\mathrm{comb}} &= m_{578} f_{\mathrm{rep}} + 2f_0 + f_{\mathrm{b},578}, \end{aligned} \tag{3.12}$$

Note that for the $\nu_{578,\mathrm{comb}}$ expression the carrier-envelope offset is $2f_0$, as in this case the comb branch used for the beatnote detection is obtained through a frequency-doubling stage.

The comb mode numbers m_{1156} and m_{578} are calculated from eq. (3.10) and eq. (3.12) once the signs of f_0 and the two beatnotes are determined, since in this case the absolute frequency ν_{Yb} is known a priori with an absolute accuracy at the Hz level. The procedure for establishing the proper signs is described in details in section 4.1. The mode number values are $m_{1156} = 1\,036\,592$ and $m_{578} = 2\,073\,184$. Hence for these measurements holds the relation $m_{578} = 2m_{1156}$, which cannot be assessed a priori since it depends on the frequency shifts due to the AOMs along the 1156 nm and 578 nm optical paths.

The frequency ratio $\nu_{578,comb}/\nu_{1156,comb}$ is calculated via software by using eq. (3.5). Therefore, we calculate for each element of the dataset the two frequencies ν_{A} and ν_{B}^* for obtaining the virtual beatnote ν_{T}:

$$\nu_{\mathrm{T}} = \nu_{\mathrm{A}} - \nu_{\mathrm{B}}^* = (f_{\mathrm{b},1156} + f_0) - \frac{m_{1156}}{m_{578}}(f_{\mathrm{b},578} + f_0) = \nu_{1156,\mathrm{comb}} - \frac{m_{1156}}{m_{578}}\nu_{578,\mathrm{comb}}. \quad (3.13)$$

The software processing uses special digital number format. Commonly float numbers are given with 16 digits of precision, which does not guarantee the accuracy level required for our measurements. Hence we chose the "Decimal" Python class [142] to process the data, which enables to specify the number of decimal digits and reach 18-digit precision or even greater.

Finally, the frequency ratio is expressed in terms of ν_{T} and the comb mode numbers by:

$$\frac{\nu_{578,\mathrm{comb}}}{\nu_{1156,\mathrm{comb}}} = \frac{m_{578}}{m_{1156}}\left(1 - \frac{\nu_{\mathrm{T}}}{\nu_{1156,\mathrm{comb}}}\right). \quad (3.14)$$

Note that this measurement can be alternatively performed by calculating the difference between the two absolute frequencies ν_{1156} and ν_{578}, which leads to the same result.

The multi-branch comb performances are assessed by considering the quantity $r/r_0 - 1$, where r is the experimental frequency ratio $\nu_{578,\mathrm{comb}}/\nu_{1156,\mathrm{comb}}$ measured through the comb and r_0 is the theoretical frequency ratio calculated from the absolute frequency values given by eq. (3.10). Figure 3.13 shows the residual instability of the measurement in terms of overlapping Allan deviation. The three curves refer to slightly different optical setups for the 1156 nm beatnote detection. The green curve shows the instability obtained when a 1 m uncompensated fibre was used for bringing the $f-2f$-branch light to the beatnote detection setup. The measurement has an instability plateau at the 2×10^{-17} level for $0\ \mathrm{s} < \tau < 10\ \mathrm{s}$, which increases for longer averaging time. In order to investigate possible causes of this behaviour, we performed another measurement (blue curve) using a foam rubber to cover the 1 m uncompensated fibre. As can be seen the result was better than the previous measurement, leading to a instability of 2×10^{-18} at 10 000 s. However, both measurements show a 6×10^{-18} flicker instability at 100 s. After these measurements, we replaced the 1 m fibre on the $f-2f$ output with a free-space path. The result of the measurement with the new setup is shown by the yellow curve of fig. 3.13.

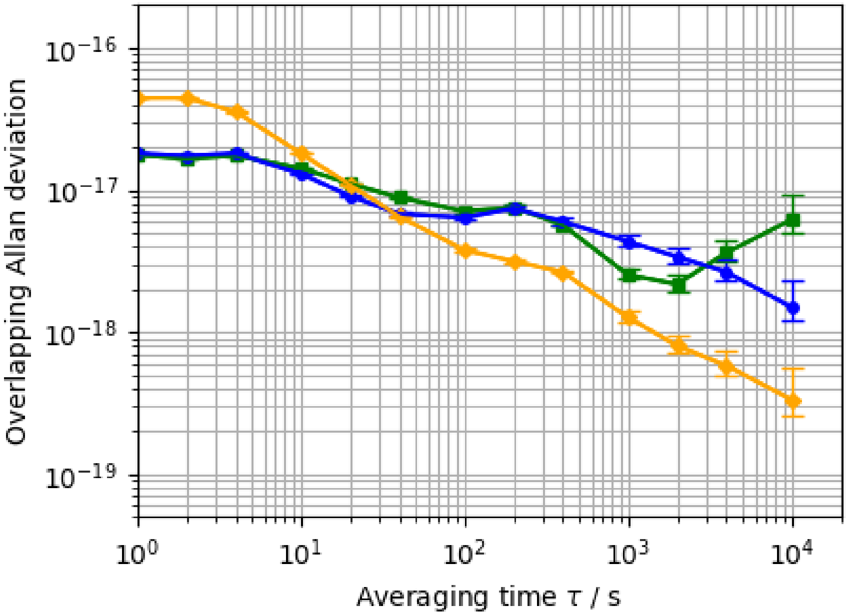

Figure 3.13: Fractional frequency instability of the frequency ratio measurement ν_{578}/ν_{1156} in terms of overlapping Allan deviation. Green: with 1 m uncompensated fibre that brings the $f-2f$ comb output to the optical bench.; blue: the 1 m fibre was covered with a foam rubber; yellow: the 1 m fibre was eliminated and the $f-2f$ output was directly coupled to free-space.

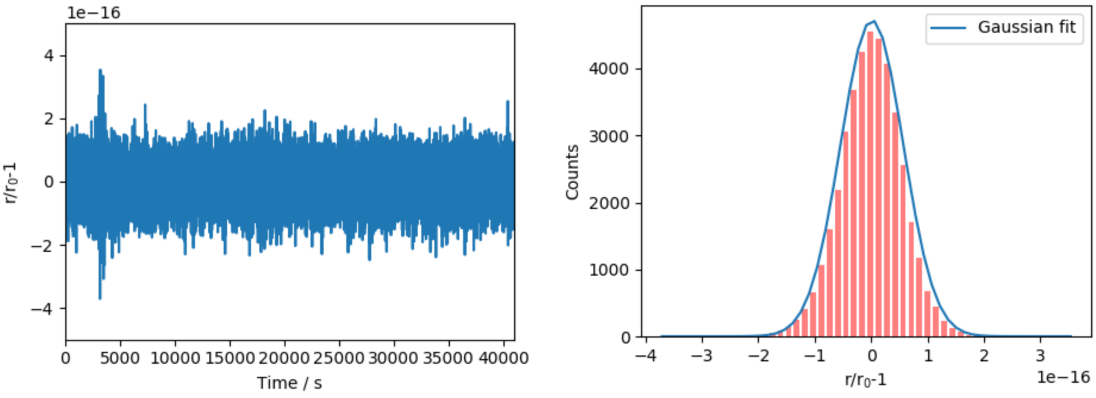

(a) **(b)**

Figure 3.14: Raw data of the frequency ratio measurement scaled to the zero offset value. (a) Raw data of r/r_0-1 over the measurement time. (b) Dispersion of the r/r_0-1 data around the zero-offset value. Blue: Gaussian fit of the distribution.

For $\tau > 10$ s the instability follows a $\tau^{-1/2}$ slope associated to white freq noise, reaching an ultimate level of 3×10^{-19} at 10 000 s.

However, the 5×10^{-17} instability at 1 s of the yellow curve is worse than the other measurements and its causes are not yet completely understood. Some investigations have been done, such as varying the polarization of the $f - 2f$ output by adding a $\lambda/2$ waveplate, as well as changing the SNR of the 1156 nm beatnote from 38 dB to 30 dB in a 100 kHz RBW, i.e. the maximum value we can reach and a lower value that still allows proper counting on the K+K counter. No deviation from the 5×10^{-17} instability at 1 s have been observed from these measurements.

Considering the measurement accuracy, we calculated the average value of the data $r/r_0 - 1$ and give the statistical uncertainty by using the last point of the Allan deviation. The resulting value is $(-1.7 \pm 3) \times 10^{-19}$, which means that the there is no offset with respect to zero at the level of 3×10^{-19}. Figure 3.14 shows the raw data of the quantity $r/r_0 - 1$ and their distribution around zero. The data follow a normal distribution, as confirmed by the Gaussian fit reported in the figure. Furthermore, in addition to the multi-branch residual noise assessment, the ratio measurement result enables us to quantify a 3×10^{-19} upper limit to the frequency instability provided by the frequency-doubling process of the crystal used for generating the 578 nm radiation.

$f - 2f$ vs 1.56 µm branches

The characterisation of the inter-branch noise between the $f - 2f$ and the 1.56 µm branches has been done by measuring it simultaneously on the two branches (see section 3.3.1). As for the detection on the 1.56 µm-branch, the beatnote between the laser and the $f - 2f$-branch is obtained by a fully fibre-coupled interferometer, where the $f - 2f$ output is filtered on the 44-channel of the ITU grid before being sent to a 50:50 fibre coupler together with the CW-laser. All the uncommon fibre paths of the interferometer have been kept as short as possible to reduce the impact of possible temperature gradients that could affect the optical path length in a different way and degrade the instability.

Note that in this case one can obtain the same instability result as the frequency ratio by simply subtracting the two beatnote signals. The mode number of the comb tooth with which the laser is beaten is identical for the two branches, as they measured the same laser frequency without any additional frequency shifting. The corresponding Allan deviation is shown in fig. 3.15. It starts with a flicker instability of 1×10^{-17} at 1 s and then decreases as $(\tau/\mathrm{s})^{-1/2}$ for $\tau > 10$ s.

Around the 1542 nm region the $f - 2f$-branch does not provide as much power as the 1.56 µm-branch. Measurements were performed with f_0 unlocked, allowing the maximisation of the $f - 2f$ power in the 1542 nm region, even if this configuration led to strong degradation in the f_0 SNR at detection. As a result, the beatnote between the CW-laser and the $f - 2f$-branch could reach the adequate level of SNR

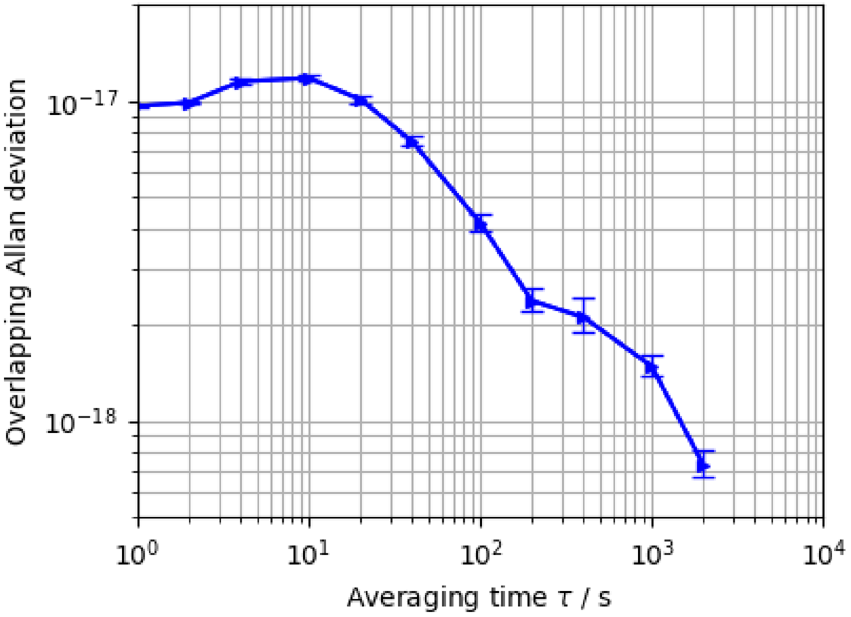

Figure 3.15: Fractional frequency instability of the $f - 2f$ - 1.56 µm branches' comparison in terms of overlapping Allan deviation.

to be counted (usually the minimum required value is 30 dB in a 100 kHz RBW). However, since the maximum achievable SNR was just few dB above the threshold level then we had to periodically compensate for the polarisation-changes along the fibres with a fibre-polarisation controller.

3.5 Transfer oscillator electronics

The electronic setup for detecting the virtual beatnote ν_{T} between the 1156 nm master laser and the 1542 nm slave laser is shown in fig. 3.16. The setup is described specifically for these two laser wavelengths. However, it has been designed to be flexible and reconfigurable for any pair of master and slave lasers by making few adjustments. Components that are to be adjusted are all the LOs frequencies and the BPFs used after the DDS outputs, which are shown in red.

The electronic scheme is built up as follows. First, the two laser beatnotes are mixed with LO_1 and LO_2 to reach a frequency value that can be filtered with a BPF. Then with a second mixing stage we produce the f_0-free signals $\bar{f}_{\mathrm{b},1156} = \mathrm{LO}_1 + f_{\mathrm{b},1156} + f_0$ and $\bar{f}_{\mathrm{b},1542} = \mathrm{LO}_2 + f_{\mathrm{b},1542} + f_0$. Note that the offset frequency f_0 has to be summed with the correct sign in order to get rid of its contribution in the generation of ν_{A} and ν_{B}. In our measurements f_0 has negative sign, while both $f_{\mathrm{b},1156}$ and $f_{\mathrm{b},1542}$ have positive sign. $\bar{f}_{\mathrm{b},1156}$ is sent to DDS_1 and scaled by the factor

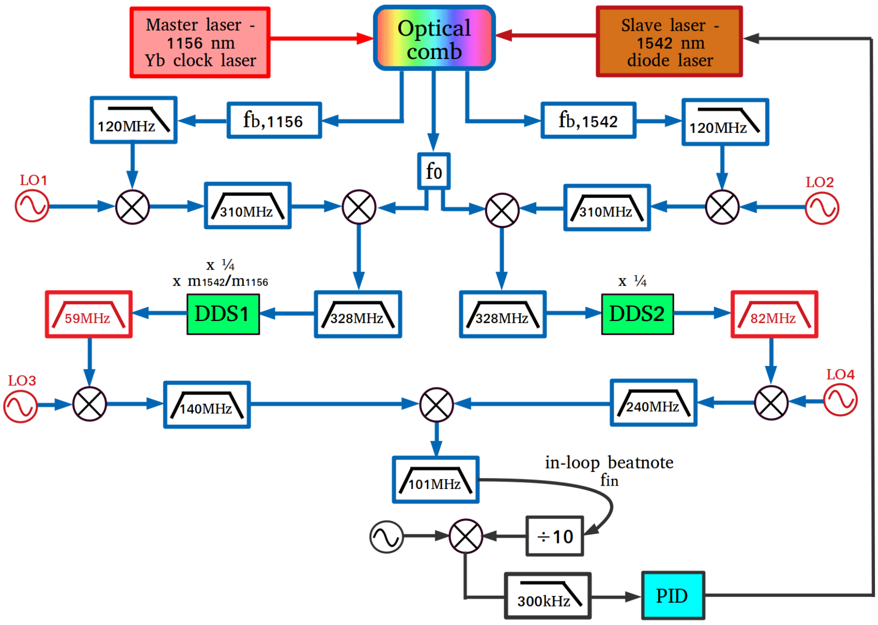

Figure 3.16: Electronics used for implementing the transfer oscillator technique. LO: local oscillator; DDS: direct digital synthesiser; PID: proportional-integral-derivative controller.

$1/4 \times m_{1542}/m_{1156}$. Being $m_{1542} = 777\,600$ and $m_{1156} = 1\,036\,592$, the resulting scaling factor $m_{1542}/m_{1156} = 0.750\,150\,493\,154\,490\,870\,08$ cannot be directly applied because of the Nyquist constraint on the DDS output. Therefore an additional factor 1/4 has been chosen in order to guarantee the DDS operation far enough from the Nyquist limit. For this reason we also apply the same 1/4 factor to $\bar{f}_{\mathrm{b},1542}$ by using DDS$_2$. However, for scaling $\bar{f}_{\mathrm{b},1542}$ the DDS is not strictly required and the 1/4 factor can be applied as well by using a pre-scaler. The DDS outputs are then filtered and up-converted by mixing with LO$_3$ and LO$_4$. The resulting signals are finally mixed together to generate the virtual beatnote ν_{T} at a fixed value of 100 MHz. This virtual beatnote f_{in} is used to feed a PLL that acts on the 1542 nm slave laser.

Direct digital synthesisers

DDSs allow the generation of a frequency-tunable output signal using an arbitrary input signal as a reference clock. Practically, the reference clock frequency is divided by the scaling factor set by a programmable binary tuning word. The DDSs used in our experiment are Analog Devices AD9912, which feature a 14-bit digital-to-analog converter and 4 µHz resolution. The formula that links the DDS output f_{OUT} to the input clock signal f_{CLK} is

$$f_{\mathrm{OUT}} = \frac{M f_{\mathrm{CLK}}}{2^N}, \tag{3.15}$$

where M is the binary tuning word and N is the length in bits of the tuning word. For the AD9912 the tuning word has $N = 48$. The reference clock frequency range is between 250 MHz and 1000 MHz.

For choosing the DDS for our experiment we considered the required level of accuracy that has to be preserved in the multiplication stage. Our target is to perform spectral purity transfer of the best ultrastable lasers available today, which can reach fractional stability level of 10^{-17} at 1 s for 1.5 µm sources (200 THz). Therefore, we have an absolute uncertainty at the mHz level that is reflected in the f_0-free signals we detect and use as clock signals for the DDSs. Such signals range in the radio-frequencies domain, up to hundreds of MHz, and consequently the DDS outputs range from tens to hundreds of MHz. Having 4 µHz resolution, the AD9912 produces such kind of signals guaranteeing the mHz-level accuracy we want to transfer between the master and slave lasers.

We investigated the occurrence of cycle-slips when using the DDSs. By sending the same f_0-free signal to two DDSs and changing the SNR of either f_0 or the beatnote between the comb and the lasers we observed that the DDS output is immune from cycle-slips if the SNR of both f_0 and the beatnotes is higher than 33 dB in a 100 kHz RBW.

The AD9912 DDS was already used in other high-accuracy frequency ratio and spectral purity transfer measurements and its accuracy has been tested up to the 10^{-21} level [29, 125].

Feedback loop

The 1542 nm slave laser is phase-locked to the master laser by using the virtual beatnote f_{in} for generating an error signal that feeds a proportional-integrative (PI) controller. The virtual beatnote contains the fluctuations of an optical signal, which are 10^6 times greater than an RF-signal. As can be seen from fig. 3.16 a 10× frequency divider is used to slow down the phase changes of f_{in}. After that, the divided signal is down-converted to DC by mixing with a local oscillator at 10 MHz. In this way the error signal is generated, filtered with a 300 kHz LPF and sent to the PI controller. Two control signal outputs are then generated. The first one provides a fast control signal that drives a 40 MHz AOM on a 60 kHz control bandwidth. The second one is a slow correction signal that acts on the slave laser current.

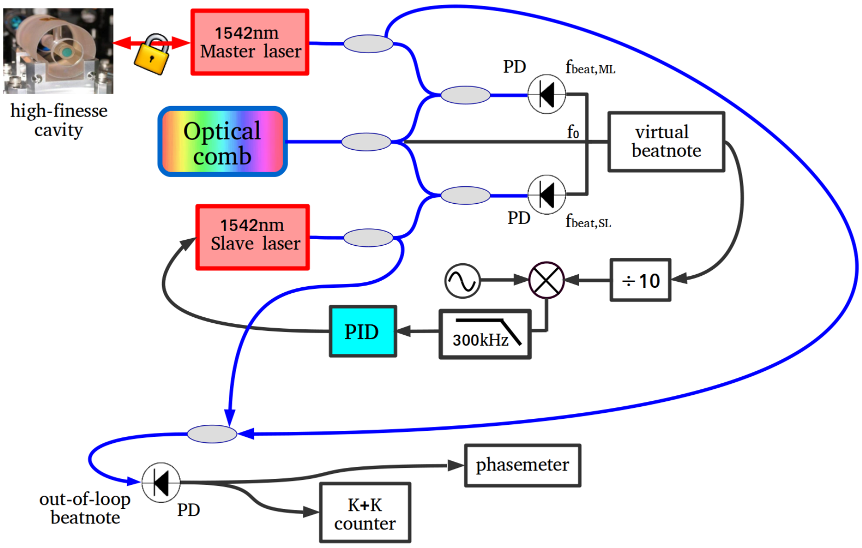

Figure 3.17: Experimental setup used to test the transfer oscillator electronics. PD: photodiode; PID: proportional-integral-derivative controller.

3.6 Electronic setup test: phase-locking of two 1542 nm lasers

We tested the noise contribution of the transfer oscillator electronics by phase-locking two 1542 nm-lasers using the transfer oscillator setup instead of locking them directly to each other using the beatnote between the two. This gives the opportunity of performing the spectral transfer in the simplest configuration. Indeed, since the two laser frequencies can be tuned in order that they differ by a quantity lesser than the comb repetition rate, we can beat the two lasers with the same comb mode. In this way f_{rep} does not contribute to the measurement and there is no need of scaling between separated spectral regions of the optical domain. Therefore, the differences with respect to using the direct beatnote of the two sources are the addition of the electronic chain (which will be the same for a general spectral purity transfer scheme), including the capability of subtracting the offset frequency contribution via hardware.

For this measurement we use the aforementioned external-cavity diode laser (section 3.3) and a 1542 nm cavity-stabilised laser with 5×10^{-15} fractional stability at 1 s as the master. The measurement setup is shown in fig. 3.17. The lasers are sent to two 50:50 fibre splitters. One half of the power is used for the detection of the two beatnote signals with the 1.56 µm comb output and the virtual beatnote is generated with the electronics described in section 3.5. The other branch is used to detect the direct beatnote signal between the two lasers. This signal allows an out-of-loop characterisation of the system and it is measured simultaneously with

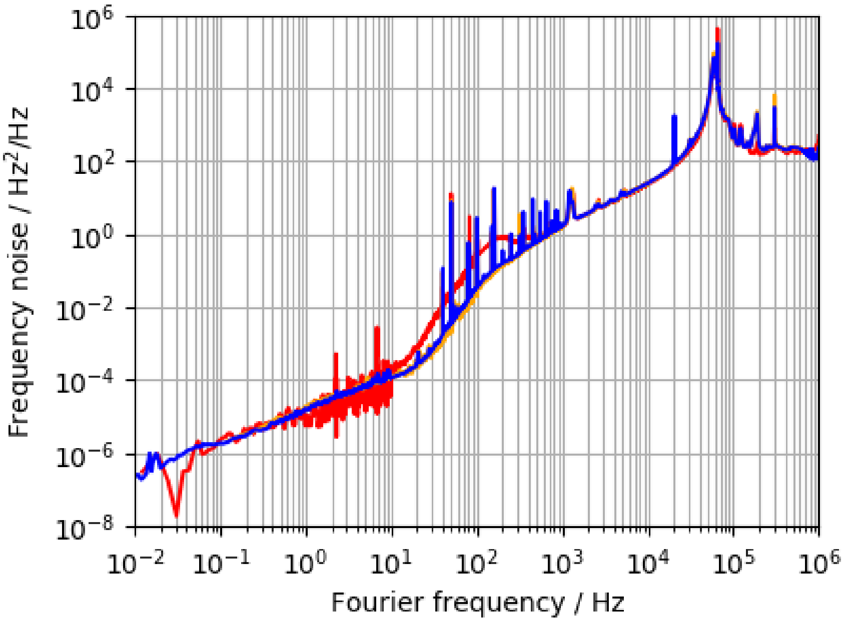

Figure 3.18: Frequency noise measurement of the transfer oscillator electronics by phase-locking two 1542 nm lasers. Red: the two lasers are directly phase-locked; yellow: the two lasers are phase-locked by using the comb but without the DDSs in the transfer electronics; blue: the two lasers are phase-locked using the comb and inserting the DDSs in the transfer electronics.

a digital phasemeter (1 MHz BW) and the K+K counter (1 s of gate time).

As a first step we phase-locked the two lasers by using the direct beatnote between the two. A copy of the direct beatnote is taken outside of the feedback loop and used as the out-of-loop signal for the phase-noise measurement. This sets the measurement noise floor.

Then we locked the two lasers using the comb as a transfer oscillator. In this case, a DDS is not needed, as the comb teeth are equal. After that, we tested the complete electronic chain including also the DDSs. In the latter case the two DDSs are used to perform the division of the f_0-free signals by a common arbitrary factor.

Figure 3.18 summarises the results in terms of frequency-noise of the out-of-loop beatnote. The red curve refers to the phase-locking of the two lasers using their direct beatnote, while the yellow and blue curves correspond to the phase-locking performed using the transfer oscillator technique, the first without using the DDSs, the latter with the complete electronic scheme. The three spectra overlap over almost all the Fourier frequency range of the measurement, except for the region between 10 and 500 Hz where the noise excess of the red curve is due to different value of the PLL gain. Hence we can conclude that no additional noise is introduced

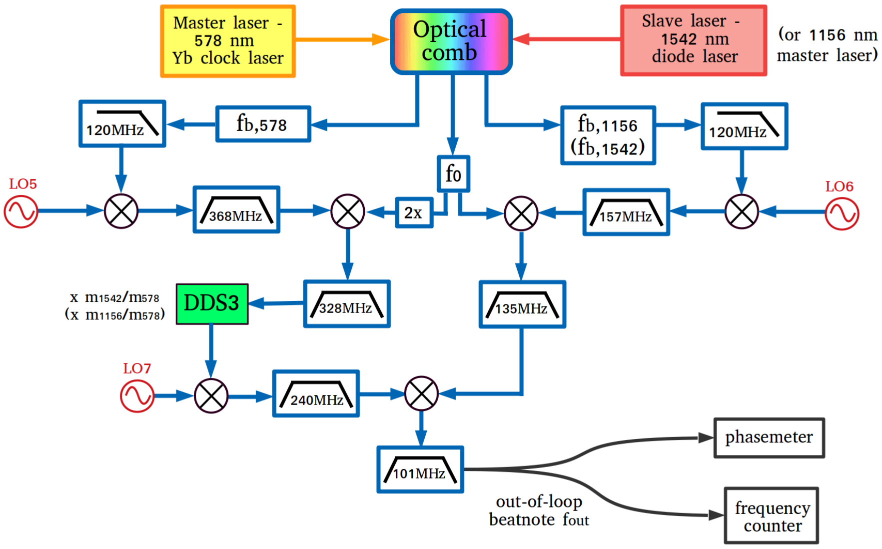

Figure 3.19: Seond transfer electronic chain, developed for detecting the out-of-loop beatnote between the master laser light at 578 nm and the 1542 nm slave laser. LO: local oscillator; DDS: direct digital synthesiser.

by the electronic setup.

3.7 Spectral purity transfer of the 1156 nm ^{171}Yb clock laser

Taking into account the previous characterisation of the contributions of the inter-branch comb noise and the transfer oscillator electronics, hereby the spectral purity transfer of the 1156 nm ^{171}Yb clock laser to the 1542 nm laser is discussed.

In order to characterise the spectral transfer, we detect an out-of-loop beatnote f_{out} by developing a second transfer oscillator setup for generating the virtual beatnote between the same 1542 nm slave laser and the 578 nm second-harmonic of the master laser. As can be seen from fig. 3.19, the new setup is similar to the previous one, with only few differences. Firstly, f_0 is multiplied by a factor 2 (represented by the "2×"box) before being mixed to $f_{\mathrm{b},578}$, since in this case we detect the master laser beatnote with a comb branch generated by a frequency-doubling process. Moreover, a single DDS is used for this measurement. This is due to the fact that, being $m_{1542} = 777\,600$ and $m_{578} = 2\,073\,184$, the comb mode number ratio $m_{1542}/m_{578} = 0.375\,075\,246\,577\,245\,435\,04$ is directly feasible using DDS3.

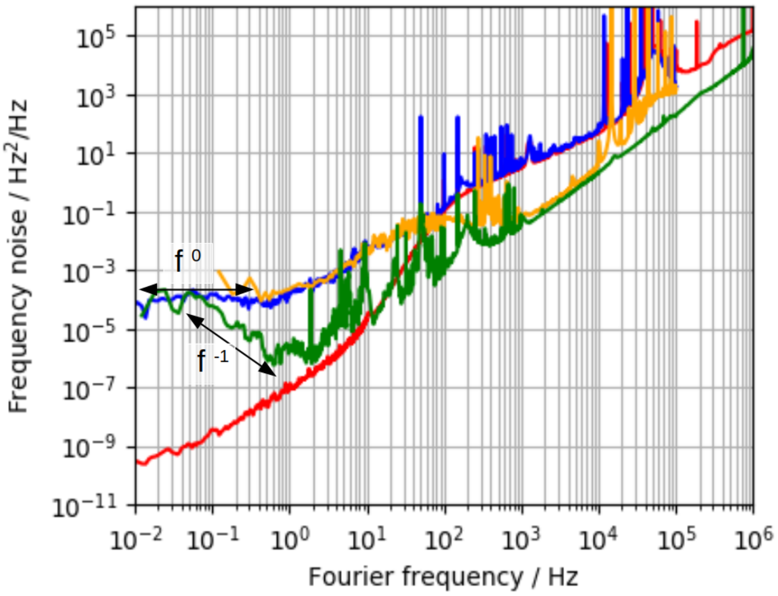

Figure 3.20: Spectral purity transfer evaluated through frequency noise spectra reported in the 1542 nm spectral region. Blue: out-of-loop beatnote measured through the transfer electronics of fig. 3.19; yellow: residual noise between the $f-2f$ and the 578 nm branches evaluated through the frequency ratio ν_{578}/ν_{1156}; green: residual noise between the $f-2f$ and 1.56 µm branches; red: in-loop beatnote measured through the transfer electronics of fig. 3.16.

Results

The results of the spectral purity transfer are shown in fig. 3.20 and fig. 3.21 in terms of frequency noise and instability measurements. By combining these two measurement methods we can provide a complete picture of the system behaviour, concerning investigation of noise processes at Fourier frequencies as high as 10^6 Hz and long-term stability performances up to 10^4 s. The spectra of fig. 3.20 are scaled to the 1542 nm spectral region.

The frequency noise spectra of fig. 3.20 present the comparison between the noise of the out-of-loop beatnote (blue curve) and the in-loop beatnote (red curve). In addition, to better distinguish the contribution of different terms to the spectral transfer, we also show the frequency noise between the $f-2f$ and the 578 nm branches and between the $f-2f$ and 1.56 µm branches, which were described in section 3.4.

The noise between the $f-2f$ and 578 nm branches has been measured by using the electronics of fig. 3.19 for detecting the virtual beatnote between the 1156 nm laser and its 578 nm second-harmonic (refer to the values in brackets in fig. 3.19). This measurement is complementary to the frequency ratio evaluation described in

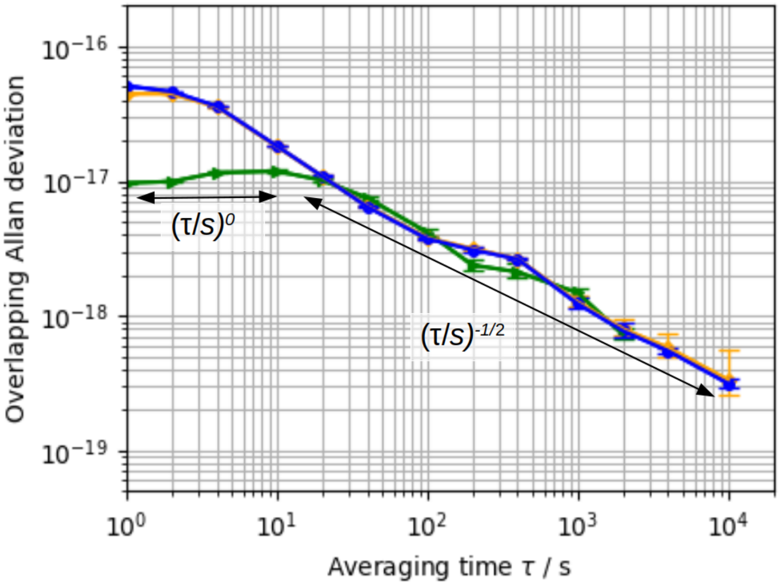

Figure 3.21: Spectral purity transfer evaluated through instability measurement in terms of overlapping Allan deviation. Blue: out-of-loop beatnote measured through the transfer electronics of fig. 3.19; yellow: residual instability between the $f-2f$ and the 578 nm branches evaluated through the frequency ratio ν_{578}/ν_{1156}; green: residual instability between the $f-2f$ and 1.56 µm branches.

section 3.4, which was computed via software.

The phase-noise between the $f-2f$ and the 1.56 µm branches has been obtained by electronically mixing the beatnotes between the 1542 nm and the two comb branches (see section 3.4) and measuring the resulting signal with the digital phasemeter. This characterisation quantifies the noise of the simplest dual-branch configuration together with the uncommon fibre paths. In particular, here we use the $f-2f$-branch, which is composed of an EDFA and a HNLF, while the 1.56 µm-branch is the main comb output without any additional components.

The blue curve includes both the electronic noise of the feedback loop and the multi-branch contribution given by the $f-2f$ and the 578 nm branches. In this case the 1.56 µm branch does not contribute, since it is in common-mode between the $f_{\text{b,in-loop}}$ and $f_{\text{b,out-of-loop}}$ detection schemes. However, the inter-branch noise power spectral density between the $f-2f$ and 1.56 µm branches (green curve) is lower than the blue curve. Thus the blue curve provides the upper limit to the spectral transfer. At high Fourier frequencies, above 100 Hz, the measurement is limited by the in-band PLL noise, and this is confirmed by the fact that the $f_{\text{b,out-of-loop}}$ overlaps the $f_{\text{b,in-loop}}$ noise (blue and red curves respectively). The noise bump at 60 kHz represents the PLL's locking bandwidth, which is limited by the AOM used in the feedback loop. Further improvement of the high-frequency noise can be achieved with a higher feedback loop bandwidth or by using slave lasers with lower noise. For Fourier frequencies below 100 Hz the major contribution is given by the inter-branch noise. Particularly, the measurements in which the 578 nm-branch is involved has a higher noise and set the limitation on the spectral transfer performance between 0.1 Hz and 100 Hz. On the other hand, the green spectrum represents the lower limit below 100 Hz. This can be seen also by looking at the frequency instability from 1 s to 10 s of the yellow and green curves in fig. 3.21.

In terms of fraction frequency instability the spectral transfer shows a $5 \times 10^{-17}(\tau/\mathrm{s})^{-1/2}$ level at 1 s, reaching the 3×10^{-19} region at 10 000 s ($f_{\text{b,out-of-loop}}$ Allan deviation, blue curve of fig. 3.21). The $f_{\text{b,out-of-loop}}$ Allan deviation and the virtual beatnote between the $f-2f$ and the 578 nm branches (yellow Allan deviation) overlap over the whole duration of the measurement. This confirms that the multi-branch comb noise sets the limitation on the long-term behaviour. As can be seen, all the curves of fig. 3.21 shows a deviation from white frequency noise at 400 s of averaging time, which is related to the air conditioning of the laboratory. Hence this emphasises the fact that the measurement is still sensitive to the environmental changes that act on the uncommon components of our system.

The frequency noise spectra and the instability measurements can be linked by considering the formula that describe the different noise processes in fig. 3.20. The dominant processes at Fourier frequencies below 1 Hz are white and flicker frequency noises, while for higher frequencies flicker phase noise and white phase noise emerge, whose behaviour is proportional to f^1 and f^2 respectively.

The frequency noise of the blue, yellow and green curve (referred as $S_{\nu-\text{out-of-loop}}$, $S_{\nu-\text{f-2f,578 nm}}$ and $S_{\nu-\text{f-2f,1.56 µm}}$) can be modelled as

$$\begin{aligned}
S_{\nu-\text{out-of-loop}} &= (1.5\times10^{-4}f^0 + 1.5\times10^{-3}f^1)\frac{\mathrm{Hz}^2}{\mathrm{Hz}},\\
S_{\nu-\text{f-2f,578 nm}} &= (1.5\times10^{-4}f^0 + 1.5\times10^{-3}f^1 + 5\times10^{-8}f^2)\frac{\mathrm{Hz}^2}{\mathrm{Hz}},\\
S_{\nu-\text{f-2f,1.56 µm}} &= (5\times10^{-6}f^{-1} + 2\times10^{-6}f^0 + 2\times10^{-8}f^2)\frac{\mathrm{Hz}^2}{\mathrm{Hz}}.
\end{aligned} \tag{3.16}$$

The flicker frequency noise $S_{\nu,\text{flickerFM}}(\mathrm{f})$, white frequency noise $S_{\nu,\text{whiteFM}}(\mathrm{f})$, flicker phase noise $S_{\nu,\text{flickerPM}}(\mathrm{f})$ and white phase noise $S_{\nu,\text{whitePM}}(\mathrm{f})$ are expressed as:

$$\begin{aligned}
S_{\nu,\text{flickerFM}}(\mathrm{f}) &= \nu_0^2\mathrm{h}_{-1}f^{-1},\\
S_{\nu,\text{whiteFM}}(\mathrm{f}) &= \nu_0^2\mathrm{h}_0f^0,\\
S_{\nu,\text{flickerPM}}(\mathrm{f}) &= \nu_0^2\mathrm{h}_1f^1,\\
S_{\nu,\text{whitePM}}(\mathrm{f}) &= \nu_0^2\mathrm{h}_2f^2,
\end{aligned} \tag{3.17}$$

where ν_0 is the carrier frequency and $\mathrm{h_i}$ are the coefficients of the power-law function that describes the power spectral density (PSD) [143]. The corresponding Allan variance $\sigma_{\mathrm{y}}^2(\tau)$ for each type of noise is [143]:

$$\begin{aligned}
&\text{flicker FM} \rightarrow \sigma_{\mathrm{y}}^2(\tau) = 2\ln(2)\mathrm{h}_{-1},\\
&\text{white FM} \rightarrow \sigma_{\mathrm{y}}^2(\tau) = \frac{1}{2}\frac{\mathrm{h}_0}{\tau},\\
&\text{flicker PM} \rightarrow \sigma_{\mathrm{y}}^2(\tau) = \frac{3\gamma - \ln(2) + \ln(2\pi f_{\mathrm{H}}\tau)}{4\pi^2}\frac{\mathrm{h}_1}{\tau^2},\\
&\text{white PM} \rightarrow \sigma_{\mathrm{y}}^2(\tau) = \frac{3f_{\mathrm{H}}}{4\pi^2}\frac{\mathrm{h}_2}{\tau^2},
\end{aligned} \tag{3.18}$$

where f_{H} is the measurement cut-off frequency.

Therefore, by extrapolating the coefficients $\mathrm{h_i}$ from eq. (3.16) it is possible to infer the expected behaviour of the Allan deviation for the corresponding curves of fig. 3.21. These calculations are consistent with the fractional instability values given by the frequency counter measurements performed with an equivalent bandwidth of 0.5 Hz. In particular, the Allan deviation at 1 s of averaging time calculated from the sum of each noise contribute as outlined in eq. (3.16) give $\sigma_{\mathrm{y}}(\tau = 1\ \mathrm{s}) = 4.9\times10^{-17}$ for the yellow and blue curves and $\sigma_{\mathrm{y}}(\tau = 1\ \mathrm{s}) = 1.5\times10^{-17}$ for the green curve, in agreement with the measured values of fig. 3.21.

Summary

We demonstrated that our multi-branch Er:fibre comb can sustain spectral purity transfer with a residual instability of $5\times10^{-17}(\tau/\mathrm{s})^{-1/2}$ and accuracy of 3×10^{-19} after 10 000 second of averaging time. The measurement limitation is determined by the uncorrelated noise between the comb branches, which has been characterised by using a single comb. The inter-branch noise contribution has been investigated by simultaneously measuring ultrastable lasers on different comb branches. This characterisation shows that our comb can be used for realising the spectral transfer of our ultrastable laser at 1156 nm, namely to the 1542 nm laser used for frequency dissemination over fibre links and to the clock laser of the INRiM ^{87}Sr optical clock [113] at 1398 nm, which in this way will be realised without using a dedicated ultrastable cavity. Although the single-branch stability level surpasses the multi-branch performance [93, 94], still the system we investigated does not hinder the spectral transfer of most of the ultrastable laser sources demonstrated so far [97, 103], as can be seen from the stability performance comparison of fig. 3.22. In addition, a multi-branch comb provides the advantage of easily detection of high-SNR beatnotes since different optical regions can be reached and independently optimised by acting on the branch-dedicated amplifiers.

The characterisation of the $f - 2f$ interferometer with respect to the 578 nm-branch and the 1.56 µm-branch can be generalised for Er:fibre multi-branch systems, as long as the wavelength-conversion components are of the same type. A possible

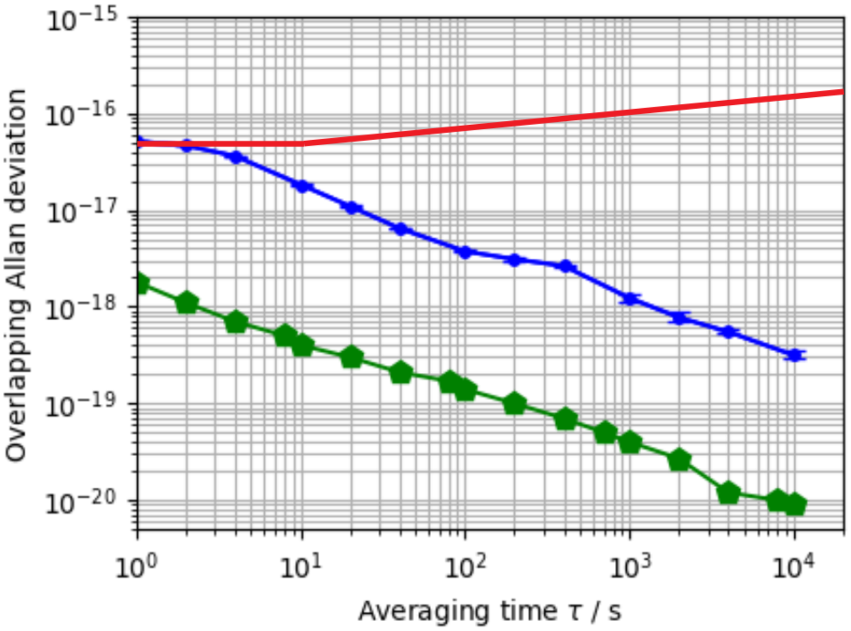

Figure 3.22: Stability comparison between our multi-branch comb measurement (blue Allan deviation) [111], the best ultrastable cavity demonstrated so far (red Allan deviation) [97], and single-branch comb performances (green Allan deviation) [94].

frequency transfer scheme could make use of the broad $f - 2f$ branch for detecting the master laser and then copy its properties throughout the optical domain exploiting dedicated comb branches.

3.8 Microwave generation

We have investigated the possibility of generating a low-noise microwave signal by using the comb as a bridge from the optical to the microwave domain [42, 89]. This section reports on the preliminary characterisation of a 100 MHz signal extracted from the comb repetition rate when it is phase-locked to an ultrastable oscillator.

The 100 MHz generation setup is shown in fig. 3.23. The comb repetition rate is phase-locked to the 1542 ultrastable laser (see the procedure in section 2.6.3) that we already used in the measurement discussed in section 3.6. Then the 1.56 µm comb output is sent to a fast photodiode for detecting f_{rep}. The 40th harmonic of f_{rep} (10 GHz) is filtered and sent to a 10× frequency divider, providing the 100 MHz output.

The 1542 nm ultrastable laser has a fractional instability of $3 - 5 \times 10^{-15}$ at 1 s

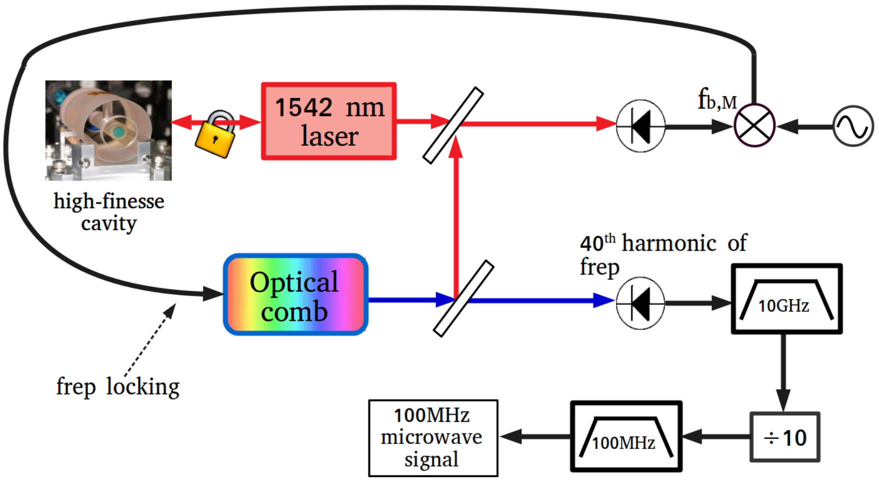

Figure 3.23: Optical-to-microwave setup for generating a low-noise microwave signal using the optical comb referenced to an ultrastable cavity.

of averaging time. To characterise such kind of signal a good reference oscillator is required, since after the down-conversion of the optical reference we compare directly two microwave oscillators. For this reason we cannot relies on any of the synthesizers available in the laboratory, as their instability would limit the measurement results.

A possible way to overcome the reference oscillator issue is to evaluate the 100 MHz stability through a three-cornered hat measurement [144]. In this technique pair-wise comparisons are performed between the oscillator under test and two independent oscillators. The instability of the oscillator under test σ_A is extrapolated from the relation

$$\sigma_\mathrm{A}^2 = \frac{1}{2}(\sigma_\mathrm{A,B}^2 + \sigma_\mathrm{A,C}^2 - \sigma_\mathrm{B,C}^2), \tag{3.19}$$

where $\sigma_\mathrm{i,j}$ refers to each pair-wise instability measurement between the three oscillator A, B, and C.

To apply this technique, we independently measured the 100 MHz comb-based signal against the 100 MHz signals provided by two H-masers by using a phasemeter with a 1 MHz bandwidth. In this way the three independent stability measurements $\sigma_\mathrm{100,HM1}$, $\sigma_\mathrm{100,HM2}$ and $\sigma_\mathrm{HM1,HM2}$ have been obtained, where the labels "100", "HM1"and "HM2"refer respectively to the comb-based singal and the two masers. Afterwards, the instability σ_{100} of the comb-based microwave is extrapolated by using eq. (3.19).

The result of this calculation is shown in fig. 3.24, where the Allan deviation is evaluated at different measurement bandwidth. As can be seen, the optical-to-microwave transfer at 100 MHz achieves a fractional stability of 3×10^{-14} at

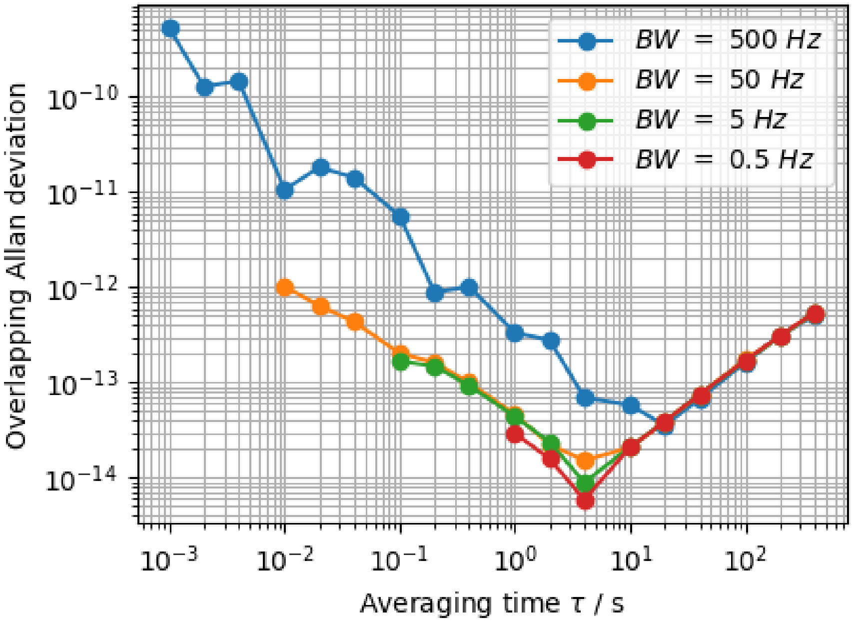

Figure 3.24: Overlapping Allan deviation of the 100 MHz signal generated by optical-to-microwave conversion using the optical comb referenced to an ultrastable laser. The instability has been evaluated by performing a three-cornered hat measurement using two H-masers.

1 s timescale on a 0.5 Hz equivalent measurement bandwidth. However, after few seconds the drift of the ultrastable reference cavity emerges, leading to a stability deterioration. Thus one of the first steps needed to improve the comb-based microwave will concern the compensation of the ultrastable laser's drift. This can be done for instance by using a second comb referenced to an H-maser if available, and then phase-locking the laser to one of the comb teeth taking advantage of the long-term $(\tau/\mathrm{s})^{-1/2}$ behaviour of the H-maser.

This preliminary evaluation allow us to consider this kind of frequency-division chain for future applications in our laboratory. One of the most interesting development would be the generation of a low-noise microwave source to be used as the local oscillator for our Cs-fountain primary standard ITCsF2 [91, 145]. In this way, we could investigate the possibility of improving the short-term instability of the Cs-fountain atomic clock.

Chapter 4

Optical frequency measurements

In this chapter two absolute optical frequency measurements of the INRiM ^{171}Yb clock are reported. The results are published in ref. [34] and [35]. The first measurement has been done with respect to the INRiM Cs fountain primary standard, the other one with respect to the International Atomic Time (TAI), which is computed from an ensemble of primary and secondary frequency standards located worldwide. Absolute frequency measurements have been realised using the optical comb to bridge the gap between the optical and microwave domain. Before detailing the clock measurements, a general description on how to use optical combs for determining absolute frequencies is provided. Then the characterisation of the optical comb contribution to uncertainty in absolute optical frequency measurements is presented.

An optical-to-optical clock comparison between the INRIM Yb clock and a ^{87}Sr-based transportable optical clock is also described in the last section of this chapter. Direct interspecies comparison of optical clocks is required to demonstrate the reliability of optical frequency standards and to evaluate their ultimate level of accuracy. The comparison has been made by performing an optical frequency ratio measurement using the optical comb as a transfer oscillator. The ^{171}Yb/^{87}Sr ratio results are published in [115].

4.1 Absolute optical frequency measurement

The equation describing the modes of an optical frequency comb provides a direct link between the optical and microwave domain, as anticipated in section 2.2. The absolute frequency ν_{opt} of an optical source can be measured through an heterodyne beatnote measurement with the nearest optical comb mode. Through the measurement of the offset frequency f_0, the repetition rate f_{rep} and the beatnote between the m^{th} comb mode and the optical sourcef_{beat}, ν_{opt} is determined through

f_{beat} sign determination by changing f_{rep}					
	$f_{\text{rep}} \nearrow$	$\wedge$	$f_{\text{beat}} \searrow$	$\Rightarrow$	$+f_{\text{beat}}$
	$f_{\text{rep}} \nearrow$	$\wedge$	$f_{\text{beat}} \nearrow$	$\Rightarrow$	$-f_{\text{beat}}$
	$f_{\text{rep}} \searrow$	$\wedge$	$f_{\text{beat}} \searrow$	$\Rightarrow$	$-f_{\text{beat}}$
	$f_{\text{rep}} \searrow$	$\wedge$	$f_{\text{beat}} \nearrow$	$\Rightarrow$	$+f_{\text{beat}}$
f_0 sign determination by changing f_0					
if $+f_{\text{beat}}$,	$f_0 \nearrow$	$\wedge$	$f_{\text{beat}} \searrow$	$\Rightarrow$	$+f_0$
if $+f_{\text{beat}}$,	$f_0 \nearrow$	$\wedge$	$f_{\text{beat}} \nearrow$	$\Rightarrow$	$-f_0$
if $+f_{\text{beat}}$,	$f_0 \searrow$	$\wedge$	$f_{\text{beat}} \searrow$	$\Rightarrow$	$-f_0$
if $+f_{\text{beat}}$,	$f_0 \searrow$	$\wedge$	$f_{\text{beat}} \nearrow$	$\Rightarrow$	$+f_0$

Table 4.1: f_{beat} and f_0 sign determination. $\nearrow$: increase; $\searrow$: decrease.

the relation

$$\nu_{\text{opt}} = m f_{\text{rep}} \pm f_0 \pm f_{\text{beat}}. \tag{4.1}$$

For the measurements presented in the previous chapter the discussion about the signs of the quantities f_0 and f_{beat} has been postponed. Below, the procedure for determining the correct signs and a generalised method to find the mode number m, which does not rely on high-accuracy a priori knowledge of ν_{opt}, are described.

The beatnote sign is determined by slightly changing the repetition rate and seeing how f_{beat} moves. If f_{beat} is positive, increasing f_{rep} moves the beatnote closer to the optical comb mode to which it is beaten, thus f_{beat} decreases. On the contrary, a negative f_{beat} will move far from the comb mode if f_{rep} increases, thus f_{beat} increases. Clearly, this procedure holds as well by decreasing f_{rep}, with opposite changes of f_{beat}. Once the f_{beat} sign is know, the ambiguity on f_0 sign is solved by varying f_0. For instance, by increasing f_0 all the optical comb modes are shifted towards higher frequencies if f_0 is positive, and viceversa. In the former case, a positive f_{beat} will get closer to the comb mode and decrease, while a negative f_{beat} will get farther from the comb mode and increase. In the latter case, the behaviour is opposite. Both procedures are summarised in table 4.1.

The integer mode number m is directly identified if ν_{opt} is already know with accuracy higher than half the separation between two consecutive comb frequency modes, i.e. f_{rep}. In this case, if the f_0 sign is already known, there is no ambiguity about m since only one value satisfies eq. (4.1) and the assignation of the f_{beat} sign comes as a direct consequence of the m choice. This method applies to optical frequency standards or ultrastable lasers whose frequency can be linked to well-known atomic transitions or is known from previous measurements and with slow frequency drift compared to f_{rep}. In other cases, without an optical frequency reference the information about ν_{opt} cannot be obtained with accuracy higher than hundreds of MHz. For instance, by using a wavemeter we achieve accuracy worse than the repetition rate value of our frequency combs, i.e. 250 MHz. To overcome this problem, m can be measured by changing the repetition rate by a quantity Δf_{rep}, so that ν_{opt} can be measured with respect to two different comb modes, namely m and $m + \Delta m$. The integer Δm is easily inferred by looking at f_{beat} moving across different comb modes while f_{rep} changes. By comparing the $f_{\mathrm{beat,1}}$ and $f_{\mathrm{beat,2}}$ beatnote measurements taken at f_{rep} and $f_{\mathrm{rep}} + \Delta f_{\mathrm{rep}}$, the mode number m is derived as

$$m = \Delta m \frac{f_{\mathrm{rep}} + \Delta f_{\mathrm{rep}}}{\Delta f_{\mathrm{rep}}} + \frac{f_{\mathrm{beat,2}} - f_{\mathrm{beat,1}}}{\Delta f_{\mathrm{rep}}}, \tag{4.2}$$

where the ambiguity on the f_0 and $f_{\mathrm{beat,i}}$ signs has been omitted for the sake of clarity. This method can be applied as long as the variation of the optical source frequency ν_{opt} during the measurement is lower than the difference Δf_{rep} between the two repetition rates. This is satisfied for most of the laboratory lasers that require high-accuracy absolute measurement, whose drift is in the worst cases of the order of tens of $\mathrm{Hz\,s^{-1}}$. The $f_{\mathrm{beat,i}}$ measurement stability is limited by the reference used for the PLLs that stabilise f_{rep} and f_0, which usually allows unambiguous evaluation of m. If needed, Δm can be increased to have more tolerance on the stability requirement.

4.1.1 Comb validation for absolute optical frequency measurements

In a metrological measurement chain, using optical combs to perform absolute frequency measurements providing traceability to the SI second requires that the comb does not degrade the measurement uncertainty at the level of the primary standard. In 2015 a first validation of our frequency comb (referred below as comb$_1$) has been carried out by comparing two similar systems, i.e. two erbium-fibre combs. The reference comb (comb$_2$) is another commercial MenloSystem erbium-fibre comb with 250 MHz f_{rep}. f_{rep} and f_0 of both combs are stabilised to RF references provided by H-masers. We simultaneously measured a 1542 nm cavity-stabilised laser (see section 3.6) with the two combs and evaluated the agreement between the corresponding absolute frequency values. The 1542 nm radiation is sent to the two combs by phase-stabilised fibre links. The 1542 nm laser long-term frequency drift is corrected by implementing a digital phase-lock to the H-maser. Since the comb is phase-locked to the H-maser, the long-term stabilisation of the laser is achieved by using the beatnote between the laser and comb$_1$ to generate the error signal for the feedback loop.

The absolute frequencies have been calculated from the measurement of the beatnote signals, f_0 and f_{rep} on the same multi-channel K+K frequency counter at 1 s of gate time. In fig. 4.1 the typical fractional frequency instability of the ultrastable laser as measured with the two combs is presented. In both cases the

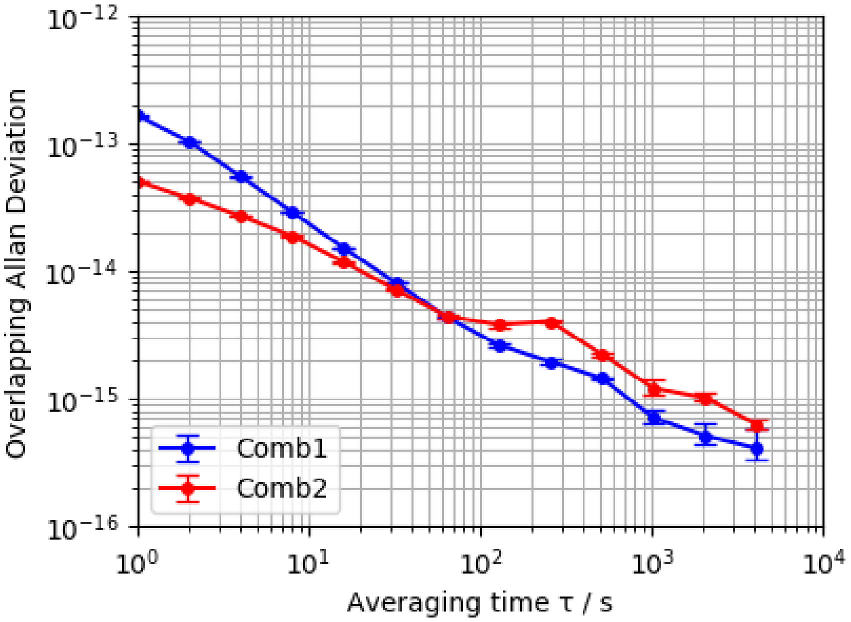

Figure 4.1: Factional instability in terms of overlapping Allan deviation of the 1542 nm laser measurement performed using comb$_1$ (blue) and comb$_2$ (red).

long-term behaviour is dominated by white frequency noise, reaching the level of 4×10^{-16} for comb$_1$ (blue curve) and 6×10^{-16} for comb$_2$ (red curve) after 4000 s of averaging time, limited by the measurement time. The 1 s-instability depends on the local oscillator used as the reference to stabilise f_{rep}. For comb$_1$ this is realised as described in section 2.6.3. For comb$_2$ the f_{rep} stabilisation exploits a similar scheme, but in this case the 4th harmonic of the 250 MHz f_{rep} is mixed to the 1 GHz signal generated by a tenfold multiplication of a 100 MHz H-maser reference. A low-noise frequency multiplier is employed, leading to a 5×10^{-14} instability at 1 s, a factor of two better than comb$_1$. For averaging time greater than 40 s the blue curve does not represent the actual residual instability of the measurement because of the common noise between comb$_1$ and the 1542 nm laser, since their beantote is in-loop as it it used in the PLL that compensates for the CW-laser drift. Finally, the instability excess around 400 s is related to the air conditioning of the laboratory, as already highlighted in the previous chapter.

This measurement was repeated several times within a period of three months. The difference between the absolute frequencies measured with the two combs was calculated for each dataset and its uncertainty was computed as the last point of the corresponding Allan deviation. The results of eight measurements are reported in fig. 4.2. The red shaded region indicates the weighted average of the sample and its 1-σ region, which allow us to claim an agreement at the level of 1×10^{-16}. A χ^2

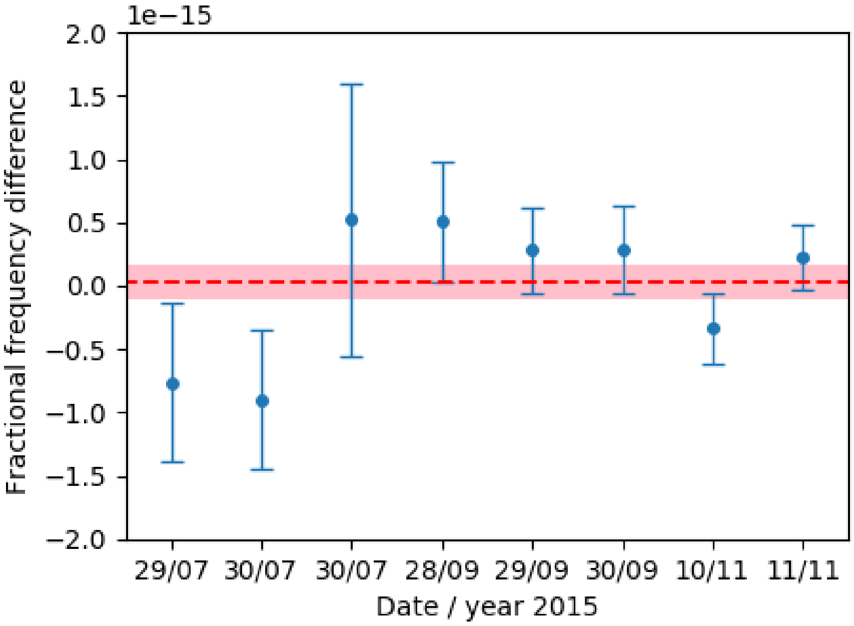

Figure 4.2: Collection of the absolute frequency difference measurements between the two combs. The red dashed line indicates the weighted average of the points within its uncertainty bar represented by the red shaded region.

test confirms that these points follow a normal distribution around the zero-offset value with a 95% confidence level. The accuracy level is limited by statistics. This result shows that the optical comb does not limit absolute frequency measurements at the accuracy level achieved by the local realisation of the SI second.

4.1.2 ^{171}Yb optical clock absolute measurement

Absolute measurement with respect to the Cs fountain In 2016 we performed the first absolute frequency measurement of the ^{171}Yb optical lattice clock operating at INRiM with respect to the INRiM Cs primary standard ITCsF2. The metrological chain is shown in fig. 4.3. The Yb clock laser is measured by the frequency comb referenced to the H-maser. The Cs fountain is continuously operating during the measurement campaign, allowing the evaluation of the H-maser frequency deviation with respect to the SI second.

The $^1S_0 - {}^3P_0$ atomic transition of the Yb clock is probed by using the 578 nm frequency-doubled ultrastable laser described in section 3.3. A fraction of the 578 nm light is sent to the Yb atoms and is locked to the atomic transition by changing the driving frequency of an AOM (f_{lockAOM}) located before the atoms. At the same time the 578 nm light is sent to the frequency comb. The comb measures

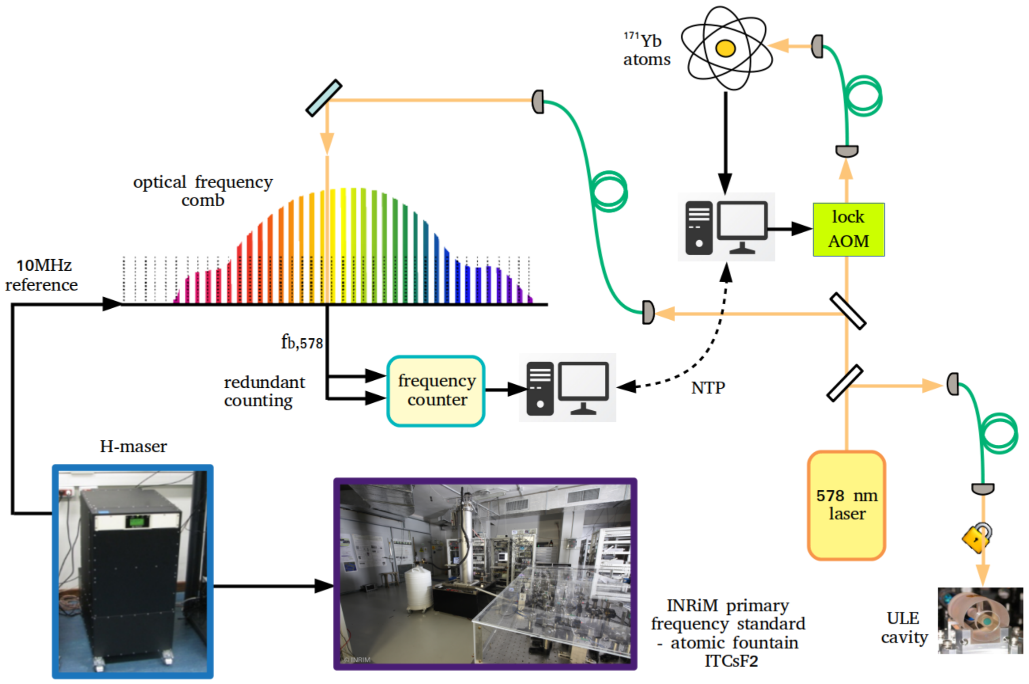

Figure 4.3: Metrological chain developed for the absolute frequency measurement of the Yb clock with respect to the INRiM primary standard ITCsF2 [34]. AOM: acousto-optic modulator; ULE: ultra-low expansion glass.

the frequency of the laser referenced to the cavity without being affected by the changes of f_{lockAOM}. The laser light is delivered through phase-stabilised PM fibre links, which have been validated at the 1×10^{-18} level for 1000 s of averaging time [133].

The beatnote $f_{\mathrm{b},578}$ between the comb and the laser is redundantly counted on a multi-channel K+K counter to detect the occurrence of cycle slips. Data are discarded if the difference between the two $f_{\mathrm{b},578}$ readings is higher than 200 mHz. Measurements of the clock laser at the comb and f_{lockAOM} need to be combined to determine the absolute clock frequency. The two measurements are recorded at different rates by two separate PCs, hence interpolation is needed to have common timestamps of the two datasets. To avoid errors in the interpolation the two PCs are synchronised via the network time protocol (NTP) provided by INRiM within 3 ms. During the time between two corrections of the driving frequency f_{lockAOM} there is no direct link between the cavity drift and the atomic reference, resulting in a frequency error even in the ideal case of perfect matching of the timestamps. Considering a cavity drift of $0.1\ \mathrm{Hz\,s^{-1}}$, an uncertainty of 6×10^{-19} is estimated.

From the measurements of $f_{\mathrm{b},578}$ and f_{lockAOM}, and taking into account the systematic Yb clock frequency shift $\Delta\nu_{\mathrm{syst}}$, the optical clock frequency $\nu_{\mathrm{Yb}}^{\mathrm{H}}$ is evaluated with respect to the H-maser as

$$\nu_{\mathrm{Yb}}^{\mathrm{H}} = m_{578} f_{\mathrm{rep}} - 2f_0 + f_{\mathrm{b},578} + f_{\mathrm{lockAOM}} + \Delta\nu_{\mathrm{syst}}, \tag{4.3}$$

where $m_{578} = 2\,073\,184$, f_0 has negative sign and it is counted twice since the comb light is generated by a frequency-doubling process, and $f_{\mathrm{b},578}$ has positive sign. Finally, the traceability to the SI second is achieved by considering the correction $\Delta f_{\mathrm{H}} = f_{\mathrm{H}}^{\mathrm{Cs}} - f_{\mathrm{H}}$, where $f_{\mathrm{H}}^{\mathrm{Cs}}$ is the H-maser frequency measured by the primary standard and f_{H} its nominal value, used in eq. (4.3). As a consequence, the Yb absolute frequency with respect to the SI second $\nu_{\mathrm{Yb}}^{\mathrm{Cs}}$ is

$$\nu_{\mathrm{Yb}}^{\mathrm{Cs}} = \nu_{\mathrm{Yb}}^{\mathrm{H}} \frac{f_{\mathrm{H}} + \Delta f_{\mathrm{H}}}{f_{\mathrm{H}}} = \nu_{\mathrm{Yb}}^{\mathrm{H}} \left(\frac{f_{\mathrm{H}}^{\mathrm{Cs}} - f_{\mathrm{H}}}{f_{\mathrm{H}}} + 1 \right). \tag{4.4}$$

During the campaign, 31 measurements have been collected, for a total measurement time of 227 h. The resulting $^{171}\mathrm{Yb}$ $^1\mathrm{S}_0 - {}^3\mathrm{P}_0$ unperturbed atomic transition is

$$\nu_{\mathrm{Yb}} = 518\,295\,836\,590\,863.59(31)\ \mathrm{Hz}, \tag{4.5}$$

with a 5.9×10^{-16} fractional uncertainty limited by the Cs fountain primary standard. This accounts for 4×10^{-16} systematic uncertainty of the Cs fountain [91], and 3.9×10^{-16} statistical uncertainty dominated by the instability of the Cs fountain. The Yb clock accuracy budget is detailed in [34] and contributes to the measurement with an uncertainty of 1.6×10^{-16} (see table 4.2 for the list of the separate contributions to the Yb clock budget).

The uncertainty budget of the absolute frequency measurement is detailed in table 4.3. The gravitational redshift contribution is also included according to the prediction given by general relativity [146]

$$\frac{\Delta\nu}{\nu_0} = \frac{g\Delta h}{c^2} = \frac{\Delta U}{c^2}, \tag{4.6}$$

where ν_0 is the clock transition with respect to the geoid surface (typically chosen as the reference height), g is the local value of the gravity acceleration, Δh is the height difference between the two clocks and ΔU the difference of the gravity potential between the clock sites. At INRiM the local gravitational potential related to the geoid has been measured within the European project "International timescales with optical clocks"(ITOC) [108, 147]. By measuring a height difference between the Yb and Cs atoms, $\Delta h(\mathrm{Yb} - \mathrm{Cs}) = 0.15(2)$ m, the uncertainty due to the differential gravitational redshift is 2×10^{-18}.

Absolute measurement via the International Atomic Time (TAI) Typically absolute frequency measurements are performed against local realisations of primary frequency standards. However, when there is no possibility of a direct

Contribution	**Shift** $\times 10^{16}$	**Uncertainty** $\times 10^{16}$
Linear lattice light	−0.4	0.8
Nonlinear lattice light	−1.2	1.0
Blackbody radiation (room)	−23.53	0.25
Blackbody radiation (oven)	−0.21	0.08
Zeeman	−2.7	0.4
Collisions	−0.2	0.6
Probe light	0.1	0.35
AOM switching	—	0.04
Background gas	—	0.15
1st order Doppler	—	0.5
Servo error	—	0.1
DC Stark	—	0.1
Tunnelling	—	0.04
Fibre links	—	0.01
Line pulling	—	0.04
Gravitational redshift	260.12	0.06
Total	232.0	1.6

Table 4.2: Uncertainty budget of the INRiM Yb optical lattice clock (2017) [34]. The uncertainties are reported in fractional unities.

Contribution	**Uncertainty** $\times 10^{16}$
Cs fountain	4.0
Statistics	3.9
Yb clock	1.6
Frequency comb	1.0
Differential gravitational redshift	0.02
Fibre link	0.01
Synchronization	0.006
Total	5.9

Table 4.3: Uncertainty budget of the Yb clock absolute frequency measurement against the Cs fountain [34]. The uncertainties are reported in fractional unities.

measurement with respect to a Cs fountain clock, traceability to the SI second can be obtained with respect to TAI [9, 148–150]. The Bureau of Weights and Measures (BIPM) computes the TAI timescale by comparing frequency standards maintained in a number of laboratories over the world exploiting satellite-based techniques [151].

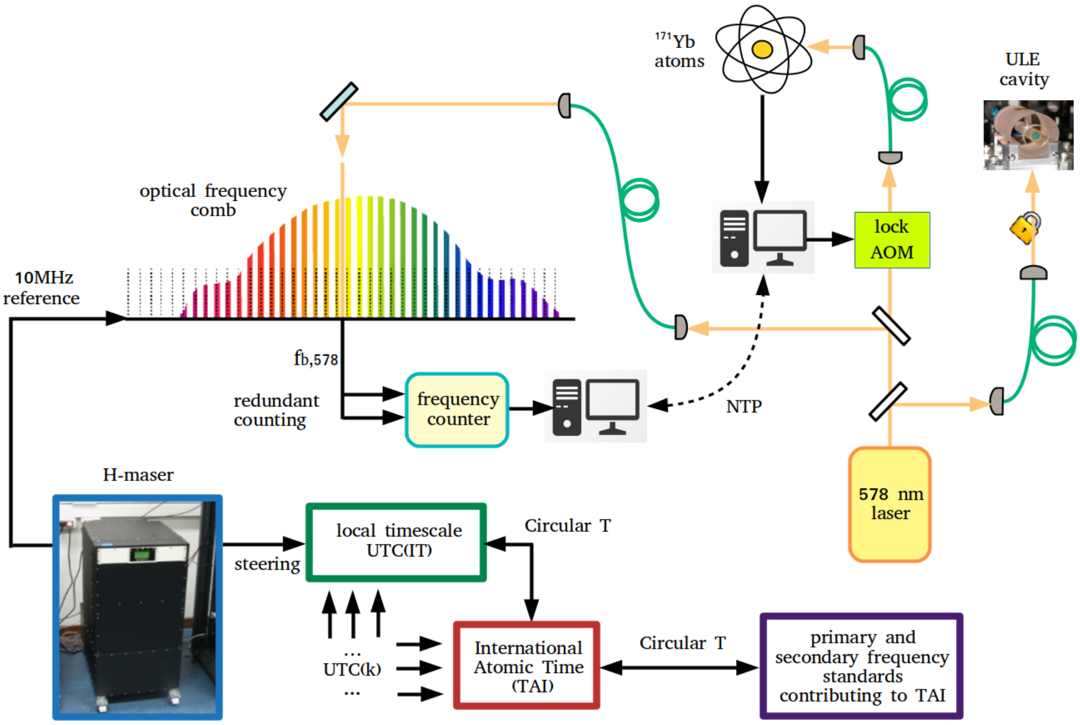

Figure 4.4: Metrological chain developed for the absolute frequency measurement of the Yb clock by exploting the link to the International Atomic Time (TAI) [35]. UTC(IT): Coordinated Universal Time generated at INRiM; UTC(k): Coordinated Universal Time of other laboratories; AOM: acousto-optic modulator; ULE: ultra-low expansion glass.

Secondary frequency standards also contribute to TAI computation, even though up to now few optical frequency standards have submitted their data to BIPM [9, 110, 152]. Therefore, absolute optical frequency measurements will benefit a more accurate evaluation of TAI as more optical frequency standards contribute to its computation.

TAI timescale is evaluated every 5 days and its value with respect to the SI second is published every month in the Circular T bulletin [153]. BIPM is also in charge of the dissemination of Coordinated Universal Time (UTC), i.e. the timescale commonly used worldwide. TAI and UTC differ by an integer number of seconds, since leap seconds are applied to UTC time to take into account for the slowing down of the Earth rotation [151]. Local timescales UTC(k) are maintained in many laboratories and they are compared through satellite time and frequency transfer. The deviation of the local UTC(k) time from UTC is evaluated every 5 days and it is reported in Circular T once a month.

In 2019 we performed the absolute frequency measurement of the INRiM Yb optical lattice clock using a measurement chain that provided a link to TAI, as outlined in fig. 4.4. The first part of the chain is the same as for the previous

Contribution	**Shift** $\times 10^{17}$	**Uncertainty** $\times 10^{17}$
Lattice light	7.6	2.0
Blackbody radiation (room)	−235.0	1.2
Blackbody radiation (oven)	−1.7	0.8
Zeeman	−0.693	0.014
Collisions	−5.9	0.2
Probe light	0.09	0.05
AOM switching	—	0.4
Background gas	−0.5	0.2
Servo error	—	0.3
DC Stark	−1.6	0.9
Tunnelling	—	0.4
Fibre links	—	0.01
Line pulling	—	0.02
Gravitational redshift	2599.5	0.3
Total	2361.8	2.8

Table 4.4: Updated uncertainty budget of the INRiM Yb optical lattice clock (2019) [35]. The uncertainties are reported in fractional unities.

measurement against INRiM Cs fountain, where the clock laser is measured by the optical comb referenced to the H-maser. The local timescale UTC(IT) is generated by steering the same H-maser with an auxiliary output generator to keep in step with UTC and it is compared to the other local timescales UTC(k) via satellite transfer. By using the data contained in the Circular T bulletin the difference between UTC(IT) and TAI is then calculated, allowing the final link to the SI second provided by the primary and secondary frequency standards from which the TAI timescale is generated. The measurement campaign lasted five months, with a total of 381 h of measurement of the Yb clock, which has been operated for few hours at a time. Uncertainty and correction due to the optical clock intermitted operation have been accounted for by using the H-maser and TAI as flywheels from the Yb frequency standard to the SI second. The detailed uncertainty evaluation of the measurement chain is presented in [35], together with the updated uncertainty budget of the Yb clock, which has been characterised at the 2.8×10^{-17} level (see table 4.4 for the list of the separate contributions to the Yb clock budget). For the comb contribution we referred to the characterisation done for the previous absolute frequency measurement. The new measurement of the ^{171}Yb $^1\text{S}_0 - {}^3\text{P}_0$ unperturbed atomic transition is

$$\nu_{\text{Yb}} = 518\,295\,836\,590\,863.61(13)\ \text{Hz}, \tag{4.7}$$

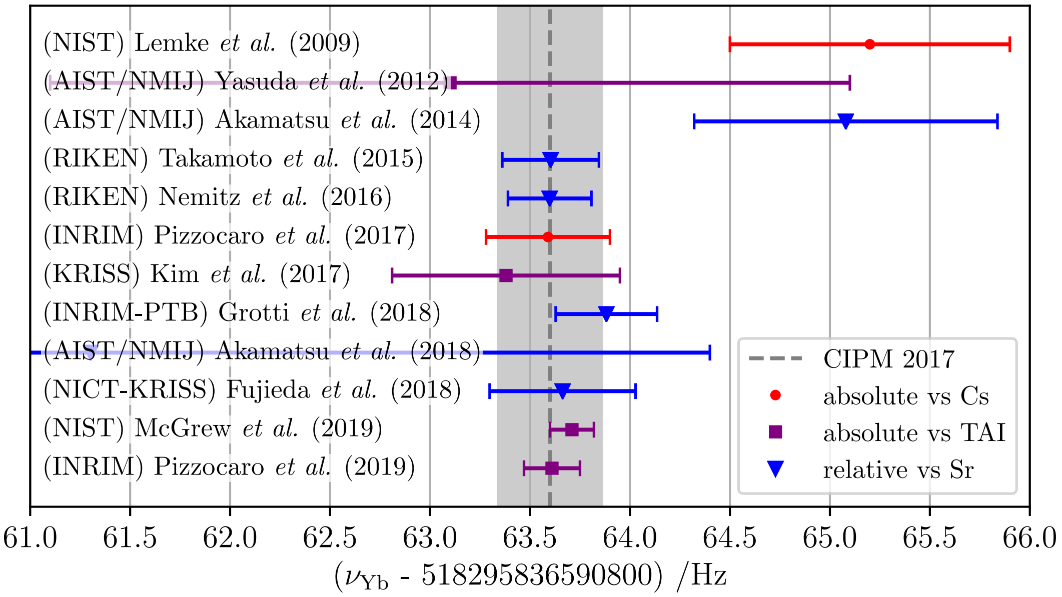

Figure 4.5: Absolute optical frequency measurements of the $^1\mathrm{S}_0 - {}^3\mathrm{P}_0$ transition of the ^{171}Yb clock performed worldwide [9, 34, 35, 107, 115, 154–162]. The data list includes measurements performed with respect to local Cs fountains, through the link to the SI second provided by TAI and from the frequency ratio between ^{171}Yb and ^{87}Sr frequency standards. The recommended 2017 CIPM value is represented by the dashed grey line, with the grey shaded region indicating its uncertainty.

with an uncertainty of 2.6×10^{-16} dominated by the satellite transfer in the comparison between UTC(IT) and TAI, whose uncertainty contribution is 1.4×10^{-16}. The frequency standards used for the TAI computation contributed with a uncertainty of 1.2×10^{-16}, i.e. the level of accuracy that can be achieved with the current realisation of the SI frequency standard.

Summary The two absolute frequency measurements presented above are in agreement with the frequency standard value recommended by CIPM [163]

$$\nu_{\mathrm{Yb}}(\mathrm{CIPM2017}) = 518\,295\,836\,590\,863.6(5)\ \mathrm{Hz}. \tag{4.8}$$

The whole set of absolute measurements performed so far by several research groups is shown in fig. 4.5. The data collection include measurements performed with respect to local Cs fountains, through the link to the SI second provided by TAI and from the frequency ratio between ^{171}Yb and ^{87}Sr frequency standards. The absolute frequency of the ^{87}Sr-based standard is independently evaluated and its recommended value is [164]

$$\nu_{\mathrm{Sr}}(\mathrm{CIPM2017}) = 429\,228\,004\,229\,873.0(4)\ \mathrm{Hz}. \tag{4.9}$$

Thus, the absolute frequency ν_{Yb} is extracted by multiplying the $\nu_{\mathrm{Yb}}/\nu_{\mathrm{Sr}}$ frequency ratio by $\nu_{\mathrm{Sr}}(\mathrm{CIPM2017})$. The consistency between these absolute frequency measurements supports the Yb-based optical lattice clock as secondary frequency standard and it highlights the possibility of a future redefinition of the SI second based on optical frequency standards.

4.2 Optical frequency ratio measurement

The direct comparison between optical frequency standards is one of the key steps to strengthen their reliability. Optical frequency ratios can be evaluated by using optical combs through the transfer oscillator technique [28, 116], as described in section 3.1. Therefore, frequency ratio measurements are not limited by the RF-stabilisation of the comb, which in principle can be used in free-running operation. This allows the characterisation of the ultimate uncertainties of optical frequency standards at a level that is not feasible when they are compared to the current primary frequency standard.

4.2.1 Comparison between the INRiM Yb optical clock and a transportable Sr optical clock

Within the ITOC project, the INRiM ^{171}Yb optical lattice clock has been compared to a transportable ^{87}Sr optical lattice clock developed at the Physikalisch-Technische Bundesanstalt (PTB), the German National Metrology Institute [165]. In 2016 the Sr clock has been transported for the first time and it has been brought to the INRiM campus site, where the ^{171}Yb/^{87}Sr frequency ratio has been measured.

Remote atomic clock comparison can be performed via different techniques, among them satellite-based comparison is widely used. However, when comparing optical frequency standards satellite-based techniques do not allow to assess the clocks uncertainty. Networks of fibre-links have been developed to overcome this problem. In a different approach, interest in building transportable optical clocks arises since they allow direct comparison of optical frequency standards eliminating the need of an intermediate frequency transfer channel to connect the clocks and they can be moved to sites not reached by fibre links.

The measurement of the ^{171}Yb/^{87}Sr frequency ratio has been performed by means of the optical comb as shown by the metrological chain in fig. 4.6. The PTB Sr clock apparatus was enclosed in a car trailer positioned outside the building where the Yb clock is operated. Only the 698 nm ultrastable laser used to probe the $^1\mathrm{S}_0 - {}^3\mathrm{P}_0$ ^{87}Sr clock transition was moved outside the trailer and located inside

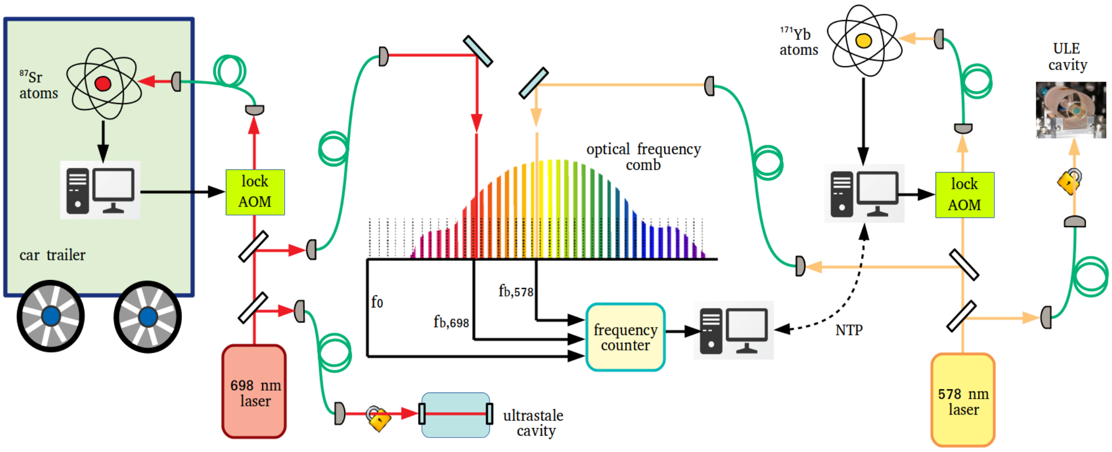

Figure 4.6: Metrological chain developed to compare the INRIM Yb clock and the PTB Sr transportable clock by measureing their frequency ratio with the optical comb [115]. AOM: acousto-optic modulator; ULE: ultra-low expansion glass.

the comb laboratory, and it was sent to the clock through a 50 m phase-stabilised fibre.

The clock laser radiations are detected by using two independent branches of the optical comb. The Yb clock laser is measured as reported in section 3.3.1 and section 4.1.2. The Sr clock laser is measured against the comb branch generated through the red PCF that broadens the 780 nm frequency-doubled comb light, resulting in an output spanning the 600 – 950 nm region (see section 2.6.2). As for the $f_{\mathrm{b},578}$ detection, we implemented a free-space interferometer to measure the 698 nm beatnote signal $f_{\mathrm{b},698}$, which achieved a 35 dB SNR in a 100 kHz RBW. The beatnotes between both clock lasers and the comb are redundantly counted to detect cycle slips. Through the procedure described in section 3.1, the ratio $R = \nu_{\mathrm{Yb}}/\nu_{\mathrm{Sr}}$ is evaluated as

$$R = \frac{\nu_{\mathrm{Yb}}}{\nu_{\mathrm{Sr}}} = \frac{m_{578}}{m_{698}} \left(1 - \frac{(2f_0 + f_{\mathrm{b},698} + \Delta\nu_{\mathrm{Sr}}) - (2f_0 + f_{\mathrm{b},578} + \Delta\nu_{\mathrm{Yb}})\frac{m_{698}}{m_{578}}}{\nu_{\mathrm{Sr}}} \right), \qquad (4.10)$$

where $m_{698} = 1\,716\,912$ is the number of the comb mode to which the Sr clock laser is beaten and $\Delta\nu_{\mathrm{Sr}}$ and $\Delta\nu_{\mathrm{Yb}}$ quantify the systematic corrections that have to be applied to find the $^1\mathrm{S}_0 - {}^3\mathrm{P}_0$ unperturbed transitions.

Seven frequency ratio measurements were performed over two weeks, collecting data for a total time of 31 000 s. The corresponding averaged result is [115]

$$R = 1.207\,507\,039\,343\,338\,41(34). \qquad (4.11)$$

The uncertainty budget of the measurement is outlined in table 4.5. The ratio instability was about $2 \times 10^{-14}/\sqrt{\tau/s}$, leading to an ultimate statistical uncertainty

Contribution	**Uncertainty** $\times 10^{16}$
Sr systematics	1.8
Yb systematics	1.6
Statistics	1.1
Differential gravitational redshift	0.1
Frequency comb	0.3
Fibre link	0.01
Synchronisation	0.006
Total	2.8

Table 4.5: Uncertainty budget of the ^{171}Yb/^{87}Sr frequency ratio measurement [115]. The uncertainties are reported in fractional unities.

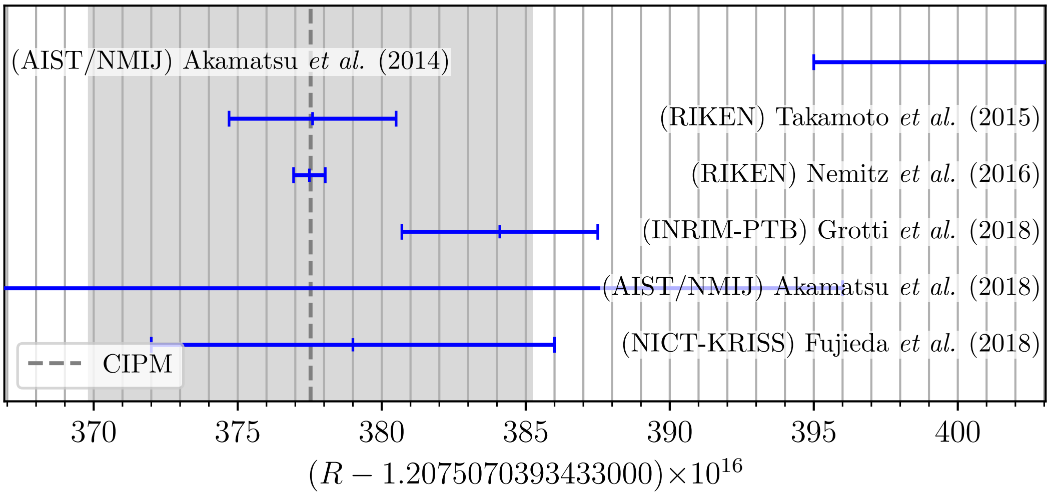

Figure 4.7: ^{171}Yb/^{87}Sr optical frequency ratio measurements performed in different laboratories [107, 115, 158, 159, 161, 162]. The frequency ratio value calculated from the 2017 CIPM recommended values is represented by the dashed grey line, with the grey shaded region indicating its uncertainty.

of 1.1×10^{-16}. The fibre links and computers' synchronisation contributions and the Yb clock accuracy are the same as those reported in section 4.1.2. The Sr clock systematic uncertainty was 1.8×10^{-16}, larger than the 7.4×10^{-17} value previously assessed at PTB [165]. This was mainly related to technical difficulties encountered in performing a new characterisation at INRiM [115].

Concerning the comb contribution, at the time of the ^{171}Yb/^{87}Sr measurement campaign the optical comb had been validated at the 3×10^{-17} level for frequency ratio measurements. This validation guaranteed that the comb could sustain the

^{171}Yb/^{87}Sr measurement with an uncertainty contribution one order of magnitude below the clocks' accuracy.

Finally, as in the case of the absolute measurement of the Yb clock with respect to the Cs fountain, the differential gravitational redshift for the ^{171}Yb/^{87}Sr comparison has been evaluated. The two optical clocks were located at a height difference $\Delta h = 3.6(1)$ m, leading to an uncertainty of 1×10^{-17}.

The ^{171}Yb/^{87}Sr frequency ratio measurements performed to date by different research groups are summarised in fig. 4.7, compared to the ratio $R_0(\mathrm{CIPM2017}) = 1.207\,507\,039\,343\,337\,75(77)$ calculated via the CIPM recommended frequencies for the ^{171}Yb and ^{87}Sr standards [163, 164]. Our measurement shows a discrepancy of two standard deviations compared to the most accurate result obtained so far [107]. The motivation for this disagreement has not yet been found.

Further measurements of the ^{171}Yb/^{87}Sr ratio will be carried out at INRiM, once the ^{87}Sr stationary optical clock under development will be operating. Future optical frequency ratio measurements will benefit from the optical-to-optical comb transfer characterisation presented in chapter 3, with a comb contribution to the uncertainty demonstrated at the 3×10^{-19} level.

Chapter 5

Characterisation of backreflection signals in optical fibres for fibre-noise cancellation

During the third year of my Ph.D. I spent six months as a visiting Ph.D. student at the National Physical Laboratory (NPL), UK. NPL is the UK's National Measurement Institute, where the national primary measurement standards are developed and maintained. I worked in the Time and Frequency group, which is part of the NPL Quantum Metrology Institute. NPL Time and Frequency group deals with the operation of the UK national time scale UTC(NPL) and primary frequency standards, providing also dissemination of accurate time and frequency signals. My secondment research has been carried out under the supervision of Dr. Giuseppe Marra and it has been supported by the European Union project Q-Sense (call H2020-MSCA-RISE-2015). I was also guest at the Optoelectronic Research Centre of the University of Southampton, UK, where part of the results presented in this chapter have been obtained.

NPL has developed techniques for the dissemination of time and frequency signals using pulsed laser sources. Accurate microwave and optical frequency transfer, as well as time transfer, have been demonstrated over fibre spools and installed fibre links. The results obtained showed that these techniques are suitable for state-of-the-art frequency references and 100 ps-accuracy timing signals transfer over fibre networks [32, 166, 167]. Moreover, an operating optical fibre link between NPL and Paris allows atomic clock comparisons [168].

This chapter describes my research activity at NPL, which concerned the theoretical and experimental study of technical limitations and improvements of time and frequency transfer techniques using optical fibres, facing real-life scenarios including spurious reflection signals over fibres and chromatic dispersion effect.

5.1 Time and frequency dissemination

The advent of atomic clocks as high-precision measurement devices has lead to the development of different techniques for time and frequency signal dissemination, both for reaching remote users and for comparing clocks between distant research facilities. Depending on the transfer channel, different noise sources modify the path length of electromagnetic waves that propagate between two remote sites, causing phase and stability deterioration of the original signals. Therefore, the critical issue in the transmission of atomic clock signals concerns the capability of cancelling any additional noise that could degrade the accuracy of the clocks.

The dissemination between distant locations is realised by means of free-space satellite transfer, optical fibre links or free-space optical transfer. Historically, the first techniques have been based on transmission of microwave signals exploiting satellites from the Global Navigation Satellite System (GNSS), where atomic clocks on the ground measure time signals from the satellites. Time accuracy of about 10^{-16} after few days [30] has been demonstrated. In a different approach, the clock signals travel between different sites in two-way satellite time and frequency transfer (TWSTFT), using geostationary satellites as repeaters. In this case the accuracy level is better than 10^{-15} after one day of averaging time [169]. However, both techniques are not suitable to accurately disseminate the new generation of optical atomic clocks, which achieve accuracy of orders of magnitude better [122, 123]. Alternative dissemination techniques have been investigated, leading to the optical fibre link-based dissemination that guarantees superior performances, as described in the next section. Nevertheless, satellite-based transfer is to date the only tool available for transoceanic dissemination.

5.2 Optical link-based dissemination

On continental baselines, time and frequency transfer through optical fibre links can sustain the demanding high-accuracy level dissemination required by state-of-the-art optical clocks. Fibre links provide a robust medium to confine laser light ensuring better insulation with respect to free-space signal propagation. Fibre dissemination exploits the fibre network developed for internet traffic, which is based on the Dense Wavelength Division Multiplexing (DWDM) technology. A single channel of the of the International Telecommunication Union (ITU) grid is needed for metrological purposes, hence it is possible to use the fibre network without interfering with the data transmission. This is the so-called "dark channel"architecture, while "dark fibre"architecture refers to using the fibre only for dedicated applications as time and frequency dissemination.

Depending on the application required, RF and optical dissemination techniques using CW-laser or pulsed laser radiation transmitted over fibre links have been developed. Optical frequency signals can be transmitted by phase-locking a telecom CW-laser to an atomic frequency standard using optical frequency combs. On the other hand, ultrastable RF and optical frequency signals can be transferred by directly referencing optical combs to a frequency standard.

RF dissemination can be obtained by applying an amplitude modulation on the optical carrier of a free-running CW-laser. At the user end the signal can be recovered by detecting the modulation signal on a photodiode. A 10 GHz signal has been transmitted on a 86 km-long network reaching a residual stability at the 10^{-18} level after one day of measurement [170]. On the other hand, direct dissemination of the optical carrier improves the stability level thanks to the five orders of magnitude higher frequency compared to the microwave domain, leading to better resolution for tracking the phase fluctuations that are experienced along fibre links. Thanks to the compensation of the fibre-noise through a Doppler cancellation scheme (see section 5.3), optical dissemination in the low 10^{-19} regime on a few hours timescale has been demonstrated over fibre links longer than 1000 km [171–173].

Alternatively to CW-laser dissemination, injecting optical comb or mode-locked laser (MLL) pulses into fibre links make possible to simultaneously transfer RF and optical signals. In this case optical carrier dissemination is made by choosing one of the comb optical modes to be transmitted, while the RF-transfer is accomplished by detecting the repetition rate of the comb at the remote end. With this technique dissemination of RF-signal has been demonstrated at the low 10^{-17} level over a 86 km fibre link [166], while optical comb mode has been transferred over 7.7 km-long fibre spool with accuracy of few parts in 10^{-18} [167]. In addition, time transfer with 100 ps accuracy over a 159 km-long fibre link has been performed using an optical comb and encoding the timing information over the optical pulses [32].

To conclude the summary of optical-based transfer technique, we mention also the free-space optical dissemination. It is based on sending MLL pulses through air, avoiding the limitation of having a fibre network available between remote sites. As a drawback, turbulences in the atmosphere represent a critical issue since are high phase-noise sources, which do not allow long-duration measurements. By using a two-way comparison similar to the two-way satellite scheme optical oscillators have been compared at the 10^{-19} stability level at 1000 s over a 4.4 km free-space link [174].

5.3 Phase-noise cancellation in optical fibre links

Time and frequency transfer techniques have to accurately suppress the noise introduced along the path between two sites. In optical fibre dissemination long-term temperature variations and acoustic noise and vibrations acting on shorter timescales are the the main noise sources that deteriorate the delivered signals. The most used fibre-noise cancellation scheme relies on a Doppler-based technique, which has been firstly proposed in 1994 [132]. Its operating principle is outlined in fig. 5.1, referring to optical carrier dissemination using a CW-laser. The noise suppression is achieved by implementing a PLL that acts on an actuator to compensate for the noise accumulated in a round-trip along the fibre link. The error signal used to feed the PLL is generated from the comparison between the local reference source and the light that travels back from the remote site. To detect the beatnote signal between the local reference and the round-trip light two partial reflectors are installed, the first one before injecting the laser in the fibre link, the other at the remote end. The laser source has to be chosen in order to avoid additional noise due to the self-beating of the laser itself. In other words, narrow-linewidth lasers are required, with coherence length larger than the round-trip time T_{rt}. For this reason, lasers phase-locked to ultrastable optical cavities are employed, achieving linewidth narrower than 10 Hz. Usually the 44$^{\mathrm{th}}$ channel of the ITU grid centred at 1542.14 nm is used for fibre dissemination, hence lasers that emit at frequency within the channel bandwidth (100 GHz) are employed. An acousto-optic modulator (AOM$_1$) is placed at the local laboratory before launching the light into the fibre and it is used to apply the correction given by the PLL by changing the AOM frequency. At the remote end another frequency-modulator (AOM$_2$) is used to distinguish between the back-travelling signal and unwanted spurious backreflections that are at the same frequency of the light injected after AOM$_1$.

Note that the compensation scheme above presented applies the correction on the laser frequency, while there is no stabilisation of the optical path length. Indeed, for frequency dissemination the absolute delay introduced by the path length variations does not represent an issue. Conversely, for time or frequency comb transfer optical path length stabilisation is required. In these applications fibre-stretchers and temperature-controlled fibre spools are chosen as actuators instead of AOMs.

In a different approach, a two-way scheme that can be used only to perform comparisons between two frequency standards is based on launching the clock signals from the two laboratories along the same fibre [175]. In this way, there is no need of fibre-noise cancellation, since the two signals experience common-mode noise fluctuations by travelling in opposite directions.

Over several hundreds of km-long fibre links the dissemination technique described so far requires a modification of the telecom fibre network. The laser power decreases as the light propagates through the fibre because of Rayleigh scattering and absorption from the fibre medium, as well as due to discontinuities given by connectors and fibre splicings. Although the minimum loss value at 1.56 µm has improved up to 0.2 dB/km [67], fibre amplifiers are needed to recover the signal power after propagation over distances of about tens of km. In standard telecom fibre links unidirectional amplifiers are commonly employed, typically erbium-doped fibre amplifiers (EDFA) supplied with isolators to avoid any stray backreflection. Since the Doppler cancellation scheme requires the detection of the round-trip light, there is

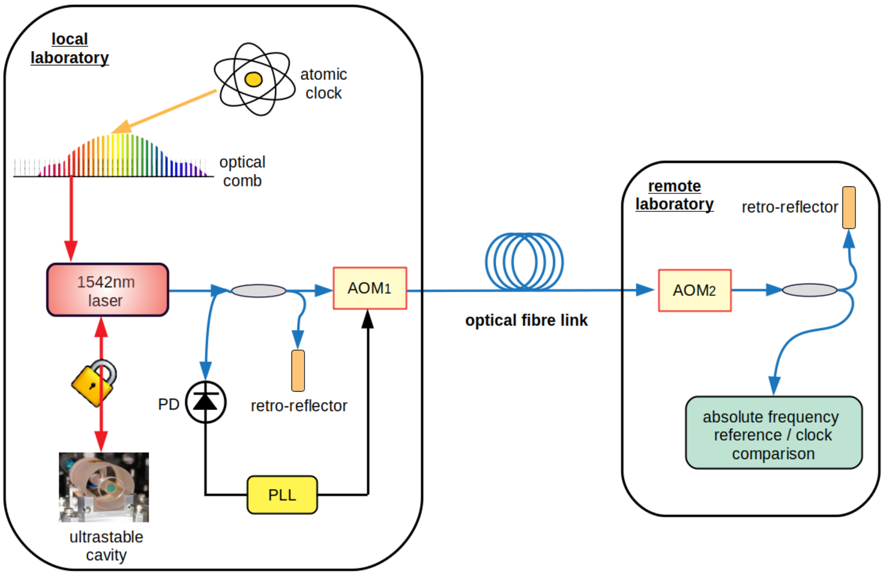

Figure 5.1: Fibre-noise cancellation technique using the round-trip signal to compensate for the noise accumulated over the fibre. The figure shows an example of optical carrier dissemination accomplished by using an ultrastable laser source that can be referenced to an atomic frequency standard by means of an optical frequency comb. The noise compensation is achieved by acting on a frequency modulator at the beginning of the fibre link. AOM: acousto-optic modulator; PD: photodiode; PLL: phase-locked loop.

the need of bypassing unidirectional amplifiers and replacing them with their bidirectional counterpart, or renting a dark fibre to develop an independent fibre link. Both solutions have been implemented, and fibre dissemination over terrestrial links longer than 1000 km has been performed [171–173]. However, considering real-life scenarios where there is no possibility of making the fibre network compatible to detect round-trip signals, one can wonder if different fibre-noise cancellation schemes could be realised. Particularly, transoceanic dissemination through submarine cables represents an attractive transfer channel that could overcome the limitation set by satellite transfer [176]. Comparison of atomic clocks located in different continents would benefit from submarine fibre-noise suppression. A Doppler cancellation scheme is not likely to be developed for transoceanic links since the existing underwater infrastructure cannot be modified. In the next section the first investigation on an alternative fibre-noise cancellation technique based on backreflection signals is presented, aiming to face extreme scenarios like submarine fibre network and at the same time to provide a simpler scheme that can be used for laboratory applications.

5.4 Fibre-noise cancellation based on backreflection signals

Laser light propagating through fibre links generates backreflection signals mainly due to Rayleigh backscattering and fibre connectors. In the conventional fibre-noise cancellation scheme those reflections are undesired since they are at the same frequency of the optical carrier and cause degradation of the round-trip signal if they are not properly distinguished. Nonetheless, we focused on a reverse approach that aims to exploit spurious reflection signals for extracting information about the noise process along the fibres instead of getting rid of them. The basic idea we investigated regards the use of Rayleigh backreflections derived from the first span of fibre links, namely the length of fibre before the first fibre amplifier, to perform a partial fibre-noise cancellation. A possible application of this method can be found by considering a submarine fibre link in view of a future transoceanic atomic clock comparison. In this case, there will be the capability of compensating for the noise of the first part of the link, i.e. the length span before the first EDFA, since after the unidirectional amplifier the backpropagating light cannot be detected. However, this will allow noise cancellation of the most noisy section of the link, from the seaside to the bottom of the ocean. There, the largest temperature variations are experienced, while the remaining part of the link can be assumed to be less perturbed.

Rayleigh backscattering in optical fibres is largely employed in different fibre-sensing technologies used to inspect the structure of optical fibre itself [177], as well to monitor oil and gas pipelines, environmental parameters and transportation systems [178]. It is an elastic scattering that arises from the collision between the laser light and local inhomogeneities in fused silica generated during the fibre fabrication [179]. As a result, the fibre medium shows fluctuations of the refraction index leading to light scattering in all directions. The loss lower limit in optical fibres is set by Rayleigh scattering, since it is an intrinsic property of the propagation medium.

In our experiment we implemented a detection scheme that makes use of Rayleigh backscattering as is similarly done in sensing techniques based on optical time domain reflectometry (OTDR). OTDR allows non-intrusive inspection of optical fibres by launching optical probe pulses using an optical circulator before the fibre under test. By measuring the time-domain backreflection signal as the light propagates a picture containing information about the fibre structure is derived. OTDR traces show a decreasing slope that indicates the power attenuation through the fibre. Different local features can be recognised by looking at discontinuities along the traces. An upward step in the reflected power is usually generated by high-reflection points such as fibre connectors, while fibre splices and bending points are represented by discontinuities with only loss of power. The information about the distance L at which each event occurs is straightforwardly obtained by converting the time delay

t to the position, $L = v_g t/2$, where v_g is the group velocity. Two events can be distinguished with spatial resolution Δx set by the pulse width T_w, $\Delta x = v_g T_\mathrm{w}/2$. Higher spatial resolution is obtained by narrowing the pulse width, although this would limit the distance at which the fibre can be probed. This is due to the fact that the pulse power decreases and thus the light cannot propagate for distances as long as for larger pulse. As a consequence, a compromise between the spatial resolution and the length of fibre that can be inspected has to be found. Another characterising parameter is the dynamic range, given by the difference between the intensity of the Rayleigh backscattering at the beginning of the OTDR trace and the noise floor. It can be improved by launching pulses of increased power, but at a high power level other phenomena such as Brillouin scattering emerge [47], limiting the dynamic range itself.

Considering the potentiality of OTDR techniques, we studied a scheme based on Rayleigh backscattering that can be used to perform time-division multiplexing along fibre links. By selecting a specific point of the fibre, it is possible to monitor its phase variations over the time. Phase information is derived by comparing the backreflection signal to the local reference, obtaining the corrections to compensate for the fibre-noise accumulated between the input of the fibre and the selected point. Below we first present the characterisation of backreflection signals through fibre links. Then we discuss a coherent detection scheme that allows the study of the phase fluctuations along the fibre.

5.4.1 Backreflection from fibre connectors and EDFAs

Preliminary investigations have been made for characterising the backscattered light from the main components that the laser light encounters travelling into fibre networks, namely fibre connectors an EDFAs. Different test measurements have been performed following the setups of fig. 5.2.

The first test bench has been thought for measuring the backscattering over a 6 km-long single-mode (SM) fibre spool (refer to fig. 5.2 a)). We used a 1542.9 nm CW-laser modulated via a Mach-Zehnder intensity modulator (MZIM) for launching optical pulses into the fibre. The CW-laser output power is about 0 dBm, which yields to a power of about −12 dBm after the MZIM. Two fibre-optic circulators (CIR_1 and CIR_2) are placed at the two ends of the fibre spool. CIR_2 is used to relaunch the light into the fibre, after it has been attenuated acting on a variable optical attenuator, by connecting ports 2 and 3. On the way back, the backreflected and relaunched light pulses that exit from port 3 of CIR_1 are detected with a photodiode. The pulse generator was set to produce pulses with 200 ns period and 50 ns width. By using a spectrum analyser we can monitor the repetition rate signal generated by the pulses impinging the photodetector. This has been done both when port 2 and port 3 of CIR_2 are connected, to see the relaunched signal as the attenuation is manually increased, and when the ports are disconnected,

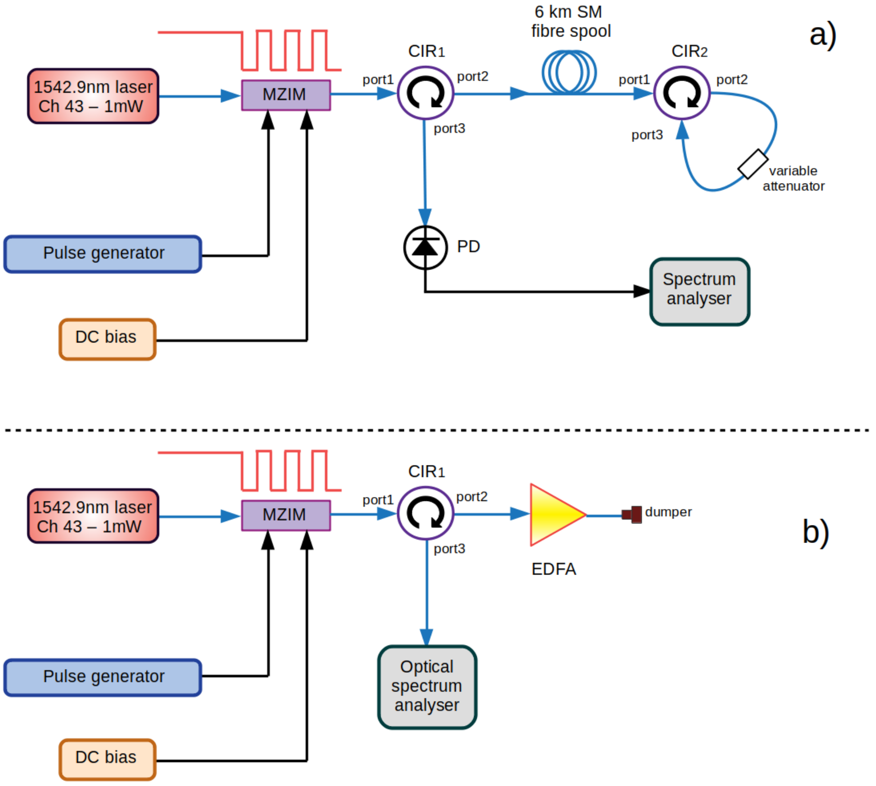

Figure 5.2: Experimental setups used to characterise the backreflection from a) a 6 km-long fibre spool and b) a fibre amplifier. MZIM: Mach-Zehnder intensity modulator; CIR: optical circulator; EDFA: erbium-doped fibre amplifier; PD: photodiode.

to measure only the backreflection signal given by the fibre. Table 5.1 reports the power measured at port 3 of CIR$_1$ as the attenuation of the re-launched light is manually increased until it is not possible to distinguish between the repetition rate signal generated by the relaunched and backreflected radiations in terms of the SNR measured on the spectrum analyser. This condition happens when the light attenuation at port 2 of CIR$_2$ is 42 dB, which corresponds to a signal of -56 dBm relaunched into the fibre spool. Therefore, 44 dB roughly quantifies the magnitude of the Rayleigh backscattered signal with respect to the power injected into the fibre spool, including also the effect of fibre connectors used in the setup.

The backreflection signal generated by using a commercial EDFA has been measured by implementing the setup of fig. 5.2 b). In this case the backscattered light is generated from the amplified spontaneous emission (ASE) of the EDFA, as well as from the isolators placed inside the amplifier and connectors. For this experiment the light after CIR$_1$ goes directly to the EDFA under test and the backreflection

attenuation @ port 2 of CIR$_2$ / dB	power @ port 3 of CIR$_1$ / dBm	repetition rate peak power @ 100 kHz RBW / dBm
10	$-22(1)$	$-31(1)$
25	$-37(1)$	$-60(1)$
31	$-43(1)$	$-75(1)$
42	$-60(1)$	$-85(1)$

Table 5.1: Characterisation of the backreflection signal from a 6 km-long fibre spool measured at port3 of CIR$_1$ (setup shown in fig. 5.2 a)).

EDFA pump current / mA	peak power @ port3 of CIR$_1$ / dBm
400	$-56.0(5)$
350	$-59.0(5)$
300	$-60.0(5)$
250	$-65.0(5)$

Table 5.2: Characterisation of the backreflection signal generated from an erbium-doped fibre amplifier measured at port3 of CIR$_1$ (setup shown in fig. 5.2 b)).

from port 3 of CIR$_1$ is measured on an OSA with 0.1 nm RBW, allowing the discrimination between the carrier signal and the pedestal generated by the ASE of the EDFA. The measurements were performed by increasing the pump laser current of the EDFA as reported in table 5.2. The magnitude of the backscattered light in this case is about $40-50$ dB lower with respect to the injected power of -16 dBm measured after the MZIM. Typically the erbium-doped fibre used as the gain medium in EDFAs has length of about $10-50$ m [180]. The backscattering coefficient S for erbium-doped fibre has been measured to be -63 dB(m^{-1}), whereas for standard SM-fibres S is lower, about $-70/-73$ dB(m^{-1}) [181]. However, usually at the ingress and output of an EDFA optical isolators are placed for avoiding backreflection from the output and stabilising the amplification process, preventing also laser operation of the amplifier. As a result, although the S coefficient is enhanced in erbium-doped fibres, its effect on the light travelling back from the input of the EDFA would be suppressed. By measuring the backreflection obtained using 20 m-long SM-fibre after the circulator instead of the EDFA we found roughly the same level of power provided by the fibre-amplifier even though the latter is affected by the mitigation due to the built-in isolators. Nevertheless, the backreflection due to the EDFA is still detectable, as can be proved by stretching the fibre-patchcord at the output of the amplifier and seeing the amplitude variations of the backreflected signal.

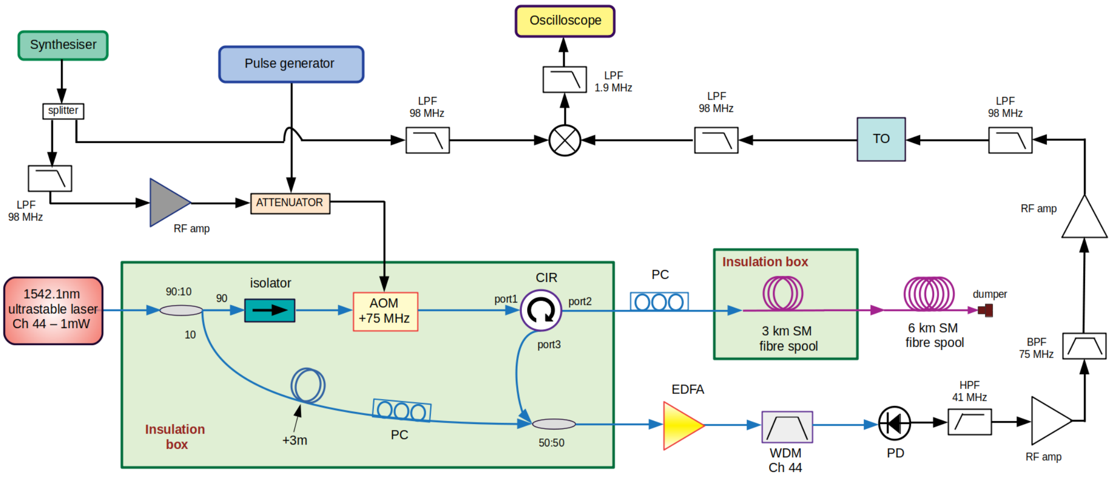

Figure 5.3: Experimental setup developed for the coherent detection of the backrefeltion signal derived from two fibre spools connected in cascade. AOM: acousto-optic modulator; CIR: optical circulator; PC: polarisation controller; EDFA: erbium-doped fibre amplifier; WDM: wavelength-division-multiplexing filter; PD: photodiode; LPF: low-pass filter; BPF: band-pass filter; TO: tracking oscillator.

5.4.2 Coherent detection of backreflected light from fibre-spools

In order to retrieve the phase-changes along fibre-spools we developed a coherent detection scheme that is similar to those employed for performing distributed acoustic sensing (DAS) [182]. Most of these sensing techniques are based on OTDR, and they allow acoustic monitoring over several tens of km using optical fibres as sensors. The most advanced DAS implementations exploit the so-called phase-sensitive OTDR (ϕ-OTDR) for achieving better performances [183] especially in terms of spatial resolution and power level of the backscattering signal [184]. The peculiarity of ϕ-OTDR is that exploits coherent detection schemes by using a narrow-linewidth laser. The backreflection signal generated in this way is the result of the coherent interaction between several backscattering centres within the pulse length. Conversely, conventional OTDR makes use of just the amplitude signal resulting from the sum of the intensities over the backscattering centres, thus it can be performed even by using laser sources with low-coherence length.

Experimental setup Figure 5.3 shows the schematic of our detection scheme. A 1542.1 nm ultrastable laser with 1 mW output power split into two arms is used to detect the beatnote between the backreflected light and the original laser radiation. One arm of the interferometer delivers the pulsed signal along the fibre-spool under test, while the second one provides the local reference signal to which the light that travels back through the circulator is beaten. The pulsed-signal is frequency-shifted by using an AOM, allowing the detection of a beatnote between the two arms at frequency equal to the AOM driving signal. Two cascaded fibre spools have been used to investigate different environmental conditions. The first one is 3 km-long and it is enclosed into an insulation box, the second one is 6 km-long, without any kind of isolation.

The pulsed laser light has been produced by acting on an AOM instead of using the aforementioned MZIM. This choice has been made because of by using the MZIM we observed a residual noise during the dead-time intervals between two consecutive pulses, whereas we expect the suppression of the signal for time greater than the temporal window needed to cover the length of the fibre spools. The noise magnitude was comparable to that of the backreflection signal and it was probably related to the fact that the MZIM was not operated at its optimum DC-bias voltage and with a high-stability DC-supplier. Possible improvements can be achieved if the DC-bias voltage is stabilised by implementing a power-control feedback loop. At the same time, temperature-control is required to avoid the drift of the transfer-function of the modulator over the time. However, in order to demonstrate a proof-of-concept scheme, we started with a simpler setup using an AOM that ensures adequate extinction ratio between the actual signal and dead-time noise. The main drawback in real-life applications is that the pulse attainable with the AOM is limited by its rise-time response, which in this case is about 70 ns. For this reason the shortest pulses can have temporal width of ∼5 µs, which corresponds to a spatial resolution of 250 m. Conversely, the MZIM does not pose limitations on the minimum pulse width achievable with the pulse generator, 10 ns, allowing higher spatial resolution, up to the 1 m-level. In the current setup the pulsed operation is achieved by using the pulse generator to drive a variable RF-attenuator that is fed with a synthesiser signal tuned at the frequency suitable for the AOM operation. An optical isolator is placed before the AOM to avoid that backreflection from the input facet of the modulator affects the beatnote signal of the interferometer. This reflection has been measured to be about 50 dB lower than the input signal. It is further suppressed by 20 dB using the isolator, which is sufficient for eliminating its contribution to the beatnote signal.

All the uncommon optical paths of the interferometer have been covered with foam rubber and enclosed in a insulation box to mitigate the effect of temperature changes and acoustic vibrations. The optical path length of the two arms is kept similar as much as possible by adding few meters of SM-fibre on the reference arm. The optical setup includes two polarisation controllers (PC), one on the reference arm, the other at port 2 of the circulator before injecting the light into the fibre spools. The first PC is used to mitigate the reflection given by the first connection between port 2 of the circulator and the fibres under test. This point is particularly critical as is the first discontinuity encountered by the laser pulses, when the light power is still not attenuated and generates the highest reflection. Once this reflection is suppressed with the PC placed inside the insulation box,

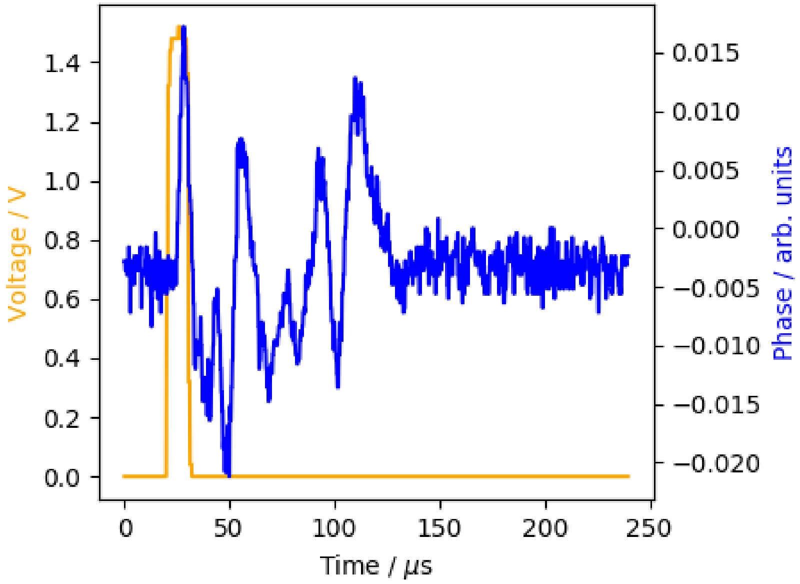

Figure 5.4: Down-converted phase-signal sample derived from the backscattering over the two fibre spools (blue trace) and pulse generator signal (yellow trace) recorded on an oscilloscope.

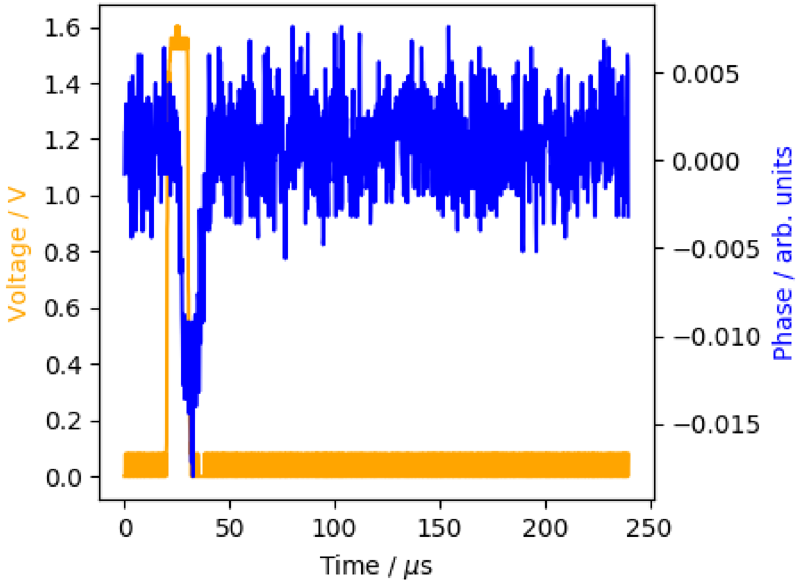

Figure 5.5: Down-converted phase-signal sample derived when the fibre spools are not connected (blue trace) and pulse generator signal (yellow trace) recorded on an oscilloscope.

then the second PC connected just before the fibre spools allows the optimisation of the signal belonging to a specific point along the laser pulses' path.

The beatnote signal between the two arms is amplified by using an EDFA and then filtered with a telecom wavelength-division-multiplexing (WDM) filter centred at the 44th channel of the ITU grid. The detection of the phase-variations is accomplished by down-converting to DC the beatnote signal and measuring it on an oscilloscope after low-pass filtering at 1.9 MHz. Before the down-conversion the beatnote is filtered using BPFs after each amplification stage. The beatnote signal's power is amplified up to the level at which the last amplifier is power-saturated, in order to be insensitive to amplitude fluctuations on the down-converted signal. Furthermore, a clean-up tracking oscillator (TO) with a 200 kHz BW is used to narrow the filtering bandwidth.

Results First investigations have been performed to prove the sensitivity of this technique to external noise sources. We produce laser pulses of 300 µs duration, which is more than twice the time required to cover the length of the combined fibre spools. The pulse width is 10 µs, corresponding to 500 m spatial resolution. We measured the down-converted beatnote signal on an oscilloscope with sampling rate of 500 $\mathrm{kSa\,s^{-1}}$, leading to time resolution of 2 µs. Figure 5.4 shows the typical down-conveted signal we obtained from a single pulse that probes the two fibre spools (blue trace) and the pulse signal provided by the pulse generator (yellow trace). The down-converted signal has $\sim$6 µs of delay with respect to the starting time of the pulse generator signal. This is due to the propagation time of the acoustic wave throughout the AOM, which produces the frequency-shifted signal at the modulator output. In fig. 5.5 the same traces are plotted to provide an example of the residual backreflection obtained when the two fibre spools are disconnected. As can be seen, there is still a large bump at the start of the down-converted signal generated from the reflection from the first fibre connector. It lasts for a duration equal to the pulse width. This measurement sample has been chosen to highlight the effect of the first discontinuity along the light path when its contribution is not properly suppressed.

During the acquisition time acoustic perturbations are induced by tapping on one of the two fibre spools. We selected two points from the backrefletion trace, one for each fibre spool, and analysed what happens in terms of frequency response over the time measurement. The results are presented by means of the spectrograms in fig. 5.6 and fig. 5.7. In the first case the perturbation has been applied to the 6 km fibre spool for measuring time t greater than 12 s. Its effect can be seen from fig. 5.6 (b), where the point monitored belongs to the 6 km fibre, while the point selected from the 3 km fibre is not affected by the perturbation as we expected (see fig. 5.6 (a)). Conversely, when the perturbation is applied to the first fibre spool the effect is visible on both the spectrograms, as is highlighted in fig. 5.7 for $t > 7$ s. Furthermore, fig. 5.7 (a) shows how the insulation box enhanced the

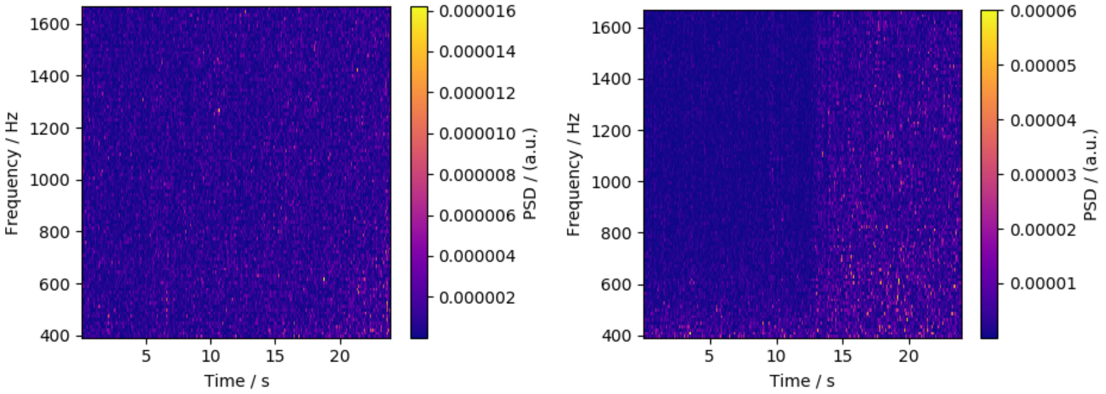

(a) **(b)**

Figure 5.6: Frequency response over the measurement time of two points that belong to the 3 km (a) and 6 km (b) fibre spools. Acoustic perturbation are induced on the 6 km fibre spool for measurement time t greater than 12 s.

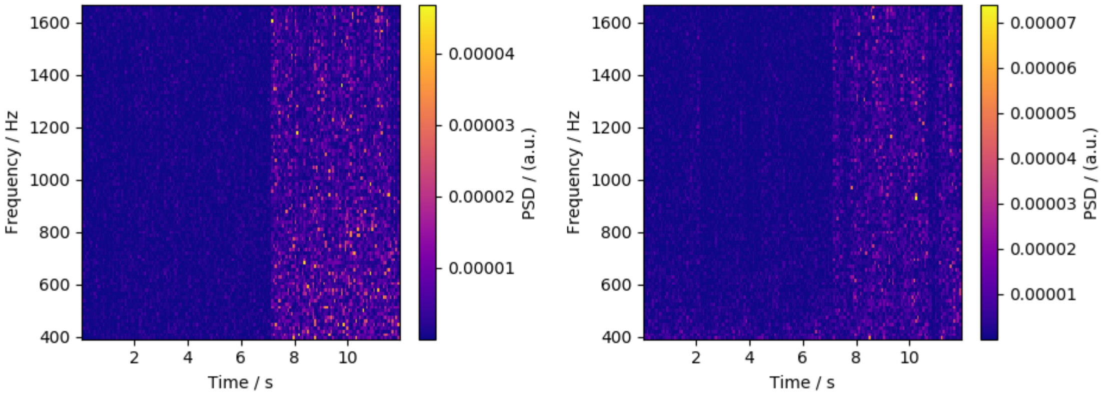

(a) **(b)**

Figure 5.7: Frequency response over the measurement time of two points that belong to the 3 km (a) and 6 km (b) fibre spools. Acoustic perturbation are induced on the 3 km fibre spool for measurement time t greater than 7 s.

noise due to acoustic vibrations on the 3 km fibre spool. Therefore, with this set of measurements we observed a qualitative demonstration of how the backreflection signal can provide information about the noise processes experienced along optical fibres.

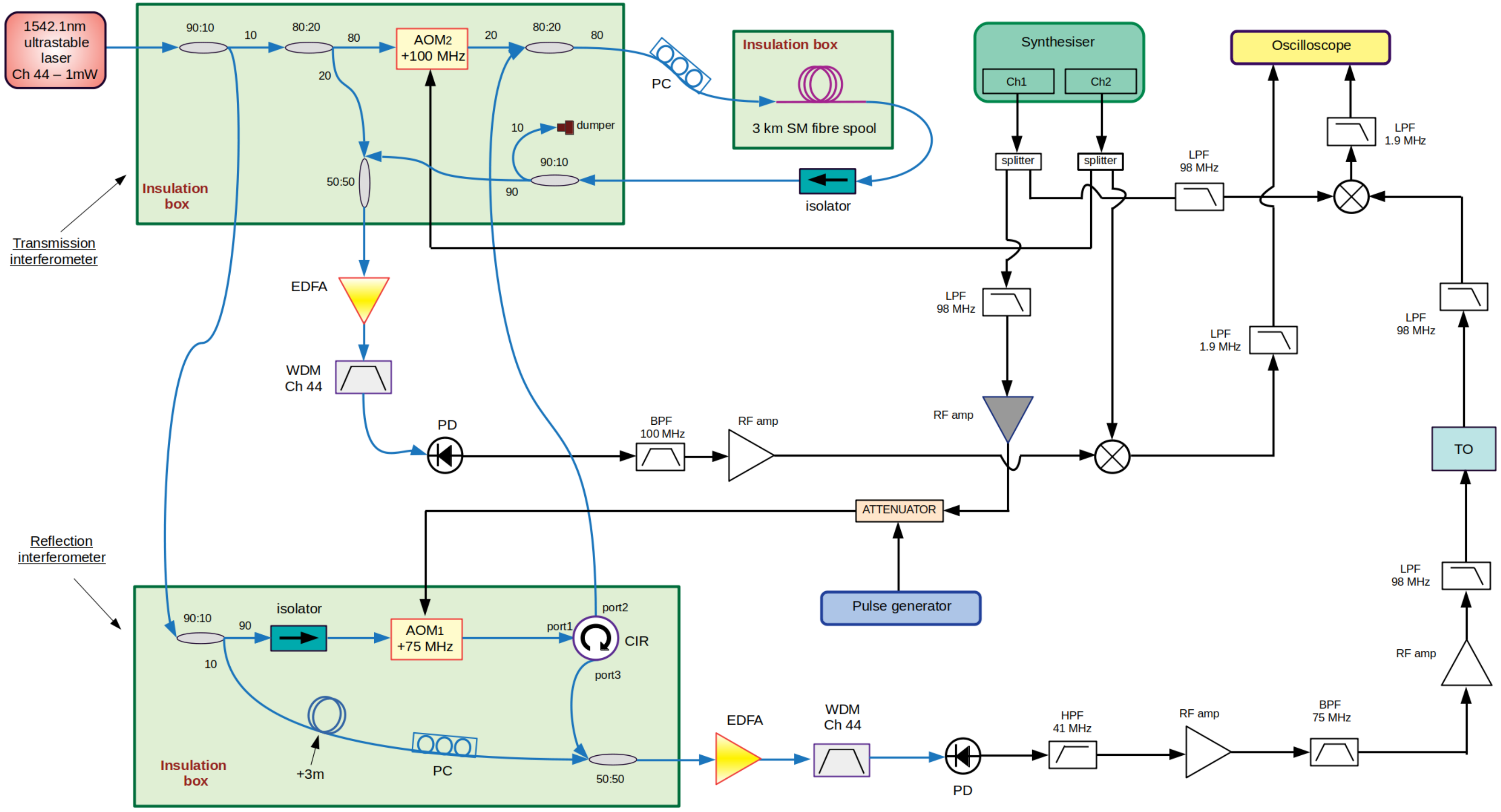

Figure 5.8: Experimental setup developed for comparing the backrefeltion and transmission signals derived from a 3 km fibre spool. AOM: acousto-optic modulator; CIR: optical circulator; PC: polarisation controller; EDFA: erbium-doped fibre amplifier; WDM: wavelength-division-multiplexing filter; PD: photodiode; LPF: low-pass filter; BPF: band-pass filter; TO: tracking oscillator.

5.4.3 Comparison between transmitted and backreflected light along fibre-pools

In order to better inspect the backreflection signal properties, we modified the optical and electronic setups for measuring at the same time the reflected and transmitted light along the optical fibres. Thanks to the comparison between those two signals we can assess how faithfully the backreflection can retrieve the phase-changes. For this measurement we used the 3 km fibre spool enclosed in the insulation box. In this way we start with considering a simple configuration, focusing on slow phase variations while high-frequency noise sources are mitigated.

Experimental setup The measurement detection scheme is shown in fig. 5.8. Before being used for the reflection interferometer described in section 5.4.2, the CW-laser is split for building the optical setup for the transmission signal's detection. 1 mW of the CW-laser light is still enough for detecting both the transmitted and reflected signals. Then, for having a CW-signal at the end of the fibre spool with different frequency from the pulsed one (generated via AOM_1 in fig. 5.8), another AOM is used (AOM_2 in fig. 5.8). The light from the AOM_2 output is recombined with that exiting from port 2 of the circulator, thus the CW-light and the pulsed-light are injected together into the fibre spool. Afterwards, the transmitted radiation at the end of the fibre spool passes through an optical isolator for avoiding unwanted backreflection generated from points after the fibre under test and it is beaten with the original laser light for generating the signal of the transmission interferometer. All the uncommon optical path are also in this case insulated as has been done for the reflection interferometer. The beatnote signal is then processed similarly to the backreflection signal for detecting a down-converted to DC signal. The principal difference is that no tracking oscillators have been used, since the transmission signal filtering is not as demanding as for the backreflection detection.

Results The information on the phase fluctuations inferred from the transmission signal is the result of the integrated noise over the whole fibre-spool, since the transmitted signal is obtained by using CW-laser light. Therefore, for performing a proper comparison the temporal width of the laser pulses used in the reflection interferometer has been chosen in order to cover the entire fibre spool length with a single pulse, which approximates the case of CW probe radiation. For this reason the pulse width is set to 15 µs, whit a pulse period of 100 µs that allows large separations between the end and beginning of consecutive traces. Transmission and reflection data are acquired simultaneously with an oscilloscope at 1.250 $\mathrm{MSa\,s^{-1}}$ sampling rate (corresponding to time resolution of 0.8 µs).

Figure 5.9 and fig. 5.10 show the comparison between the reflection (blue trace) and transmission (yellow trace) phase data taken at different times from the same

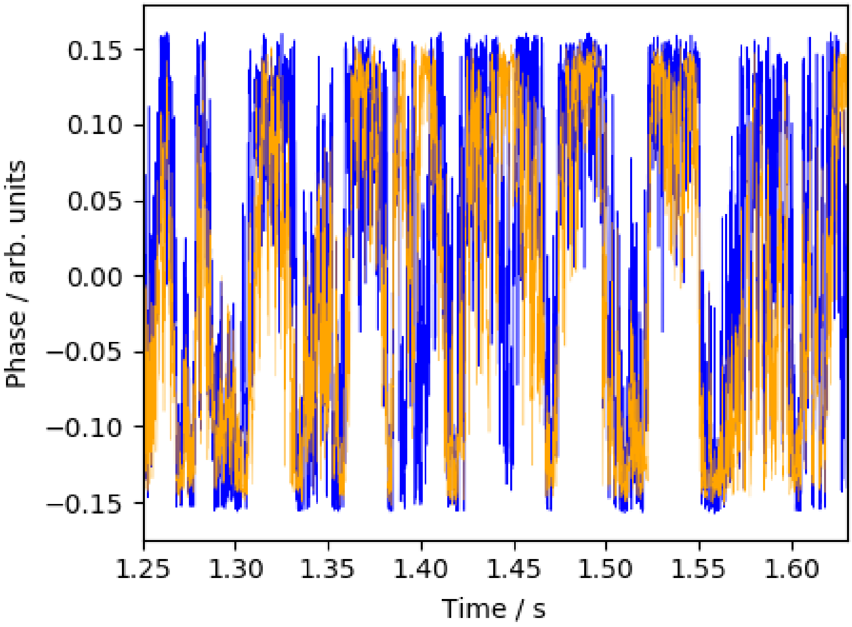

Figure 5.9: Comparison between the backreflection (blue trace) and transmission (yellow trace) signals from data acquired with the oscilloscope. The two signal show high-correlation on the phase information.

measurement. The two traces are scaled for having a comparison at the same amplitude level. As can be seen in fig. 5.9, initially the correlation between the two signals is high, but during the measurement a complete anti-correlation is experienced as shown in fig. 5.10. The transition between correlation and anti-correlation happens at timescales of few seconds and it has been noticed over several measurements. One possible cause of this behaviour can be associated to the different kind of laser signal used in the two interferometers. The transmission signal is obtained by using CW-laser light, which continuously probe the fibres. The reflected signal is related to pulsed laser light that carries information about the fibre noise only for a period of time corresponding to the pulse width, while during the dead-times between two pulses no information is provided. Thus there is the possibility that some high-frequency noise source detected by the CW-laser light is not experienced in the same way by the pulsed laser light. We tried to provide further insulation both to the fibre spool under test and to the fibres used in the interferometer. In this way the effect of noise sources that cannot be extrapolated in the same way by the reflection and transmission signals can be mitigated. We covered the fibres with thermal gel packs that guarantee a better thermal insulation. However, measurements performed after the thermal stabilisation of the setup did not show any change regarding the sign inversion of the correlation. Further investigations

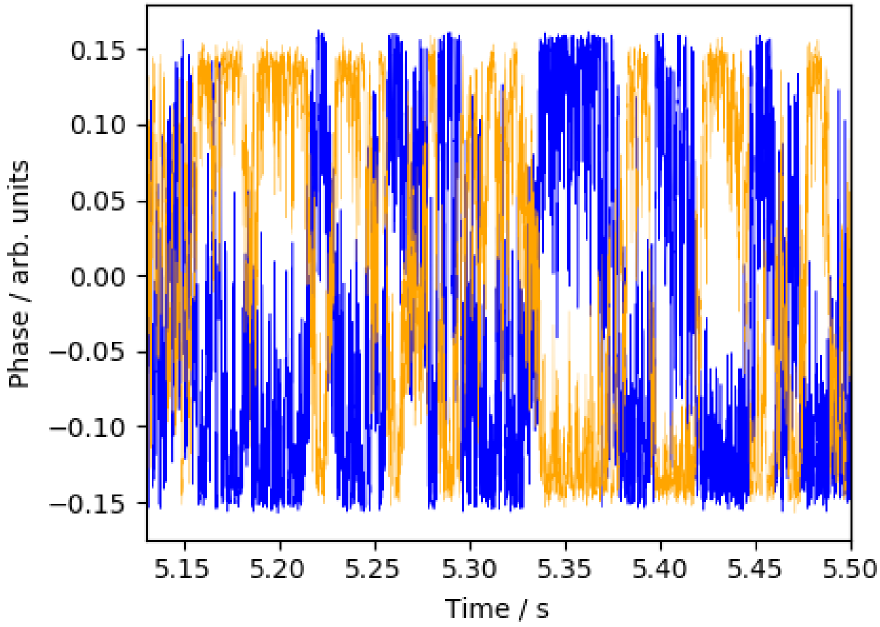

Figure 5.10: Comparison between the backreflection (blue trace) and transmission (yellow trace) signals from data acquired with the oscilloscope. A degradation of the correlation is noticed at a few seconds timescale, which yields to a complete anti-correlation between the two signals.

have yet to be done for understanding this process, but the preliminary results we obtained are promising with a view to using the backreflection signal to partially cancel the phase-noise accumulated over fibre links.

5.5 Chromatic dispersion compensation of mode-locked laser pulses

Alternatively to producing optical pulses via modulation of CW-lasers, optical frequency combs (or MLLs) can be used to inject sub-ps optical pulses into fibre links. As mentioned in section 5.2, accurate microwave and optical frequency transfer, as well as time information transfer, have been demonstrated over fibre spools and installed fibre links exploiting optical comb pulses [32]. One of the main issues encountered when fs-width optical pulses travel along several tens of km-fibre links is the pulse-broadening due to the chromatic dispersion inside the fibre medium.

Considering the scheme we presented in section 5.4.2, if the modulated CW-laser is replaced with optical combs (or MLLs), then the chromatic dispersion can be used as an additional parameter to select a specific point to be monitored along

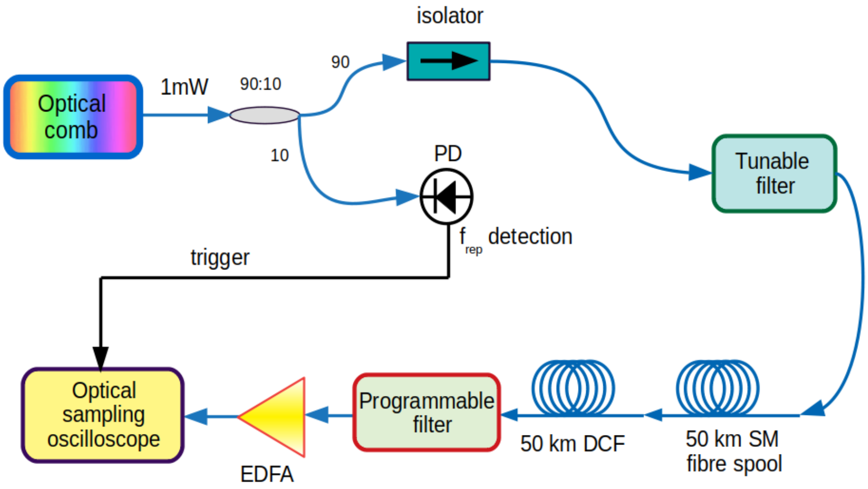

Figure 5.11: Experimental setup developed for studying the chromatic dispersion compensation of frequency comb pulses that travel through a 50 km-long fibre spool. PD: photodiode; f_{rep} = comb repetition rate; DCF: dispersion-compensating fibre; EDFA: erbium-doped fibre amplifier.

the fibre. By implementing a proper control of the dispersion compensation the pulse shape can be recovered only for a specific point at a desired length of fibre, suppressing unwanted information from other points of the fibre link. Below the experimental characterisation of the dispersion compensation of optical comb pulses launched into a fibre spool is presented, which has been performed at the Optoelectronic Research Centre of the University of Southampton (UK).

Chromatic dispersion is related to the refractive index n dependence on the frequency ω, and its effect is usually quantified by applying a Taylor-series expansion to the propagation constant β around the central frequency of the pulse ω_0 [47]:

$$\beta(\omega) = n(\omega)\frac{\omega}{c} = \beta_0 + \beta_1(\omega-\omega_0) + \frac{1}{2}\beta_2(\omega-\omega_0)^2 + ..., \tag{5.1}$$

being $\beta_m = (d^m\beta/d\omega^m)_{\omega=\omega_0}$. The dispersion parameter D is linked to the coefficient β_2 by the relation

$$D = \frac{d\beta_1}{d\lambda} = -\frac{2\pi c}{\lambda^2}\beta_2 \approx \frac{\lambda}{c}\frac{d^2n}{d\lambda^2}. \tag{5.2}$$

The value of D at 1550 nm is about 17 ps/(nm km). The dispersion effect is negligible for CW-laser of few Hz-linewidth, while for optical frequency combs it becomes critical because of the inversely proportional relation that holds between the pulse width and the gain bandwidth of the laser (see section 2.1). Typical values of MLLs' gain bandwidth are in the order of several tens of nm, yielding to pulse

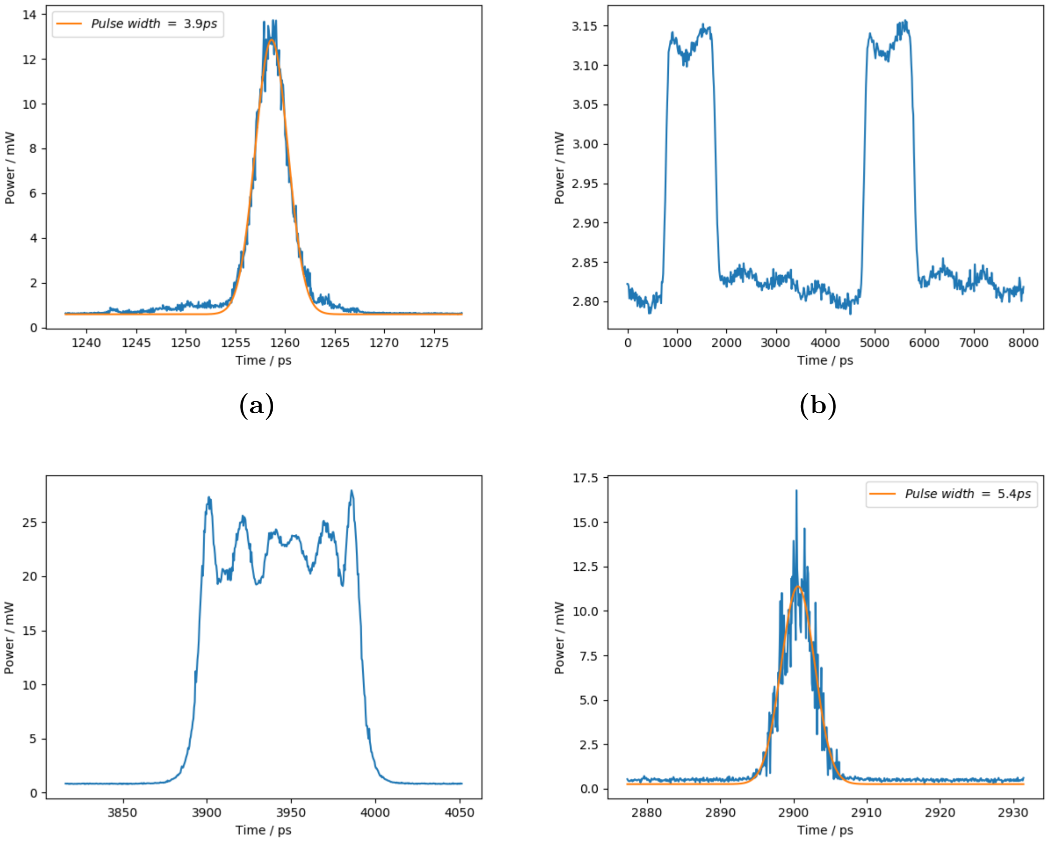

(a) (b)

(c) (d)

Figure 5.12: Optical comb pulses pre-filtered with a 6 nm BW. Referring to the setup of fig. 5.11, measurements are taken before the light is injected into the fibre spools (a), after the 50 km SM fibre spool (b), after the 50 km DCF (c) and at the programmable optical filter output (d). The programmable filter is set to compensate the chromatic dispersion for a length of 970 m. Gaussian fits are been used to infer the pulse width (yellow curves).

broadening at the ns level over few km of optical fibres. For facing this problem, dispersion-compensating fibres (DCFs) are employed. The aim of the experiment we performed was the characterisation of how well the pulse shape of optical comb pulses that travel over several km-long optical fibres can be retrieved by using DCFs modules.

Experimental setup Figure 5.11 shows the setup used for measuring the optical pulses of a commercial erbium-fibre comb that are broadened over a 50 km-long SM fibre spool. The optical comb output is centred at 1.55 µm and 100 nm-wide, with output power of about 1 mW. Before injecting the comb light into the fibre

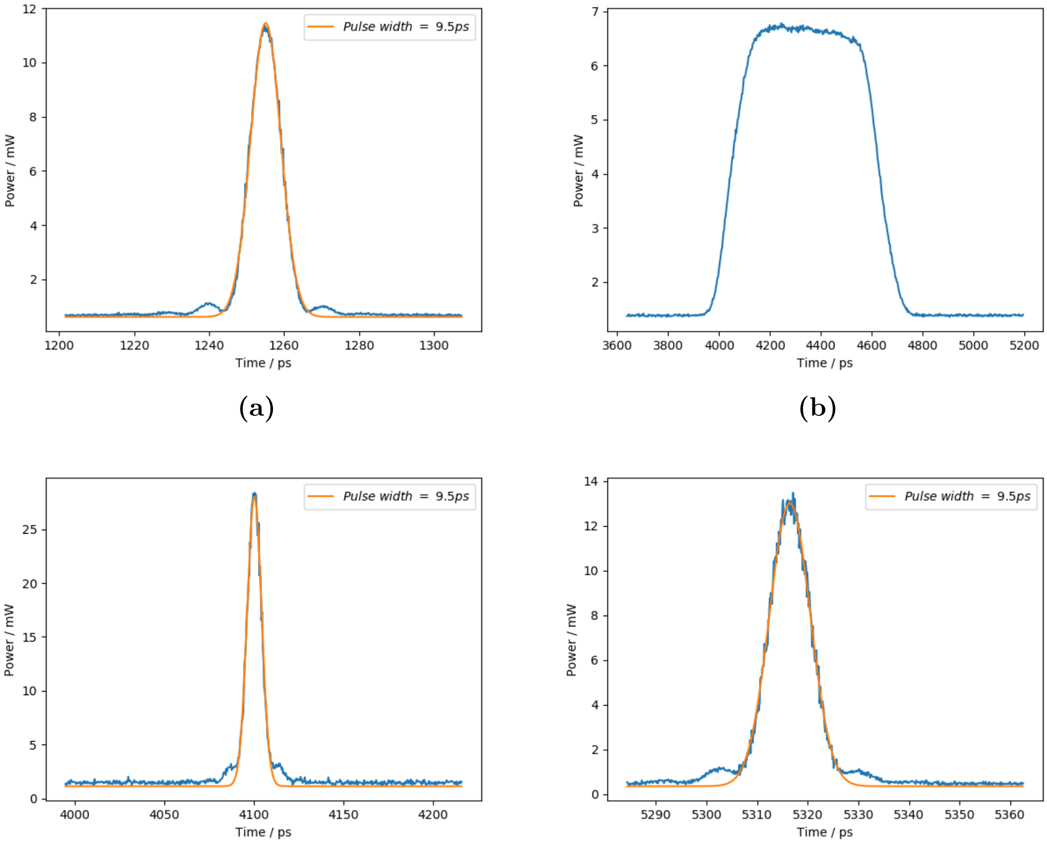

(a) (b)

(c) (d)

Figure 5.13: Optical comb pulses pre-filtered with a 0.7 nm BW. Referring to the setup of fig. 5.11, measurements are taken before the light is injected into the fibre spools (a), after the 50 km SM fibre spool (b), after the 50 km DCF (c) and at the programmable optical filter output (d). The programmable filter is set to compensate the chromatic dispersion for a length of 100 m. Gaussian fits are been used to infer the pulse width (yellow curves).

spool an optical tunable filter is used for narrowing the optical BW of the comb output. An optical sampling oscilloscope is used for measuring the optical pulses. The signal used to trigger the oscilloscope is generated by detecting the comb repetition rate f_{rep} on a photodiode. The pulse broadening is coarsely corrected by adding a 50 km-long commercial DCF, which has negative dispersion of -828 ps/nm at 1542 nm. Additional fine-tuning of the pulse shape is applied by using a programmable optical filter. In this way the dispersion can be compensated at the equivalent level achieved by using DCFs whose length can be varied with precision better than 10 m. Finally the comb pulses have been amplified by means of an EDFA (which has 30 nm BW) to be properly detected on the optical sampling

filtering BW / nm	**pulse width after the tunable filter / ps**	**pulse width after the 50 km DCF / ps**	**pulse width after the programmable filter / ps**	**additional DCF length / m**
0.7	9.5	9.5	9.5	100
1.7	5.6	27.0	6.0	1100
3	5.5	/	5.5	1100
6	3.9	/	5.4	970
10	3.8	/	8.2	1000
20	3.6	/	4.8	1030

Table 5.3: Characterisation of the recovering of the pulse comb width after broadening over 50 km fibre spool by means of DCF modules. The comb output is filtered at different BW values before being injected into the fibre spool.

oscilloscope.

Results Measurements of the pulse width on the optical sampling oscilloscope have been taken at different value of the tunable filter's BW. As a consequence, the initial pulse width has been increased of few ps as the BW became narrower. The pulse shape has been recorded at four different points of the setup, namely before being injected into the fibre spools, after the 50 km SM fibre spool, after the 50 km DCF and at the programmable optical filter output. Figure 5.12 and fig. 5.13 report examples of these measurements, each one showing the pulse width at the four monitored points. For those measurements filtering BW of 6 nm and 0.7 nm have been applied (fig. 5.12 and fig. 5.13 respectively). Gaussian fits have been used to infer the pulse width and they are showed as well in the figures. The fine-tuning optical filter has been programmed in order to find the best length of fibre that corresponds to recover as well as possible the original pulse width. Considering a filtering BW of 6 nm, we observed a pulse broadening of about 100 ps at the end of the 50 km DCF. Taking into account the aforementioned dispersion parameter D, then roughly 1 km of additional DCF is needed to match the initial pulse width. Therefore, we searched the optimum value by varying the programmable filter around this length value. As can be seen from fig. 5.12, the 50 km DCF is not sufficient to recover the 3.9 ps pulse width and fine-tuning is needed to get close to the initial value. On the contrary, with a narrower filtering BW of 0.7 nm as in fig. 5.13 the reshaping of the 9.5 ps pulse width is already achieved with the commercial DCF.

In table 5.3 the results obtained for different filtering BW are listed, comparing the initial pulse width before the fibre spools to the one measured after applying DCF modules. The comparison between these measurements shows that the use of the fine-tuning filter to recover the original pulse width is required for filter's BW greater than 1 nm, while for lower BW values commercial DCFs can perform the pulse reshaping at adequate levels. Therefore, the characterisation here presented shows that for using optical frequency comb pulses over several km-long fibre links a compromise between choosing adequate pulse width and exploiting a commercial-based dispersion compensation (i.e. if special programmable filters are not available) has to be found.

5.6 Summary

An alternative scheme for fibre stabilisation using spurious reflections generated along fibre links rather than intentionally generated with retro-reflectors has been investigated.

The characterisation of the level of spurious backscatter signals, arising from interconnections and Rayleigh scattering, has been tested. Laser pulsed signals were launched into fibre spools by modulating a 1542 nm CW-laser using an AOM. With regards to the backscattered light, different cases were investigated. Reflections due to fibre connectors and EDFAs were measured. In this way we could understand the main contributions to the detected signal.

A coherent detection scheme has been developed, which allowed the study of the phase fluctuations of the laser light once it travelled back and forth over the fibre. By comparing the backscattered light to that transmitted over a 3 km fibre spool the correlation between the two has been analysed. From preliminary measurements we can assess that the backreflection signal can retrieve the phase changes experienced through the fibre spool. However, a sign inversion of the correlation during the experiments has been observed, which needs to be further investigated. These experiments pave the way to frequency transfer techniques based on backscattered light, which could be helpful in real-life applications when a modification of the telecom fibre infrastructure cannot be realised, providing also the advantages of a simpler configuration.

In addition, experiments have been carried out for studying the possibility of using optical frequency combs (or MLLs) instead of a modulated CW-laser for launching sub-ps-width pulses into the fibres. For this purpose we characterised the effect of chromatic dispersion on optical comb pulses that travelled a 50 km-long fibre spool and how the initial pulse shape can be recovered using dispersion-compensating modules.

Chapter 6

Conclusion

The work presented in this thesis reports on the contributions of my Ph.D. activity to the advancements in optical frequency metrology. The consolidation of the reliability of optical frequencies' traceability would benefit not only fundamental metrology but also a number of other fields of research and many sectors of our society. The work has been carried out at the Italian National Metrology Institute, INRiM, in the Quantum Metrology and Nanotechnology division, and at the UK's National Measurement Institute, NPL, in the Time and Frequency division of the Quantum Metrology Institute.

Since optical atomic clocks have been demonstrated to reach accuracy and stability performances in the 10^{-18} regime, which outperform those of the current Cs primary microwave standards, many efforts have been dedicated to measure and characterise optical frequency standards in view of a future redefinition of the SI unit of second. Among the technologies that make possible the measurements and comparison of optical clocks, a fundamental role is played by optical frequency combs and optical fibre-based time and frequency dissemination techniques. Optical combs allow both the measurement of absolute frequencies with respect to the microwave domain, i.e. establishing a link to the SI second, and optical frequency ratio measurements, necessary for the direct comparison of optical clocks. Optical fibre links provide the adequate infrastructure to compare atomic clocks between remote facilities. With regards to the above illustrated aspects of optical frequency metrology, a summary of the results obtained during my Ph.D. is reported below.

Consolidation of optical traceability At INRiM we performed the spectral purity transfer from the 1156 nm ultrastable laser used for the interrogation of the ^{171}Yb clock transition to a 1542 nm laser by using our multi-branch erbium-fibre comb. Different noise contributions that affect the spectral transfer have been characterised, concerning the electronic and optical setups developed. We demonstrated that spectral transfer with $5 \times 10^{-17} (\tau/\mathrm{s})^{-1/2}$ residual instability and 3×10^{-19} accuracy can be achieved with such a system. The results are published in [111].

The ultimate limit on the spectral transfer is set by the residual noise due to the multi-branch comb configuration. Its contribution has been evaluated by measuring the 1156 nm laser and its 578 nm second-harmonic on the $f-2f$ and 578 nm branches of the comb, while the inter-branch noise between the $f-2f$ and 1.56 µm branches has been quantified by measuring the same 1542 nm laser on the two. This characterisation could be generalised for similar multi-branch erbium-fibre systems, putting an upper limit to the performances of such kind of combs. The results showed that we can use our multi-branch comb to disseminate the ^{171}Yb optical clock over fibre links by spectral transfer to a 1542 nm telecom laser and to generate the 698 nm ultrastable clock laser for the ^{87}Sr optical clock that is under development [113].

Optical frequency measurements Two absolute optical frequency measurements of the ^{171}Yb optical lattice clock operating at INRiM have been performed. In the first measurement the ^{171}Yb clock has been compared to the Cs primary standard ITCsF2 that is maintained at INRiM [91], achieving an uncertainty of 5.9×10^{-16} limited by the Cs fountain clock. The second measurement has been performed by exploiting a link to the International Atomic Time (TAI), achieving an ultimate uncertainty of 2.6×10^{-16} limited by the satellite-based transfer. For both the two measurements we used the erbium-fibre comb to bridge the optical to the microwave domain. The results are published in [34] and [35].

Furthermore, a comparison between the ^{171}Yb optical clock and a transportable ^{87}Sr optical clock developed at PTB has been performed in the context of the ITOC project. The comparison has been made by using the optical comb as a transfer oscillator, allowing the evaluation of the ^{171}Yb/^{87}Sr frequency ratio without being limited by the Cs primary standard. The ratio has been measured with an ultimate uncertainty of 2.8×10^{-16} and it is published in [115].

These optical frequency measurements represent an important contribution for consolidating the ^{171}Yb-based frequency standard as a secondary representation of the second.

Fibre-link transfer At NPL we studied the possibility of implementing an alternative technique for stabilising fibre links used to transfer time and frequency signals. We investigated spurious backreflection signals generated along optical fibres, due to Rayleigh backscattering and reflections from fibre connectors and EDFAs. This technique would be useful in real-life scenario where there is no possibility of modifying the existent fibre network to implement conventional phase stabilisation based on using retro-reflectors at the end of the fibre links. We compared the reflected and the transmitted signals along fibre spools by launching pulses generated from a modulated CW-laser and implementing a coherent detection scheme, in order to assess if through backreflection the phase-noise experienced along optical fibres can be retrieved. The preliminary results obtained show that the reflected signal is correlated to the transmitted one, even if further investigation on sign inversion of the correlation is required. Furthermore, the effect of chromatic dispersion on laser pulses with sub-ps width that travel along several km-long fibre has been characterised in view of using optical comb sources instead of modulated CW-lasers for launching laser pulses into fibre links.

Bibliography

[1] “Documents Concerning the New Definition of the Metre”. In: *Metrologia* 19.4 (1984), pp. 163–178. DOI: 10.1088/0026-1394/19/4/004 (cit. on p. 1).

[2] L. Essen and J. V. L. Parry. “An Atomic Standard of Frequency and Time Interval: A Caesium Resonator”. In: *Nature* 176.4476 (1955), pp. 280–282. DOI: 10.1038/176280a0 (cit. on p. 2).

[3] R Wynands and S Weyers. “Atomic fountain clocks”. In: *Metrologia* 42.3 (2005), S64–S79. DOI: 10.1088/0026-1394/42/3/s08 (cit. on p. 2).

[4] https://www.bipm.org/utils/common/pdf/CGPM-2018/26th-CGPM-Resolutions.pdf (cit. on p. 2).

[5] Andrew D. Ludlow, Martin M. Boyd, Jun Ye, E. Peik, and P. O. Schmidt. “Optical atomic clocks”. In: *Reviews of Modern Physics* 87.2 (2015), pp. 637–701. DOI: 10.1103/revmodphys.87.637 (cit. on p. 3).

[6] F. Diedrich, J. C. Bergquist, Wayne M. Itano, and D. J. Wineland. “Laser Cooling to the Zero-Point Energy of Motion”. In: *Physical Review Letters* 62.4 (1989), pp. 403–406. DOI: 10.1103/physrevlett.62.403 (cit. on p. 3).

[7] Hidetoshi Katori, Masao Takamoto, V. G. Pal’chikov, and V. D. Ovsiannikov. “Ultrastable Optical Clock with Neutral Atoms in an Engineered Light Shift Trap”. In: *Physical Review Letters* 91.17 (2003). DOI: 10.1103/physrevlett.91.173005 (cit. on p. 3).

[8] Ichiro Ushijima, Masao Takamoto, Manoj Das, Takuya Ohkubo, and Hidetoshi Katori. “Cryogenic optical lattice clocks”. In: *Nature Photonics* 9.3 (2015), pp. 185–189. DOI: 10.1038/nphoton.2015.5 (cit. on p. 3).

[9] W. F. McGrew, X. Zhang, H. Leopardi, R. J. Fasano, D. Nicolodi, K. Beloy, J. Yao, J. A. Sherman, S. A. Schäffer, J. Savory, R. C. Brown, S. Römisch, C. W. Oates, T. E. Parker, T. M. Fortier, and A. D. Ludlow. “Towards the optical second: verifying optical clocks at the SI limit”. In: *Optica* 6.4 (2019), p. 448. DOI: 10.1364/optica.6.000448 (cit. on pp. 3, 70, 71, 73).

[10] Christian Sanner, Nils Huntemann, Richard Lange, Christian Tamm, Ekkehard Peik, Marianna S. Safronova, and Sergey G. Porsev. "Optical clock comparison for Lorentz symmetry testing". In: *Nature* 567.7747 (2019), pp. 204–208. DOI: `10.1038/s41586-019-0972-2` (cit. on p. 3).

[11] Fritz Riehle, Patrick Gill, Felicitas Arias, and Lennart Robertsson. "The CIPM list of recommended frequency standard values: guidelines and procedures". In: *Metrologia* 55.2 (2018), pp. 188–200. DOI: `10.1088/1681-7575/aaa302` (cit. on p. 3).

[12] Scott A. Diddams. "The evolving optical frequency comb [Invited]". In: *Journal of the Optical Society of America B* 27.11 (2010), B51. DOI: `10.1364/josab.27.000b51` (cit. on p. 3).

[13] Fritz Riehle. "Optical clock networks". In: *Nature Photonics* 11.1 (2017), pp. 25–31. DOI: `10.1038/nphoton.2016.235` (cit. on p. 3).

[14] V. P. Chebotayev, V. G. Goldort, V. M. Klementyev, M. V. Nikitin, B. A. Timchenko, and V. F. Zakharyash. "Development of an optical time scale". In: *Applied Physics B Photophysics and Laser Chemistry* 29.1 (1982), pp. 63–65. DOI: `10.1007/bf00694370` (cit. on p. 3).

[15] C.O. Weiss, G. Kramer, B. Lipphardt, and E. Garcia. "Frequency measurement of a CH_4 hyperfine line at 88 THz - 'optical clock'". In: *IEEE Journal of Quantum Electronics* 24.10 (1988), pp. 1970–1972. DOI: `10.1109/3.8528` (cit. on p. 3).

[16] H. Schnatz, B. Lipphardt, J. Helmcke, F. Riehle, and G. Zinner. "First Phase-Coherent Frequency Measurement of Visible Radiation". In: *Physical Review Letters* 76.1 (1996), pp. 18–21. DOI: `10.1103/physrevlett.76.18` (cit. on p. 3).

[17] J. E. Bernard, A. A. Madej, L. Marmet, B. G. Whitford, K. J. Siemsen, and S. Cundy. "Cs-Based Frequency Measurement of a Single, Trapped Ion Transition in the Visible Region of the Spectrum". In: *Physical Review Letters* 82.16 (1999), pp. 3228–3231. DOI: `10.1103/physrevlett.82.3228` (cit. on p. 3).

[18] H. R. Telle, D. Meschede, and T. W. Hänsch. "Realization of a new concept for visible frequency division: phase locking of harmonic and sum frequencies". In: *Optics Letters* 15.10 (1990), p. 532. DOI: `10.1364/ol.15.000532` (cit. on p. 4).

[19] K. Imai, M. Kourogi, and M. Ohtsu. "30-THz span optical frequency comb generation by self-phase modulation in an optical fiber". In: *IEEE Journal of Quantum Electronics* 34.1 (1998), pp. 54–60. DOI: `10.1109/3.655007` (cit. on p. 4).

[20] Th. Udem, J. Reichert, R. Holzwarth, and T. W. Hänsch. "Accurate measurement of large optical frequency differences with a mode-locked laser". In: *Optics Letters* 24.13 (1999), p. 881. DOI: `10.1364/ol.24.000881` (cit. on pp. 4, 17).

[21] Th. Udem, J. Reichert, R. Holzwarth, and T. W. Hänsch. "Absolute Optical Frequency Measurement of the Cesium D_1 Line with a Mode-Locked Laser". In: *Physical Review Letters* 82.18 (1999), pp. 3568–3571. DOI: `10.1103/physrevlett.82.3568` (cit. on pp. 4, 17).

[22] John L. Hall. "Nobel Lecture: Defining and measuring optical frequencies". In: *Reviews of Modern Physics* 78.4 (2006), pp. 1279–1295. DOI: `10.1103/revmodphys.78.1279` (cit. on p. 4).

[23] Theodor W. Hänsch. "Nobel Lecture: Passion for precision". In: *Reviews of Modern Physics* 78.4 (2006), pp. 1297–1309. DOI: `10.1103/revmodphys.78.1297` (cit. on p. 4).

[24] Long-Sheng Ma, Zhiyi Bi, Albrecht Bartels, Kyoungsik Kim, Lennart Robertsson, Massimo Zucco, Robert S. Windeler, Guido Wilpers, Chris Oates, Leo Hollberg, and Scott A. Diddams. "Frequency Uncertainty for Optically Referenced Femtosecond Laser Frequency Combs". In: *IEEE Journal of Quantum Electronics* 43.2 (2007), pp. 139–146. DOI: `10.1109/jqe.2006.886836` (cit. on p. 4).

[25] L. E. Hargrove, R. L. Fork, and M. A. Pollack. "Locking of He-Ne Laser Modes Induced by Synchronous Intracavity Modulation". In: *Applied Physics Letters* 5.1 (1964), pp. 4–5. DOI: `10.1063/1.1754025` (cit. on p. 4).

[26] Jinendra K. Ranka, Robert S. Windeler, and Andrew J. Stentz. "Visible continuum generation in air–silica microstructure optical fibers with anomalous dispersion at 800 nm". In: *Optics Letters* 25.1 (2000), p. 25. DOI: `10.1364/ol.25.000025` (cit. on p. 5).

[27] Scott A. Diddams, David J. Jones, Jun Ye, Steven T. Cundiff, John L. Hall, Jinendra K. Ranka, Robert S. Windeler, Ronald Holzwarth, Thomas Udem, and T. W. Hänsch. "Direct Link between Microwave and Optical Frequencies with a 300 THz Femtosecond Laser Comb". In: *Physical Review Letters* 84.22 (2000), pp. 5102–5105. DOI: `10.1103/physrevlett.84.5102` (cit. on p. 5).

[28] H.R. Telle, B. Lipphardt, and J. Stenger. "Kerr-lens, mode-locked lasers as transfer oscillators for optical frequency measurements". In: *Applied Physics B: Lasers and Optics* 74.1 (2002), pp. 1–6. DOI: `10.1007/s003400100735` (cit. on pp. 5, 33, 74).

[29] L A M Johnson, P Gill, and H S Margolis. “Evaluating the performance of the NPL femtosecond frequency combs: agreement at the 10^{-21} level”. In: *Metrologia* 52.1 (2015), pp. 62–71. DOI: `10.1088/0026-1394/52/1/62` (cit. on pp. 5, 19, 35, 52).

[30] Gérard Petit, Amale Kanj, Sylvain Loyer, Jérôme Delporte, Flavien Mercier, and Félix Perosanz. “1×10^{-16} frequency transfer by GPS PPP with integer ambiguity resolution”. In: *Metrologia* 52.2 (2015), pp. 301–309. DOI: `10.1088/0026-1394/52/2/301` (cit. on pp. 6, 80).

[31] Jun Ye, Jin-Long Peng, R. Jason Jones, Kevin W. Holman, John L. Hall, David J. Jones, Scott A. Diddams, John Kitching, Sebastien Bize, James C. Bergquist, Leo W. Hollberg, Lennart Robertsson, and Long-Sheng Ma. “Delivery of high-stability optical and microwave frequency standards over an optical fiber network”. In: *Journal of the Optical Society of America B* 20.7 (2003), p. 1459. DOI: `10.1364/josab.20.001459` (cit. on p. 6).

[32] M. Lessing, H. S. Margolis, C. T. A. Brown, and G. Marra. “Frequency comb-based time transfer over a 159 km long installed fiber network”. In: *Applied Physics Letters* 110.22 (2017), p. 221101. DOI: `10.1063/1.4984144` (cit. on pp. 6, 79, 81, 96).

[33] C. Lisdat, G. Grosche, N. Quintin, C. Shi, S.M.F. Raupach, C. Grebing, D. Nicolodi, F. Stefani, A. Al-Masoudi, S. Dörscher, S. Häfner, J.-L. Robyr, N. Chiodo, S. Bilicki, E. Bookjans, A. Koczwara, S. Koke, A. Kuhl, F. Wiotte, F. Meynadier, E. Camisard, M. Abgrall, M. Lours, T. Legero, H. Schnatz, U. Sterr, H. Denker, C. Chardonnet, Y. Le Coq, G. Santarelli, A. Amy-Klein, R. Le Targat, J. Lodewyck, O Lopez, and P.-E. Pottie. “A clock network for geodesy and fundamental science”. In: *Nature Communications* 7.1 (2016). DOI: `10.1038/ncomms12443` (cit. on p. 6).

[34] Marco Pizzocaro, Pierre Thoumany, Benjamin Rauf, Filippo Bregolin, Gianmaria Milani, Cecilia Clivati, Giovanni A Costanzo, Filippo Levi, and Davide Calonico. “Absolute frequency measurement of the ${}^1\mathrm{S}_0 - {}^3\mathrm{P}_0$transition of ${}^{171}\mathrm{Yb}$”. In: *Metrologia* 54.1 (2017), pp. 102–112. DOI: `10.1088/1681-7575/aa4e62` (cit. on pp. 6, 32, 36, 63, 68–70, 73, 104).

[35] Marco Pizzocaro, Filippo Bregolin, Piero Barbieri, Benjamin Rauf, Filippo Levi, and Davide Calonico. “Absolute frequency measurement of the ${}^1\mathrm{S}_0 - {}^3\mathrm{P}_0$ transition of ${}^{171}\mathrm{Yb}$ with a link to International Atomic Time”. In: *Metrologia* (2019). DOI: `10.1088/1681-7575/ab50e8` (cit. on pp. 6, 22, 23, 32, 36, 63, 71–73, 104).

[36] Nathalie Picqué and Theodor W. Hänsch. “Frequency comb spectroscopy”. In: *Nature Photonics* 13.3 (2019), pp. 146–157. DOI: `10.1038/s41566-018-0347-5` (cit. on p. 9).

[37] Cecilia Clivati, Giacomo Cappellini, Lorenzo F. Livi, Francesco Poggiali, Mario Siciliani de Cumis, Marco Mancini, Guido Pagano, Matteo Frittelli, Alberto Mura, Giovanni A. Costanzo, Filippo Levi, Davide Calonico, Leonardo Fallani, Jacopo Catani, and Massimo Inguscio. “Measuring absolute frequencies beyond the GPS limit via long-haul optical frequency dissemination”. In: *Optics Express* 24.11 (2016), p. 11865. DOI: `10.1364/oe.24.011865` (cit. on p. 9).

[38] R. Santagata, D. B. A. Tran, B. Argence, O. Lopez, S. K. Tokunaga, F. Wiotte, H. Mouhamad, A. Goncharov, M. Abgrall, Y. Le Coq, H. Alvarez-Martinez, R. Le Targat, W. K. Lee, D. Xu, P.-E. Pottie, B. Darquié, and A. Amy-Klein. “High-precision methanol spectroscopy with a widely tunable SI-traceable frequency-comb-based mid-infrared QCL”. In: *Optica* 6.4 (2019), p. 411. DOI: `10.1364/optica.6.000411` (cit. on p. 9).

[39] Arman Cingöz, Dylan C. Yost, Thomas K. Allison, Axel Ruehl, Martin E. Fermann, Ingmar Hartl, and Jun Ye. “Direct frequency comb spectroscopy in the extreme ultraviolet”. In: *Nature* 482.7383 (2012), pp. 68–71. DOI: `10.1038/nature10711` (cit. on p. 9).

[40] Ian Coddington, Nathan Newbury, and William Swann. “Dual-comb spectroscopy”. In: *Optica* 3.4 (2016), p. 414. DOI: `10.1364/optica.3.000414` (cit. on p. 9).

[41] Richard A. McCracken, Jake M. Charsley, and Derryck T. Reid. “A decade of astrocombs: recent advances in frequency combs for astronomy [Invited]”. In: *Optics Express* 25.13 (2017), p. 15058. DOI: `10.1364/oe.25.015058` (cit. on p. 9).

[42] T. M. Fortier, M. S. Kirchner, F. Quinlan, J. Taylor, J. C. Bergquist, T. Rosenband, N. Lemke, A. Ludlow, Y. Jiang, C. W. Oates, and S. A. Diddams. “Generation of ultrastable microwaves via optical frequency division”. In: *Nature Photonics* 5.7 (2011), pp. 425–429. DOI: `10.1038/nphoton.2011.121` (cit. on pp. 9, 25, 31, 60).

[43] Yoon-Soo Jang and Seung-Woo Kim. “Distance Measurements Using Mode-Locked Lasers: A Review”. In: *Nanomanufacturing and Metrology* 1.3 (2018), pp. 131–147. DOI: `10.1007/s41871-018-0017-8` (cit. on p. 9).

[44] Orazio Svelto. *Principles of Lasers*. Springer US, 1976. DOI: `10.1007/978-1-4899-2748-4` (cit. on pp. 10–14).

[45] E. P. Ippen. “Principles of passive mode locking”. In: *Applied Physics B Laser and Optics* 58.3 (1994), pp. 159–170. DOI: `10.1007/bf01081309` (cit. on p. 13).

[46] R. Ell, U. Morgner, F. X. Kärtner, J. G. Fujimoto, E. P. Ippen, V. Scheuer, G. Angelow, T. Tschudi, M. J. Lederer, A. Boiko, and B. Luther-Davies. "Generation of 5 fs pulses and octave-spanning spectra directly from a Ti:sapphire laser". In: *Optics Letters* 26.6 (2001), p. 373. DOI: `10.1364/ol.26.000373` (cit. on p. 13).

[47] G. P. Agrawal. *Nonlinear fiber optics*. Burlington: Elsevier Science, 2013. ISBN: 9780123970237 (cit. on pp. 13, 85, 97).

[48] R.H. Stolen and A. Ashkin. "Optical Kerr effect in glass waveguide". In: *Applied Physics Letters* 22.6 (1973), pp. 294–296. DOI: `10.1063/1.1654644` (cit. on p. 14).

[49] S. A. Meyer, J. A. Squier, and S. A. Diddams. "Diode-pumped Yb:KYW femtosecond laser frequency comb with stabilized carrier-envelope offset frequency". In: *The European Physical Journal D* 48.1 (2008), pp. 19–26. DOI: `10.1140/epjd/e2008-00012-8` (cit. on p. 14).

[50] M. C. Stumpf, S. Pekarek, A. E. H. Oehler, T. Südmeyer, J. M. Dudley, and U. Keller. "Self-referencable frequency comb from a 170-fs, 1.5 µm solid-state laser oscillator". In: *Applied Physics B* 99.3 (2009), pp. 401–408. DOI: `10.1007/s00340-009-3854-8` (cit. on p. 14).

[51] Steven T. Cundiff and Jun Ye. "Colloquium: Femtosecond optical frequency combs". In: *Reviews of Modern Physics* 75.1 (2003), pp. 325–342. DOI: `10.1103/revmodphys.75.325` (cit. on p. 14).

[52] H.R. Telle, G. Steinmeyer, A.E. Dunlop, J. Stenger, D.H. Sutter, and U. Keller. "Carrier-envelope offset phase control: A novel concept for absolute optical frequency measurement and ultrashort pulse generation". In: *Applied Physics B* 69.4 (1999), pp. 327–332. DOI: `10.1007/s003400050813` (cit. on p. 16).

[53] R. H. Stolen and Chinlon Lin. "Self-phase-modulation in silica optical fibers". In: *Physical Review A* 17.4 (1978), pp. 1448–1453. DOI: `10.1103/physreva.17.1448` (cit. on pp. 16, 22).

[54] Tara Fortier and Esther Baumann. "20 years of developments in optical frequency comb technology and applications". In: (Sept. 11, 2019). arXiv: `1909.05384v1 [physics.optics]` (cit. on p. 17).

[55] D. J. Jones. "Carrier-Envelope Phase Control of Femtosecond Mode-Locked Lasers and Direct Optical Frequency Synthesis". In: *Science* 288.5466 (2000), pp. 635–639. DOI: `10.1126/science.288.5466.635` (cit. on p. 17).

[56] A. Bartels, D. Heinecke, and S. A. Diddams. "10-GHz Self-Referenced Optical Frequency Comb". In: *Science* 326.5953 (2009), pp. 681–681. DOI: `10.1126/science.1179112` (cit. on p. 17).

[57] Stéphane Schilt and Thomas Südmeyer. "Carrier-Envelope Offset Stabilized Ultrafast Diode-Pumped Solid-State Lasers". In: *Applied Sciences* 5.4 (2015), pp. 787–816. DOI: 10.3390/app5040787 (cit. on p. 17).

[58] Wei Xia and Xuzong Chen. "Recent developments in fiber-based optical frequency comb and its applications". In: *Measurement Science and Technology* 27.4 (2016), p. 041001. DOI: 10.1088/0957-0233/27/4/041001 (cit. on p. 17).

[59] L. C. Sinclair, J.-D. Deschênes, L. Sonderhouse, W. C. Swann, I. H. Khader, E. Baumann, N. R. Newbury, and I. Coddington. "Invited Article: A compact optically coherent fiber frequency comb". In: *Review of Scientific Instruments* 86.8 (2015), p. 081301. DOI: 10.1063/1.4928163 (cit. on p. 18).

[60] Axel Ruehl. "Advances in Yb:Fiber Frequency Comb Technology". In: *Optics and Photonics News* 23.5 (2012), p. 30. DOI: 10.1364/opn.23.5.000030 (cit. on p. 18).

[61] Mahmoud A. Gaafar, Arash Rahimi-Iman, Ksenia A. Fedorova, Wolfgang Stolz, Edik U. Rafailov, and Martin Koch. "Mode-locked semiconductor disk lasers". In: *Advances in Optics and Photonics* 8.3 (2016), p. 370. DOI: 10.1364/aop.8.000370 (cit. on p. 18).

[62] Jérôme Faist, Gustavo Villares, Giacomo Scalari, Markus Rösch, Christopher Bonzon, Andreas Hugi, and Mattias Beck. "Quantum Cascade Laser Frequency Combs". In: *Nanophotonics* 5.2 (2016). DOI: 10.1515/nanoph-2016-0015 (cit. on p. 18).

[63] T. J. Kippenberg, R. Holzwarth, and S. A. Diddams. "Microresonator-Based Optical Frequency Combs". In: *Science* 332.6029 (2011), pp. 555–559. DOI: 10.1126/science.1193968 (cit. on p. 18).

[64] Victor Brasch, Erwan Lucas, John D Jost, Michael Geiselmann, and Tobias J Kippenberg. "Self-referenced photonic chip soliton Kerr frequency comb". In: *Light: Science & Applications* 6.1 (2016), e16202–e16202. DOI: 10.1038/lsa.2016.202 (cit. on p. 18).

[65] David R. Carlson, Daniel D. Hickstein, Wei Zhang, Andrew J. Metcalf, Franklyn Quinlan, Scott A. Diddams, and Scott B. Papp. "Ultrafast electro-optic light with subcycle control". In: *Science* 361.6409 (2018), pp. 1358–1363. DOI: 10.1126/science.aat6451 (cit. on p. 18).

[66] Andrew J. Metcalf, Tyler Anderson, Chad F. Bender, Scott Blakeslee, Wesley Brand, David R. Carlson, William D. Cochran, Scott A. Diddams, Michael Endl, Connor Fredrick, Sam Halverson, Daniel D. Hickstein, Fred Hearty, Jeff Jennings, Shubham Kanodia, Kyle F. Kaplan, Eric Levi, Emily Lubar, Suvrath Mahadevan, Andrew Monson, Joe P. Ninan, Colin Nitroy, Steve

Osterman, Scott B. Papp, Franklyn Quinlan, Larry Ramsey, Paul Robertson, Arpita Roy, Christian Schwab, Steinn Sigurdsson, Kartik Srinivasan, Gudmundur Stefansson, David A. Sterner, Ryan Terrien, Alex Wolszczan, Jason T. Wright, and Gabriel Ycas. "Stellar spectroscopy in the near-infrared with a laser frequency comb". In: *Optica* 6.2 (2019), p. 233. DOI: `10.1364/optica.6.000233` (cit. on p. 18).

[67] Yoshiaki Tamura, Hirotaka Sakuma, Keisei Morita, Masato Suzuki, Yoshinori Yamamoto, Kensaku Shimada, Yuya Honma, Kazuyuki Sohma, Takashi Fujii, and Takemi Hasegawa. "Lowest-Ever 0.1419-dB/km Loss Optical Fiber". In: *Optical Fiber Communication Conference Postdeadline Papers*. OSA, 2017. DOI: `10.1364/ofc.2017.th5d.1` (cit. on pp. 19, 82).

[68] Nathan R. Newbury and William C. Swann. "Low-noise fiber-laser frequency combs (Invited)". In: *Journal of the Optical Society of America B* 24.8 (2007), p. 1756. DOI: `10.1364/josab.24.001756` (cit. on p. 19).

[69] I. Coddington, W. C. Swann, L. Lorini, J. C. Bergquist, Y. Le Coq, C. W. Oates, Q. Quraishi, K. S. Feder, J. W. Nicholson, P. S. Westbrook, S. A. Diddams, and N. R. Newbury. "Coherent optical link over hundreds of metres and hundreds of terahertz with subfemtosecond timing jitter". In: *Nature Photonics* 1.5 (2007), pp. 283–287. DOI: `10.1038/nphoton.2007.71` (cit. on p. 19).

[70] `http://www.menlosystems.com/` (cit. on p. 19).

[71] `http://www.imra.com/` (cit. on p. 19).

[72] `http://www.toptica.com/` (cit. on p. 19).

[73] Philippe M. Becker, Anders A. Olsson, and Jay R. Simpson. *Erbium-Doped Fiber Amplifiers: Fundamentals and Technology (Optics and Photonics)*. Academic Press, 1999. ISBN: 9780080505848 (cit. on pp. 19, 21).

[74] Stefan Droste, Gabriel Ycas, Brian R. Washburn, Ian Coddington, and Nathan R. Newbury. "Optical Frequency Comb Generation based on Erbium Fiber Lasers". In: *Nanophotonics* 5.2 (2016). DOI: `10.1515/nanoph-2016-0019` (cit. on p. 20).

[75] K. Tamura, E. P. Ippen, H. A. Haus, and L. E. Nelson. "77-fs pulse generation from a stretched-pulse mode-locked all-fiber ring laser". In: *Optics Letters* 18.13 (1993), p. 1080. DOI: `10.1364/ol.18.001080` (cit. on p. 20).

[76] V.J. Matsas, T.P. Newson, D.J. Richardson, and D.N. Payne. "Selfstarting passively mode-locked fibre ring soliton laser exploiting nonlinear polarisation rotation". In: *Electronics Letters* 28.15 (1992), p. 1391. DOI: `10.1049/el:19920885` (cit. on p. 20).

[77] M. Hofer, M. E. Fermann, F. Haberl, M. H. Ober, and A. J. Schmidt. “Mode locking with cross-phase and self-phase modulation”. In: *Optics Letters* 16.7 (1991), p. 502. DOI: `10.1364/ol.16.000502` (cit. on p. 20).

[78] D.J. Richardson, R.I. Laming, D.N. Payne, V. Matsas, and M.W. Phillips. “Selfstarting, passively modelocked erbium fibre ring laser based on the amplifying Sagnac switch”. In: *Electronics Letters* 27.6 (1991), p. 542. DOI: `10.1049/el:19910341` (cit. on p. 20).

[79] Wolfgang Hänsel, Heinar Hoogland, Michele Giunta, Sebastian Schmid, Tilo Steinmetz, Ralf Doubek, Peter Mayer, Sven Dobner, Carsten Cleff, Marc Fischer, and Ronald Holzwarth. “All polarization-maintaining fiber laser architecture for robust femtosecond pulse generation”. In: *Applied Physics B* 123.1 (2017). DOI: `10.1007/s00340-016-6598-2` (cit. on p. 20).

[80] U. Keller, K.J. Weingarten, F.X. Kartner, D. Kopf, B. Braun, I.D. Jung, R. Fluck, C. Honninger, N. Matuschek, and J. Aus der Au. “Semiconductor saturable absorber mirrors (SESAM's) for femtosecond to nanosecond pulse generation in solid-state lasers”. In: *IEEE Journal of Selected Topics in Quantum Electronics* 2.3 (1996), pp. 435–453. DOI: `10.1109/2944.571743` (cit. on p. 20).

[81] Tonglei Cheng, Lei Zhang, Xiaojie Xue, Dinghuan Deng, Takenobu Suzuki, and Yasutake Ohishi. “Broadband cascaded four-wave mixing and supercontinuum generation in a tellurite microstructured optical fiber pumped at 2 µm”. In: *Optics Express* 23.4 (2015), p. 4125. DOI: `10.1364/oe.23.004125` (cit. on p. 22).

[82] T. Okuno, M. Onishi, T. Kashiwada, S. Ishikawa, and M. Nishimura. “Silica-based functional fibers with enhanced nonlinearity and their applications”. In: *IEEE Journal of Selected Topics in Quantum Electronics* 5.5 (1999), pp. 1385–1391. DOI: `10.1109/2944.806765` (cit. on p. 22).

[83] P. A. Franken and J. F. Ward. “Optical Harmonics and Nonlinear Phenomena”. In: *Reviews of Modern Physics* 35.1 (1963), pp. 23–39. DOI: `10.1103/revmodphys.35.23` (cit. on p. 23).

[84] A. V. Husakou and J. Herrmann. “Supercontinuum Generation of Higher-Order Solitons by Fission in Photonic Crystal Fibers”. In: *Physical Review Letters* 87.20 (2001). DOI: `10.1103/physrevlett.87.203901` (cit. on p. 24).

[85] Gianmaria Milani, Benjamin Rauf, Piero Barbieri, Filippo Bregolin, Marco Pizzocaro, Pierre Thoumany, Filippo Levi, and Davide Calonico. “Multiple wavelength stabilization on a single optical cavity using the offset sideband locking technique”. In: *Optics Letters* 42.10 (2017), p. 1970. DOI: `10.1364/ol.42.001970` (cit. on p. 24).

[86] W. C. Swann, J. J. McFerran, I. Coddington, N. R. Newbury, I. Hartl, M. E. Fermann, P. S. Westbrook, J. W. Nicholson, K. S. Feder, C. Langrock, and M. M. Fejer. “Fiber-laser frequency combs with subhertz relative linewidths”. In: *Optics Letters* 31.20 (2006), p. 3046. DOI: `10.1364/ol.31.003046` (cit. on p. 25).

[87] Yoshiaki Nakajima, Hajime Inaba, Kazumoto Hosaka, Kaoru Minoshima, Atsushi Onae, Masami Yasuda, Takuya Kohno, Sakae Kawato, Takao Kobayashi, Toshio Katsuyama, and Feng-Lei Hong. “A multi-branch, fiber-based frequency comb with millihertz-level relative linewidths using an intra-cavity electro-optic modulator”. In: *Optics Express* 18.2 (2010), p. 1667. DOI: `10.1364/oe.18.001667` (cit. on pp. 25, 31, 35).

[88] Kana Iwakuni, Hajime Inaba, Yoshiaki Nakajima, Takumi Kobayashi, Kazumoto Hosaka, Atsushi Onae, and Feng-Lei Hong. “Narrow linewidth comb realized with a mode-locked fiber laser using an intra-cavity waveguide electro-optic modulator for high-speed control”. In: *Optics Express* 20.13 (2012), p. 13769. DOI: `10.1364/oe.20.013769` (cit. on pp. 25, 31).

[89] J. Millo, R. Boudot, M. Lours, P. Y. Bourgeois, A. N. Luiten, Y. Le Coq, Y. Kersalé, and G. Santarelli. “Ultra-low-noise microwave extraction from fiber-based optical frequency comb”. In: *Optics Letters* 34.23 (2009), p. 3707. DOI: `10.1364/ol.34.003707` (cit. on pp. 25, 60).

[90] Franklyn Quinlan, Tara M. Fortier, Matthew S. Kirchner, Jennifer A. Taylor, Michael J. Thorpe, Nathan Lemke, Andrew D. Ludlow, Yanyi Jiang, and Scott A. Diddams. “Ultralow phase noise microwave generation with an Er:fiber-based optical frequency divider”. In: *Optics Letters* 36.16 (2011), p. 3260. DOI: `10.1364/ol.36.003260` (cit. on p. 25).

[91] Filippo Levi, Davide Calonico, Claudio E Calosso, Aldo Godone, Salvatore Micalizio, and Giovanni A Costanzo. “Accuracy evaluation of ITCsF2: a nitrogen cooled caesium fountain”. In: *Metrologia* 51.3 (2014), pp. 270–284. DOI: `10.1088/0026-1394/51/3/270` (cit. on pp. 26, 62, 69, 104).

[92] Christian Hagemann, Christian Grebing, Thomas Kessler, Stephan Falke, Nathan Lemke, Christian Lisdat, Harald Schnatz, Fritz Riehle, and Uwe Sterr. “Providing 1×10^{-16} Short-Term Stability of a 1.5 µm Laser to Optical Clocks”. In: *IEEE Transactions on Instrumentation and Measurement* 62.6 (2013), pp. 1556–1562. DOI: `10.1109/tim.2013.2242597` (cit. on pp. 31, 35).

[93] Daniele Nicolodi, Bérengère Argence, Wei Zhang, Rodolphe Le Targat, Giorgio Santarelli, and Yann Le Coq. “Spectral purity transfer between optical wavelengths at the 10^{-18} level”. In: *Nature Photonics* 8.3 (2014), pp. 219–223. DOI: `10.1038/nphoton.2013.361` (cit. on pp. 31, 35, 36, 59).

[94] Holly Leopardi, Josue Davila-Rodriguez, Franklyn Quinlan, Judith Olson, Jeff A. Sherman, Scott A. Diddams, and Tara M. Fortier. "Single-branch Er:fiber frequency comb for precision optical metrology with 10^{-18} fractional instability". In: *Optica* 4.8 (2017), p. 879. DOI: `10.1364/optica.4.000879` (cit. on pp. 31, 35, 59, 60).

[95] Hajime Inaba, Kazumoto Hosaka, Masami Yasuda, Yoshiaki Nakajima, Kana Iwakuni, Daisuke Akamatsu, Sho Okubo, Takuya Kohno, Atsushi Onae, and Feng-Lei Hong. "Spectroscopy of ^{171}Yb in an optical lattice based on laser linewidth transfer using a narrow linewidth frequency comb". In: *Optics Express* 21.7 (2013), p. 7891. DOI: `10.1364/oe.21.007891` (cit. on pp. 31, 32).

[96] G. Santarelli, C. Audoin, A. Makdissi, P. Laurent, G.J. Dick, and A. Clairon. "Frequency stability degradation of an oscillator slaved to a periodically interrogated atomic resonator". In: *IEEE Transactions on Ultrasonics, Ferroelectrics and Frequency Control* 45.4 (1998), pp. 887–894. DOI: `10.1109/58.710548` (cit. on p. 31).

[97] D G Matei, T Legero, Ch Grebing, S Häfner, Ch Lisdat, R Weyrich, W Zhang, L Sonderhouse, J M Robinson, F Riehle, J Ye, and U Sterr. "A second generation of low thermal noise cryogenic silicon resonators". In: *Journal of Physics: Conference Series* 723 (2016), p. 012031. DOI: `10.1088/1742-6596/723/1/012031` (cit. on pp. 31, 36, 59, 60).

[98] W. Zhang, J. M. Robinson, L. Sonderhouse, E. Oelker, C. Benko, J. L. Hall, T. Legero, D. G. Matei, F. Riehle, U. Sterr, and J. Ye. "Ultrastable Silicon Cavity in a Continuously Operating Closed-Cycle Cryostat at 4 K". In: *Physical Review Letters* 119.24 (2017). DOI: `10.1103/physrevlett.119.243601` (cit. on p. 31).

[99] Garrett D. Cole, Wei Zhang, Michael J. Martin, Jun Ye, and Markus Aspelmeyer. "Tenfold reduction of Brownian noise in high-reflectivity optical coatings". In: *Nature Photonics* 7.8 (2013), pp. 644–650. DOI: `10.1038/nphoton.2013.174` (cit. on p. 31).

[100] G. D. Cole, W. Zhang, B. J. Bjork, D. Follman, P. Heu, C. Deutsch, L. Sonderhouse, C. Franz, A. Alexandrovski, O. H. Heckl, J. Ye, and M. Aspelmeyer. "Low-loss crystalline coatings for the near- and mid-infrared". In: *Advanced Optics for Defense Applications: UV through LWIR*. Ed. by Jay N. Vizgaitis, Bjørn F. Andresen, Peter L. Marasco, Jasbinder S. Sanghera, and Miguel P. Snyder. SPIE, 2016. DOI: `10.1117/12.2234740` (cit. on p. 31).

[101] Sebastian Häfner, Stephan Falke, Christian Grebing, Stefan Vogt, Thomas Legero, Mikko Merimaa, Christian Lisdat, and Uwe Sterr. "8×10^{-17} fractional laser frequency instability with a long room-temperature cavity". In:

Optics Letters 40.9 (2015), p. 2112. DOI: 10.1364/ol.40.002112 (cit. on p. 31).

[102] Kenji Numata, Amy Kemery, and Jordan Camp. "Thermal-Noise Limit in the Frequency Stabilization of Lasers with Rigid Cavities". In: *Physical Review Letters* 93.25 (2004). DOI: 10.1103/physrevlett.93.250602 (cit. on p. 31).

[103] John M. Robinson, Eric Oelker, William R. Milner, Wei Zhang, Thomas Legero, Dan G. Matei, Fritz Riehle, Uwe Sterr, and Jun Ye. "Crystalline optical cavity at 4K with thermal-noise-limited instability and ultralow drift". In: *Optica* 6.2 (2019), p. 240. DOI: 10.1364/optica.6.000240 (cit. on pp. 31, 36, 59).

[104] D. G. Matei, T. Legero, S. Häfner, C. Grebing, R. Weyrich, W. Zhang, L. Sonderhouse, J. M. Robinson, J. Ye, F. Riehle, and U. Sterr. "1.5 µm Lasers with Sub-10 mHz Linewidth". In: *Physical Review Letters* 118.26 (2017). DOI: 10.1103/physrevlett.118.263202 (cit. on p. 31).

[105] Masao Takamoto, Tetsushi Takano, and Hidetoshi Katori. "Frequency comparison of optical lattice clocks beyond the Dick limit". In: *Nature Photonics* 5.5 (2011), pp. 288–292. DOI: 10.1038/nphoton.2011.34 (cit. on p. 31).

[106] Helen Margolis. "Timekeepers of the future". In: *Nature Physics* 10.2 (2014), pp. 82–83. DOI: 10.1038/nphys2834 (cit. on p. 31).

[107] Nils Nemitz, Takuya Ohkubo, Masao Takamoto, Ichiro Ushijima, Manoj Das, Noriaki Ohmae, and Hidetoshi Katori. "Frequency ratio of Yb and Sr clocks with 5×10^{-17} uncertainty at 150 seconds averaging time". In: *Nature Photonics* 10.4 (2016), pp. 258–261. DOI: 10.1038/nphoton.2016.20 (cit. on pp. 31, 34, 73, 76, 77).

[108] H. S. Margolis, R. M. Godun, P. Gill, L. A. M. Johnson, S. L. Shemar, P. B. Whibberley, D. Calonico, F. Levi, L. Lorini, M. Pizzocaro, P. Delva, S. Bize, J. Achkar, H. Denker, L. Timmen, C. Voigt, S. Falke, D. Piester, C. Lisdat, U. Sterr, S. Vogt, S. Weyers, J. Gersl, T. Lindvall, and M. Merimaa. "International timescales with optical clocks (ITOC)". In: *2013 Joint European Frequency and Time Forum & International Frequency Control Symposium (EFTF/IFC)*. IEEE, 2013. DOI: 10.1109/eftf-ifc.2013.6702183 (cit. on pp. 32, 69).

[109] Christian Grebing, Ali Al-Masoudi, Sören Dörscher, Sebastian Häfner, Vladislav Gerginov, Stefan Weyers, Burghard Lipphardt, Fritz Riehle, Uwe Sterr, and Christian Lisdat. "Realization of a timescale with an accurate optical lattice clock". In: *Optica* 3.6 (2016), p. 563. DOI: 10.1364/optica.3.000563 (cit. on p. 32).

[110] Hidekazu Hachisu, Fumimaru Nakagawa, Yuko Hanado, and Tetsuya Ido. "Months-long real-time generation of a time scale based on an optical clock". In: *Scientific Reports* 8.1 (2018). DOI: `10.1038/s41598-018-22423-5` (cit. on pp. 32, 71).

[111] Piero Barbieri, Cecilia Clivati, Marco Pizzocaro, Filippo Levi, and Davide Calonico. "Spectral purity transfer with 5×10^{-17} instability at 1 s using a multibranch Er:fiber frequency comb". In: *Metrologia* 56.4 (2019), p. 045008. DOI: `10.1088/1681-7575/ab2b0f` (cit. on pp. 32, 60, 103).

[112] Cecilia Clivati, Roberto Ambrosini, Thomas Artz, Alessandra Bertarini, Claudio Bortolotti, Matteo Frittelli, Filippo Levi, Alberto Mura, Giuseppe Maccaferri, Mauro Nanni, Monia Negusini, Federico Perini, Mauro Roma, Matteo Stagni, Massimo Zucco, and Davide Calonico. "A VLBI experiment using a remote atomic clock via a coherent fibre link". In: *Scientific Reports* 7.1 (2017). DOI: `10.1038/srep40992` (cit. on p. 32).

[113] Marco G. Tarallo, Davide Calonico, Filippo Levi, Matteo Barbiero, Giacomo Lamporesi, and Gabriele Ferrari. "A strontium optical lattice clock apparatus for precise frequency metrology and beyond". In: *2017 Joint Conference of the European Frequency and Time Forum and IEEE International Frequency Control Symposium (EFTF/IFC)*. IEEE, 2017. DOI: `10.1109/fcs.2017.8089020` (cit. on pp. 32, 59, 104).

[114] Daisuke Akamatsu, Yoshiaki Nakajima, Hajime Inaba, Kazumoto Hosaka, Masami Yasuda, Atsushi Onae, and Feng-Lei Hong. "Narrow linewidth laser system realized by linewidth transfer using a fiber-based frequency comb for the magneto-optical trapping of strontium". In: *Optics Express* 20.14 (2012), p. 16010. DOI: `10.1364/oe.20.016010` (cit. on p. 32).

[115] Jacopo Grotti, Silvio Koller, Stefan Vogt, Sebastian Häfner, Uwe Sterr, Christian Lisdat, Heiner Denker, Christian Voigt, Ludger Timmen, Antoine Rolland, Fred N. Baynes, Helen S. Margolis, Michel Zampaolo, Pierre Thoumany, Marco Pizzocaro, Benjamin Rauf, Filippo Bregolin, Anna Tampellini, Piero Barbieri, Massimo Zucco, Giovanni A. Costanzo, Cecilia Clivati, Filippo Levi, and Davide Calonico. "Geodesy and metrology with a transportable optical clock". In: *Nature Physics* 14.5 (2018), pp. 437–441. DOI: `10.1038/s41567-017-0042-3` (cit. on pp. 34, 63, 73, 75, 76, 104).

[116] Jörn Stenger, Harald Schnatz, Christian Tamm, and Harald R. Telle. "Ultraprecise Measurement of Optical Frequency Ratios". In: *Physical Review Letters* 88.7 (2002). DOI: `10.1103/physrevlett.88.073601` (cit. on pp. 35, 45, 74).

[117] Gabriel Ycas, Steve Osterman, and Scott A. Diddams. “Generation of a 660–2100 nm laser frequency comb based on an erbium fiber laser”. In: *Optics Letters* 37.12 (2012), p. 2199. DOI: `10.1364/ol.37.002199` (cit. on p. 35).

[118] Ken Kashiwagi, Yoshiaki Nakajima, Masato Wada, Sho Okubo, and Hajime Inaba. “Multi-branch fiber comb with relative frequency uncertainty at 10^{-20} using fiber noise difference cancellation”. In: *Optics Express* 26.7 (2018), p. 8831. DOI: `10.1364/oe.26.008831` (cit. on p. 35).

[119] Yusuke Hisai, Daisuke Akamatsu, Takumi Kobayashi, Sho Okubo, Hajime Inaba, Kazumoto Hosaka, Masami Yasuda, and Feng-Lei Hong. “Development of 8-branch Er:fiber frequency comb for Sr and Yb optical lattice clocks”. In: *Optics Express* 27.5 (2019), p. 6404. DOI: `10.1364/oe.27.006404` (cit. on p. 35).

[120] Noriaki Ohmae, Naoya Kuse, Martin E. Fermann, and Hidetoshi Katori. “All-polarization-maintaining, single-port Er:fiber comb for high-stability comparison of optical lattice clocks”. In: *Applied Physics Express* 10.6 (2017), p. 062503. DOI: `10.7567/apex.10.062503` (cit. on p. 35).

[121] N. Hinkley, J. A. Sherman, N. B. Phillips, M. Schioppo, N. D. Lemke, K. Beloy, M. Pizzocaro, C. W. Oates, and A. D. Ludlow. “An Atomic Clock with 10^{-18} Instability”. In: *Science* 341.6151 (2013), pp. 1215–1218. DOI: `10.1126/science.1240420` (cit. on p. 36).

[122] T.L. Nicholson, S.L. Campbell, R.B. Hutson, G.E. Marti, B.J. Bloom, R.L. McNally, W. Zhang, M.D. Barrett, M.S. Safronova, G.F. Strouse, W.L. Tew, and J. Ye. “Systematic evaluation of an atomic clock at 2×10^{-18} total uncertainty”. In: *Nature Communications* 6.1 (2015). DOI: `10.1038/ncomms7896` (cit. on pp. 36, 80).

[123] N. Huntemann, C. Sanner, B. Lipphardt, Chr. Tamm, and E. Peik. “Single-Ion Atomic Clock with 3×10^{-18} Systematic Uncertainty”. In: *Physical Review Letters* 116.6 (2016). DOI: `10.1103/physrevlett.116.063001` (cit. on pp. 36, 80).

[124] M. Schioppo, R. C. Brown, W. F. McGrew, N. Hinkley, R. J. Fasano, K. Beloy, T. H. Yoon, G. Milani, D. Nicolodi, J. A. Sherman, N. B. Phillips, C. W. Oates, and A. D. Ludlow. “Ultrastable optical clock with two cold-atom ensembles”. In: *Nature Photonics* 11.1 (2016), pp. 48–52. DOI: `10.1038/nphoton.2016.231` (cit. on p. 36).

[125] Benjamin Rauf. “Absolute frequency measurement of an ^{171}Yb lattice clock and optical clock comparisons”. PhD thesis. Politecnico di Torino, 2018 (cit. on pp. 36, 52).

[126] Antoine Rolland, Peng Li, Naoya Kuse, Jie Jiang, Marco Cassinerio, Carsten Langrock, and Martin E. Fermann. "Ultra-broadband dual-branch optical frequency comb with 10^{-18} instability". In: *Optica* 5.9 (2018), p. 1070. DOI: `10.1364/optica.5.001070` (cit. on p. 36).

[127] R. W. P. Drever, J. L. Hall, F. V. Kowalski, J. Hough, G. M. Ford, A. J. Munley, and H. Ward. "Laser phase and frequency stabilization using an optical resonator". In: *Applied Physics B Photophysics and Laser Chemistry* 31.2 (1983), pp. 97–105. DOI: `10.1007/bf00702605` (cit. on p. 36).

[128] Eric D. Black. "An introduction to Pound–Drever–Hall laser frequency stabilization". In: *American Journal of Physics* 69.1 (2001), pp. 79–87. DOI: `10.1119/1.1286663` (cit. on p. 36).

[129] M. Pizzocaro, G. A. Costanzo, A. Godone, F. Levi, A. Mura, M. Zoppi, and D. Calonico. "Realization of an ultrastable 578-nm laser for an Yb lattice clock". In: *IEEE Transactions on Ultrasonics, Ferroelectrics and Frequency Control* 59.3 (2012), pp. 426–431. DOI: `10.1109/tuffc.2012.2211` (cit. on p. 38).

[130] D. A. Howe D. B. Sullivan D. W. Allan and F. L. Walls. *NIST Technical Note 1337: Characterization of Clocks and Oscillators.* `https://tf.nist.gov/general/pdf/868.pdf`. 1990 (cit. on p. 38).

[131] Fritz Riehle. *Frequency Standards: Basics and Applications.* Wiley-VCH, 2005. ISBN: 3-527-40230-6 (cit. on p. 38).

[132] Long-Sheng Ma, Peter Jungner, Jun Ye, and John L. Hall. "Delivering the same optical frequency at two places: accurate cancellation of phase noise introduced by an optical fiber or other time-varying path". In: *Optics Letters* 19.21 (1994), p. 1777. DOI: `10.1364/ol.19.001777` (cit. on pp. 38, 82).

[133] B. Rauf, M. C. Vélez López, P. Thoumany, M. Pizzocaro, and D. Calonico. "Phase noise cancellation in polarisation-maintaining fibre links". In: *Review of Scientific Instruments* 89.3 (2018), p. 033103. DOI: `10.1063/1.5016514` (cit. on pp. 38, 68).

[134] Cecilia Clivati, Alberto Mura, Davide Calonico, Filippo Levi, Giovanni A. Costanzo, Claudio E. Calosso, and Aldo Godone. "Planar-waveguide external cavity laser stabilization for an optical link with 10^{-19} frequency stability". In: *IEEE Transactions on Ultrasonics, Ferroelectrics, and Frequency Control* 58.12 (2011), pp. 2582–2587. DOI: `10.1109/tuffc.2011.2121` (cit. on p. 39).

[135] J.E. Stalnaker, S.A. Diddams, T.M. Fortier, K. Kim, L. Hollberg, J.C. Bergquist, W.M. Itano, M.J. Delany, L. Lorini, W.H. Oskay, T.P. Heavner, S.R. Jefferts, F. Levi, T.E. Parker, and J. Shirley. "Optical-to-microwave frequency comparison with fractional uncertainty of 10^{-15}". In: *Applied Physics B* 89.2-3 (2007), pp. 167–176. DOI: `10.1007/s00340-007-2762-z` (cit. on p. 45).

[136] Michael J. Martin, Seth M. Foreman, T. R. Schibli, and Jun Ye. "Testing ultrafast mode-locking at microhertz relative optical linewidth". In: *Optics Express* 17.2 (2009), p. 558. DOI: `10.1364/oe.17.000558` (cit. on p. 45).

[137] G. Kramer and W. Klische. "Extra high precision digital phase recorder". In: *18th European Frequency and Time Forum (EFTF 2004)*. IEE, 2004. DOI: `10.1049/cp:20040935` (cit. on p. 45).

[138] Enrico Rubiola. "On the measurement of frequency and of its sample variance with high-resolution counters". In: *Review of Scientific Instruments* 76.5 (2005), p. 054703. DOI: `10.1063/1.1898203` (cit. on p. 45).

[139] Erik Benkler, Christian Lisdat, and Uwe Sterr. "On the relation between uncertainties of weighted frequency averages and the various types of Allan deviations". In: *Metrologia* 52.4 (2015), pp. 565–574. DOI: `10.1088/0026-1394/52/4/565` (cit. on p. 45).

[140] Claudio E. Calosso, Cecilia Clivati, and Salvatore Micalizio. "Avoiding Aliasing in Allan Variance: An Application to Fiber Link Data Analysis". In: *IEEE Transactions on Ultrasonics, Ferroelectrics, and Frequency Control* 63.4 (2016), pp. 646–655. DOI: `10.1109/tuffc.2016.2519265` (cit. on p. 45).

[141] G. Ascheid and H. Meyr. "Cycle Slips in Phase-Locked Loops: A Tutorial Survey". In: *IEEE Transactions on Communications* 30.10 (1982), pp. 2228–2241. DOI: `10.1109/tcom.1982.1095423` (cit. on p. 46).

[142] `https://docs.python.org/2/library/decimal.html` (cit. on p. 47).

[143] Enrico Rubiola. *Phase Noise and Frequency Stability in Oscillators (The Cambridge RF and Microwave Engineering Series)*. Cambridge University Press, 2008. ISBN: 978-0-521-88677-2 (cit. on pp. 58, 59).

[144] J.E. Gray and D.W. Allan. "A Method for Estimating the Frequency Stability of an Individual Oscillator". In: *28th Annual Symposium on Frequency Control*. IEEE, 1974. DOI: `10.1109/freq.1974.200027` (cit. on p. 61).

[145] B. Lipphardt, G. Grosche, U. Sterr, C. Tamm, S. Weyers, and H. Schnatz. "The Stability of an Optical Clock Laser Transferred to the Interrogation Oscillator for a Cs Fountain". In: *IEEE Transactions on Instrumentation and Measurement* 58.4 (2009), pp. 1258–1262. DOI: `10.1109/tim.2008.2007051` (cit. on p. 62).

[146] Heiner Denker, Ludger Timmen, Christian Voigt, Stefan Weyers, Ekkehard Peik, Helen S. Margolis, Pacôme Delva, Peter Wolf, and Gérard Petit. "Geodetic methods to determine the relativistic redshift at the level of 10^{-18} in the context of international timescales: a review and practical results". In: *Journal of Geodesy* 92.5 (2017), pp. 487–516. DOI: `10.1007/s00190-017-1075-1` (cit. on p. 69).

[147] D Calonico, A Cina, I H Bendea, F Levi, L Lorini, and A Godone. "Gravitational redshift at INRIM". In: *Metrologia* 44.5 (2007), pp. L44–L48. DOI: `10.1088/0026-1394/44/5/n03` (cit. on p. 69).

[148] Hidekazu Hachisu, Gérard Petit, and Tetsuya Ido. "Absolute frequency measurement with uncertainty below 1×10^{-15} using International Atomic Time". In: *Applied Physics B* 123.1 (2016). DOI: `10.1007/s00340-016-6603-9` (cit. on p. 70).

[149] Pierre Dubé, John E Bernard, and Marina Gertsvolf. "Absolute frequency measurement of the ^{88}Sr clock transition using a GPS link to the SI second". In: *Metrologia* 54.3 (2017), pp. 290–298. DOI: `10.1088/1681-7575/aa5e60` (cit. on p. 70).

[150] Charles F. A. Baynham, Rachel M. Godun, Jonathan M. Jones, Steven A. King, Peter B. R. Nisbet-Jones, Fred Baynes, Antoine Rolland, Patrick E. G. Baird, Kai Bongs, Patrick Gill, and Helen S. Margolis. "Absolute frequency measurement of the optical clock transition in with an uncertainty of using a frequency link to international atomic time". In: *Journal of Modern Optics* 65.5-6 (2017), pp. 585–591. DOI: `10.1080/09500340.2017.1384514` (cit. on p. 70).

[151] E F Arias, G Panfilo, and G Petit. "Timescales at the BIPM". In: *Metrologia* 48.4 (2011), S145–S153. DOI: `10.1088/0026-1394/48/4/s04` (cit. on pp. 70, 71).

[152] Slawomir Bilicki, Eva Bookjans, Gregoire Vallet, Michel Abgrall, Rodolphe Le Targat, and Jerome Lodewyck. "Contributing to TAI with Sr optical lattice clocks". In: *2017 Joint Conference of the European Frequency and Time Forum and IEEE International Frequency Control Symposium (EFTF/IFC)*. IEEE, 2017. DOI: `10.1109/fcs.2017.8089044` (cit. on p. 71).

[153] `https://www.bipm.org/en/bipm/tai/` (cit. on p. 71).

[154] Takuya Kohno, Masami Yasuda, Kazumoto Hosaka, Hajime Inaba, Yoshiaki Nakajima, and Feng-Lei Hong. "One-Dimensional Optical Lattice Clock with a Fermionic171Yb Isotope". In: *Applied Physics Express* 2 (2009), p. 072501. DOI: `10.1143/apex.2.072501` (cit. on p. 73).

[155] N. Lemke, A. Ludlow, Z. Barber, T. Fortier, S. Diddams, Y. Jiang, S. Jefferts, T. Heavner, T. Parker, and C. Oates. “Spin-1/2 Optical Lattice Clock”. In: *Physical Review Letters* 103.6 (2009). DOI: `10.1103/physrevlett.103.063001` (cit. on p. 73).

[156] Masami Yasuda, Hajime Inaba, Takuya Kohno, Takehiko Tanabe, Yoshiaki Nakajima, Kazumoto Hosaka, Daisuke Akamatsu, Atsushi Onae, Tomonari Suzuyama, Masaki Amemiya, and Feng-Lei Hong. “Improved Absolute Frequency Measurement of the ^{171}Yb Optical Lattice Clock towards a Candidate for the Redefinition of the Second”. In: *Applied Physics Express* 5.10 (2012), p. 102401. DOI: `10.1143/apex.5.102401` (cit. on p. 73).

[157] Chang Yong Park, Dai-Hyuk Yu, Won-Kyu Lee, Sang Eon Park, Eok Bong Kim, Sun Kyung Lee, Jun Woo Cho, Tai Hyun Yoon, Jongchul Mun, Sung Jong Park, Taeg Yong Kwon, and Sang-Bum Lee. “Absolute frequency measurement of ^{1}S$_0$ (F= 1/2) - ^{3}P$_0$ (F= 1/2) transition of ^{171}Yb atoms in a one-dimensional optical lattice at KRISS”. In: *Metrologia* 50.2 (2013), pp. 119–128. DOI: `10.1088/0026-1394/50/2/119` (cit. on p. 73).

[158] Daisuke Akamatsu, Masami Yasuda, Hajime Inaba, Kazumoto Hosaka, Takehiko Tanabe, Atsushi Onae, and Feng-Lei Hong. “Frequency ratio measurement of ^{171}Yb and ^{87}Sr optical lattice clocks”. In: *Optics Express* 22.7 (2014), p. 7898. DOI: `10.1364/oe.22.007898` (cit. on pp. 73, 76).

[159] Masao Takamoto, Ichiro Ushijima, Manoj Das, Nils Nemitz, Takuya Ohkubo, Kazuhiro Yamanaka, Noriaki Ohmae, Tetsushi Takano, Tomoya Akatsuka, Atsushi Yamaguchi, and Hidetoshi Katori. “Frequency ratios of Sr, Yb, and Hg based optical lattice clocks and their applications”. In: *Comptes Rendus Physique* 16.5 (2015), pp. 489–498. DOI: `10.1016/j.crhy.2015.04.003` (cit. on pp. 73, 76).

[160] Huidong Kim, Myoung-Sun Heo, Won-Kyu Lee, Chang Yong Park, Hyun-Gue Hong, Sang-Wook Hwang, and Dai-Hyuk Yu. “Improved absolute frequency measurement of the ^{171}Yb optical lattice clock at KRISS relative to the SI second”. In: *Japanese Journal of Applied Physics* 56.5 (2017), p. 050302. DOI: `10.7567/jjap.56.050302` (cit. on p. 73).

[161] Daisuke Akamatsu, Takumi Kobayashi, Yusuke Hisai, Takehiko Tanabe, Kazumoto Hosaka, Masami Yasuda, and Feng-Lei Hong. “Dual-Mode Operation of an Optical Lattice Clock Using Strontium and Ytterbium Atoms”. In: *IEEE Transactions on Ultrasonics, Ferroelectrics, and Frequency Control* 65.6 (2018), pp. 1069–1075. DOI: `10.1109/tuffc.2018.2819888` (cit. on pp. 73, 76).

[162] Miho Fujieda, Sung-Hoon Yang, Tadahiro Gotoh, Sang-Wook Hwang, Hidekazu Hachisu, Huidong Kim, Young Kyu Lee, Ryo Tabuchi, Tetsuya Ido, Won-Kyu Lee, Myoung-Sun Heo, Chang Yong Park, Dai-Hyuk Yu, and Gerard Petit. “Advanced Satellite-Based Frequency Transfer at the 10^{-16} Level”. In: *IEEE Transactions on Ultrasonics, Ferroelectrics, and Frequency Control* 65.6 (2018), pp. 973–978. DOI: `10.1109/tuffc.2018.2821159` (cit. on pp. 73, 76).

[163] *CIPM Recommended value: YTTERBIUM 171 ATOM.* 2018. eprint: `https://www.bipm.org/utils/common/pdf/mep/171Yb_518THz_2018.pdf` (cit. on pp. 73, 77).

[164] *CIPM Recommended value: STRONTIUM 87 ATOM.* 2018. eprint: `https://www.bipm.org/utils/common/pdf/mep/87Sr_429THz_2018.pdf` (cit. on pp. 74, 77).

[165] S. B. Koller, J. Grotti, St. Vogt, A. Al-Masoudi, S. Dörscher, S. Häfner, U. Sterr, and Ch. Lisdat. “Transportable Optical Lattice Clock with 7×10^{-17} Uncertainty”. In: *Physical Review Letters* 118.7 (2017). DOI: `10.1103/physrevlett.118.073601` (cit. on pp. 74, 76).

[166] Giuseppe Marra, Radan Slavík, Helen S. Margolis, Stephen N. Lea, Periklis Petropoulos, David J. Richardson, and Patrick Gill. “High-resolution microwave frequency transfer over an 86-km-long optical fiber network using a mode-locked laser”. In: *Optics Letters* 36.4 (2011), p. 511. DOI: `10.1364/ol.36.000511` (cit. on pp. 79, 81).

[167] Giuseppe Marra, Helen S. Margolis, and David J. Richardson. “Dissemination of an optical frequency comb over fiber with 3×10^{-18} fractional accuracy”. In: *Optics Express* 20.2 (2012), p. 1775. DOI: `10.1364/oe.20.001775` (cit. on pp. 79, 81).

[168] P. Delva, J. Lodewyck, S. Bilicki, E. Bookjans, G. Vallet, R. Le Targat, P.-E. Pottie, C. Guerlin, F. Meynadier, C. Le Poncin-Lafitte, O. Lopez, A. Amy-Klein, W.-K. Lee, N. Quintin, C. Lisdat, A. Al-Masoudi, S. Dörscher, C. Grebing, G. Grosche, A. Kuhl, S. Raupach, U. Sterr, I. R. Hill, R. Hobson, W. Bowden, J. Kronjäger, G. Marra, A. Rolland, F. N. Baynes, H. S. Margolis, and P. Gill. “Test of Special Relativity Using a Fiber Network of Optical Clocks”. In: *Physical Review Letters* 118.22 (2017). DOI: `10.1103/physrevlett.118.221102` (cit. on p. 79).

[169] H. Hachisu, M. Fujieda, S. Nagano, T. Gotoh, A. Nogami, T. Ido, St. Falke, N. Huntemann, C. Grebing, B. Lipphardt, Ch. Lisdat, and D. Piester. “Direct comparison of optical lattice clocks with an intercontinental baseline of 9000 km”. In: *Optics Letters* 39.14 (2014), p. 4072. DOI: `10.1364/ol.39.004072` (cit. on p. 80).

[170] O. Lopez, A. Amy-Klein, M. Lours, C. Chardonnet, and G. Santarelli. "High-resolution microwave frequency dissemination on an 86-km urban optical link". In: *Applied Physics B* 98.4 (2009), pp. 723–727. DOI: `10.1007/s00340-009-3832-1` (cit. on p. 81).

[171] S. Droste, F. Ozimek, Th. Udem, K. Predehl, T. W. Hänsch, H. Schnatz, G. Grosche, and R. Holzwarth. "Optical-Frequency Transfer over a Single-Span 1840 km Fiber Link". In: *Physical Review Letters* 111.11 (2013). DOI: `10.1103/physrevlett.111.110801` (cit. on pp. 81, 83).

[172] D. Calonico, E. K. Bertacco, C. E. Calosso, C. Clivati, G. A. Costanzo, M. Frittelli, A. Godone, A. Mura, N. Poli, D. V. Sutyrin, G. Tino, M. E. Zucco, and F. Levi. "High-accuracy coherent optical frequency transfer over a doubled 642-km fiber link". In: *Applied Physics B* 117.3 (2014), pp. 979–986. DOI: `10.1007/s00340-014-5917-8` (cit. on pp. 81, 83).

[173] Nicola Chiodo, Nicolas Quintin, Fabio Stefani, Fabrice Wiotte, Emilie Camisard, Christian Chardonnet, Giorgio Santarelli, Anne Amy-Klein, Paul-Eric Pottie, and Olivier Lopez. "Cascaded optical fiber link using the internet network for remote clocks comparison". In: *Optics Express* 23.26 (2015), p. 33927. DOI: `10.1364/oe.23.033927` (cit. on pp. 81, 83).

[174] Laura C. Sinclair, Hugo Bergeron, William C. Swann, Esther Baumann, Jean-Daniel Deschênes, and Nathan R. Newbury. "Comparing Optical Oscillators across the Air to Milliradians in Phase and 10^{-17} in Frequency". In: *Physical Review Letters* 120.5 (2018). DOI: `10.1103/physrevlett.120.050801` (cit. on p. 81).

[175] C. E. Calosso, E. Bertacco, D. Calonico, C. Clivati, G. A. Costanzo, M. Frittelli, F. Levi, A. Mura, and A. Godone. "Frequency transfer via a two-way optical phase comparison on a multiplexed fiber network". In: *Optics Letters* 39.5 (2014), p. 1177. DOI: `10.1364/ol.39.001177` (cit. on p. 82).

[176] Cecilia Clivati, Anna Tampellini, Alberto Mura, Filippo Levi, Giuseppe Marra, Pauline Galea, André Xuereb, and Davide Calonico. "Optical frequency transfer over submarine fiber links". In: *Optica* 5.8 (2018), p. 893. DOI: `10.1364/optica.5.000893` (cit. on p. 83).

[177] P Healey. "Instrumentation principles for optical time domain reflectometry". In: *Journal of Physics E: Scientific Instruments* 19.5 (1986), pp. 334–341. DOI: `10.1088/0022-3735/19/5/002` (cit. on p. 84).

[178] Wentai Lin, Chunxi Zhang, Lijing Li, and Sheng Liang. "Review on Development and Applications of Fiber-Optic Sensors". In: *2012 Symposium on Photonics and Optoelectronics*. IEEE, 2012. DOI: `10.1109/sopo.2012.6270996` (cit. on p. 84).

[179] Masataka Nakazawa. “Rayleigh backscattering theory for single-mode optical fibers”. In: *Journal of the Optical Society of America* 73.9 (1983), p. 1175. DOI: `10.1364/josa.73.001175` (cit. on p. 84).

[180] P.F. Wysocki, G. Jacobovitz-Veselka, D.S. Gasper, S. Kosinski, J. Costelloe, and S.W. Granlund. “Modeling, measurement, and a simple analytic approximation for the return loss of erbium-doped fiber amplifiers”. In: *IEEE Photonics Technology Letters* 7.12 (1995), pp. 1409–1411. DOI: `10.1109/68.477265` (cit. on p. 87).

[181] S.L. Hansen, K. Dybdal, and C.C. Larsen. “Gain limit in erbium-doped fiber amplifiers due to internal Rayleigh backscattering”. In: *IEEE Photonics Technology Letters* 4.6 (1992), pp. 559–561. DOI: `10.1109/68.141967` (cit. on p. 87).

[182] Xiaoyi Bao, Da-Peng Zhou, Chams Baker, and Liang Chen. “Recent Development in the Distributed Fiber Optic Acoustic and Ultrasonic Detection”. In: *Journal of Lightwave Technology* 35.16 (2017), pp. 3256–3267. DOI: `10.1109/jlt.2016.2612060` (cit. on p. 88).

[183] Yonas Muanenda. “Recent Advances in Distributed Acoustic Sensing Based on Phase-Sensitive Optical Time Domain Reflectometry”. In: *Journal of Sensors* 2018 (2018), pp. 1–16. DOI: `10.1155/2018/3897873` (cit. on p. 88).

[184] Yuelan Lu, Tao Zhu, Liang Chen, and Xiaoyi Bao. “Distributed Vibration Sensor Based on Coherent Detection of Phase-OTDR”. In: *Journal of Lightwave Technology* (2010). DOI: `10.1109/jlt.2010.2078798` (cit. on p. 88).

This Ph.D. thesis has been typeset by means of the TEX-system facilities. The typesetting engine was pdfLATEX. The document class was `toptesi`, by Claudio Beccari, with option `tipotesi=scudo`. This class is available in every up-to-date and complete TEX-system installation.